

**GEOLOGY, STRUCTURE, AND DETRITAL ZIRCON GEOCHRONOLOGY OF
CENTRAL BLUE RIDGE, SAN GABRIEL
MOUNTAINS, CALIFORNIA**

A Thesis

Presented to the

Faculty of

California State Polytechnic University, Pomona

In Partial Fulfillment

Of the Requirements for the Degree

Master of Science

In

Geology

By

Craig R. Manker

2022

CALIFORNIA STATE POLYTECHNIC UNIVERSITY, POMONA
THESIS ELECTRONIC SIGNATURE PAGE

Submitted: Term Summer Year 2022
Bronco ID: 010992579
Email Address: crmanker@cpp.edu

THESIS INFORMATION

THESIS TITLE STRUCTURAL CHARACTERISTICS AND PROTOLITH AGE OF PELONA SCHIST ON CENTRAL BLUE RI
AUTHOR Craig R. Manker
PROGRAM Geology, M.S.

SIGNATURES

Dr. Jonathan A. Nourse
Committee Chair Name
Thesis Committee Chair
Position
Professor of Geology - Dpt. Chair
Department
Geology
Organization


DocuSigned by:
Dr. Jonathan A. Nourse 8/27/2022
562E96F6E80E44B...
Signature
janourse@cpp.edu
Email

Dr. Nicholas J. Van Buer
Committee Member 2 Name
Professor of Geology
Position
Geology
Department
CPP
Organization

DocuSigned by:
N. J. Van Buer 8/27/2022
ED2E989A7B2A47B...
Signature
njvanbuer@cpp.edu
Email

Dr. Bryan P. Murray
Committee Member 3 Name
Professor of Geology
Position
Geology
Department
CPP
Organization

DocuSigned by:
Bryan P. Murray 8/27/2022
20873EBAB5874F6...
Signature
bpmurray@cpp.edu
Email

Upload Thesis Attachment: 

SIGNATURE PAGE

THESIS: GEOLOGY, STRUCTURE, AND
DETRITAL ZIRCON
GEOCHRONOLOGY OF CENTRAL
BLUE RIDGE, SAN GABRIEL
MOUNTAINS, CALIFORNIA

AUTHOR: Craig R. Manker

DATE SUBMITTED: Summer 2022

Department of Geological Sciences

Dr. Jonathon Nourse
Thesis Committee Chair
Professor of Geological Sciences

Dr. Nicholas J. Van Buer
Professor of Geological Sciences

Dr. Bryan P. Murray
Professor of Geological Sciences

ACKNOWLEDGEMENTS

I would like to thank my advisor Dr. Nourse for introducing me to this study and for his guidance throughout this challenging research subject. This study is built upon his years of detailed mapping and observations on central Blue Ridge with Cal Poly Pomona students and his insight and vast knowledge of southern California geology has proven invaluable.

I would also like to thank Dr. Carl Jacobson for his early review of this manuscript and for his constructive comments and discussion of certain aspects of this research. I am also grateful to him for incorporating our Blue Ridge samples into his Detrital Py provenance figures and allowing the use of them in this thesis. Both Dr. Nourse and Dr. Jacobson have been incredibly generous with their time in helping me finalize this study.

I would also like to thank Garrett Stewart who helped map significant portions of the areas depicted on the geologic map.

Last but certainly not least, I thank my wife Deanna for her unwavering support while I returned to school to pursue this degree, and for her patience as I spent many long hours working on this research.

ABSTRACT

The Blue Ridge schist body is a member of the larger widely distributed group of schist bodies known as the Pelona-Orocopia-Rand schists (POR). Blue Ridge and the other schists are generally thought to be composed of marine trench protoliths that were underplated beneath North America during flat slab subduction of the Farallon Plate. Mount Pinos, Sierra Pelona, Blue Ridge, and Orocopia Mountains schist bodies are generally accepted to have once been connected prior to dissection and offset along the San Andreas transform boundary. Although these schist bodies have been studied at various levels, Blue Ridge has received relatively little attention in terms of lithologic, structural, and geochronologic work.

Subunits on Blue Ridge appear to be complexly interleaved or interbedded, contrasting with some previous interpretations that metabasites should exist in the basal portions, followed by metacherts, calc-silicates, and quartzofeldspathic schist in the upper portions (i.e. an intact sequence of oceanic plate overlain by calcareous and siliceous muds followed by turbidites or sandstones). Detailed mapping shows that these subunits are randomly distributed throughout the structural sections of the schist body. Even at basal to mid structural levels, quartzofeldspathic schist is ubiquitous, and interleaved or interbedded with all other subunits.

Despite extensive analysis, there does not appear to be evidence qualitatively, for a systematic up-section variation in metamorphic grade. According to analyses of 56 thin sections, the majority of central Blue Ridge schist subunits were metamorphosed at lowermost amphibolite facies, or at the boundary between greenschist and amphibolite facies. This is consistent with published results on metamorphic grade of Blue Ridge.

A subset of syn-metamorphic asymmetric folds in two locations appears to record shearing concomitant with subduction and extrusion of the schist body. One locality records top-to-SW and top-to-NE sense of shear, and a second locality records only top-to-SW sense of shear after vertical axis rotations are performed. The resulting orientation restores to that of the convergence vector of the Farallon plate during the late Cretaceous if the Blue Ridge block is back rotated approximately 40–45 degrees. Additionally, two sets of map-scale folds exist in the study area. 1) A syn-metamorphic tight folding event with northerly trending fold hinges demonstrates that the maximum principal stress direction associated with syn-metamorphic folding varies from N78E-S78W to N73W-S73E before vertical-axis rotation. 2) A younger post-metamorphic open group of folds with WNW trending fold axes demonstrates that the maximum principal stress direction associated with the formation of these folds was N29E-S29W before vertical axis rotation.

U-Pb geochronology results indicate that the Blue Ridge schist may be treated as a quasi-intact sedimentary sequence. Two independent structural sections at near basal to mid structural levels, show that the schist body appears to preserve an intact proto-stratigraphy that displays a younging trend up-section. Combined maximum depositional ages, indicated by youngest single grain (YSG) analysis, range from 88.3 ± 2.6 Ma to 75.6 ± 1.2 Ma (2σ uncertainty) up-section. Age vs. depth relations for the structural sections show remarkable congruence between the YSG's per sample and relative depth measurements, possibly due to extreme tectonic flattening of the schist. These results potentially allow for the analysis of detrital zircon provenance changes up-section through time.

Detrital zircon analysis shows that the Blue Ridge schist body is most similar in provenance signature to the Sierra Pelona schist body, followed closely by the Mount Pinos schist body, lending further support for the proposed connection of the three schist bodies in the past. In contrast, the Orocopia Mountains schist body is sufficiently different in provenance signature from the Blue Ridge, Sierra Pelona, and Mount Pinos schist bodies, to call into question a contiguous origin or similar depocenter between them.

Blue Ridge detrital zircon samples also appear to record the expected shifts in provenance occurring up-section through time that reflect the progressive evolution from outboard to inboard source detritus (i.e. the breaching of the Sierran-Peninsular Ranges Arc and allowance of detritus from the Mojave block and San Gabriel terrane to reach the continental margin) seen in forearc strata and pooled zircon data from the POR schists. In general, the sections show the progression of erosional detritus from dominantly the Sierran-Peninsular Ranges Arc at basal structural levels (88.3 Ma), followed by the first appearance of inboard detritus in the mid structural levels (81.8 Ma), and culminating with the marked increase of inboard detritus at the uppermost structural level (75.6 Ma). Assuming that the other schist bodies also preserve relatively intact quasi-stratigraphic sections, evaluation of published data sets from Mount Pinos and Sierra Pelona schist bodies show similar provenance development through time (if the samples are defined by the youngest single grain and are assumed to roughly represent the maximum depositional age of the structural level). It is acknowledged however, that this interpretation of the data relies on several assumptions that are based on the Blue Ridge

sections, and that the data from Blue Ridge is limited in terms of the number of samples (7) as well as the low number of analyses per sample (24–72 grains).

This study shows that marine trench protoliths of the Blue Ridge schist were deposited between 88.3 Ma and approximately 75.6 Ma (minimum), then deformed in a northeast-dipping subduction zone. Two generations of folds record syn-metamorphic Laramide subduction-related deformation, followed by a period of open folding that predated development of the San Gabriel-San Andreas transform fault system. The present-day orientation of fold hinges on Blue Ridge reflects counterclockwise block rotation of ~17 degrees during development of the restraining double bend in the San Andreas fault, and clockwise block rotation of ~40–45 degrees that may be the result of transrotation between the Punchbowl and San Andreas faults.

TABLE OF CONTENTS

SIGNATURE PAGE	ii
ACKNOWLEDGEMENTS.....	iii
ABSTRACT.....	iv
LIST OF TABLES.....	x
LIST OF FIGURES	xi
INTRODUCTION	1
Purpose and Objectives	6
Location and Access	10
Previous Work	10
Background.....	14
Research Questions.....	17
Methods.....	18
DATA AND RESULTS	21
Schist Subunits and Protoliths	21
Geologic Map and Cross-Sections.....	33
Thin Section Analysis	47
Structure.....	54
<i>Map-scale Folds</i>	54
<i>Out-crop Scale Folds</i>	62
<i>Faults</i>	70
U-Pb Geochronology	71

<i>Concordia Plots</i>	74
<i>Probability Density Plots</i>	87
<i>Youngest Single Grain Analysis</i>	90
DISCUSSION AND INTERPRETATION	97
Thin Section Petrography	97
Structure	100
<i>Syn-metamorphic Folds with Northerly Hinges</i>	101
<i>Post-metamorphic Folds with West-Northwest Hinges</i>	102
<i>Late Cenozoic Faulting</i>	104
Geochronology	105
Detrital Zircon Provenance	111
Tectonic Significance	127
CONCLUSIONS	137
General Geology	137
Thin Section Analysis	137
Structure	138
U-Pb Geochronology	139
Detrital Zircon Provenance	140
Tectonic Significance	141
REFERENCES	142
APPENDIX A: Plate 1: Geologic Map of Central Blue Ridge	158
APPENDIX B: Plate 2: Cross-Sections of Central Blue Ridge	159
APPENDIX C: Table 2: U-Pb Geochronology Isotopic Data	160

LIST OF TABLES

Table 1. Central Blue Ridge Thin Section Summary	53
--	----

LIST OF FIGURES

Figure 1. Map of the Study Area	4
Figure 2. Modern Distribution of Schist Bodies.....	5
Figure 3. Pre-San Andreas Distribution of Schist Bodies.....	6
Figure 4. Protolith and Metamorphic Emplacement Ages of Schist Bodies	13
Figure 5. Flat Slab Subduction and Arc Migration.....	16
Figure 6. Muscovite-rich Grayschist Outcrop	23
Figure 7. Metasandstone Geochronology Sample JN2056.....	24
Figure 8. Greenschist Outcrop	25
Figure 9. Close up of Greenschist.....	26
Figure 10. Sample Site JN2058 (Greenschist).....	27
Figure 11. Calc-silicate Gneiss Outcrop.....	28
Figure 12. Calc-silicate Gneiss with Z-Folds	29
Figure 13. Calc-silicate Gneiss with S-Folds.....	29
Figure 14. Calc-silicate Gneiss with S-Folds.....	30
Figure 15. Metachert.....	31
Figure 16. Folded Banded Schist.....	32
Figure 17. Map Legend.....	34
Figure 18. Geologic Map (Sub Area 1)	37
Figure 19. Cross-section B.....	38
Figure 20. Cross-section C.....	39
Figure 21. Cross-section D	40

Figure 22. Cross-section E.....	41
Figure 23. Geologic Map (Sub Area 2)	43
Figure 24. Combined Cross-section F-G''.....	44
Figure 25. Geologic Map (Sub Area 3)	46
Figure 26. Sub Area 1 Fold Map	56
Figure 27. Sub Area 2 Fold Map	57
Figure 28. Sub Area 3 Fold Map	58
Figure 29. Stereonet Plots of Map-scale Folds (NW).....	59
Figure 30. Stereonet Plots of Map-scale Folds (SE).....	60
Figure 31. Stereonet Plot: All NE Map-scale Folds	61
Figure 32. Stereonet Plot: All WNW Map-scale Folds	62
Figure 33. Stereonet Plot: Ridge B Outcrop Folds	65
Figure 34. Stereonet Plot: Banded Fold Area	67
Figure 35. Stereonet Plot: Ridge E Syncline	69
Figure 36. Fault Slicken-Side and Gouge.....	71
Figure 37. Geochronology Section 2	73
Figure 38. Concordia Plot: JNCM1947 (all).....	76
Figure 39. Concordia Plot: JNCM1947 (Mz).....	77
Figure 40. Concordia Plot: JNCM1942 (all).....	78
Figure 41. Concordia Plot: JNCM1942 (Mz)	79
Figure 42. Concordia Plot: JN2056 (all).....	80
Figure 43. Concordia Plot: JN2056 (Mz)	81
Figure 44. Concordia Plot: JNCM1943 (all).....	82

Figure 45. Concordia Plot: JNCM1943 (Mz)	83
Figure 46. Concordia Plot: JN2060 (all).....	84
Figure 47. Concordia Plot: JN2060 (Mz)	85
Figure 48. Concordia Plot: JN2161 (all).....	86
Figure 49. Concordia Plot: JN2161 (Mz)	87
Figure 50. Index Map of Igneous Terranes.....	88
Figure 51. Probability Density Plots: Blue Ridge.....	89
Figure 52. Probability Density Plots: BR and East Fork	90
Figure 53. Youngest Single Grain (Sections 1 and 2)	92
Figure 54. Section 1 Depth vs. YSG.....	95
Figure 55. Section 1 Depth vs. YSG (variation).....	96
Figure 56. Section 2 Depth vs. YSG.....	96
Figure 57. Transect TC-1	108
Figure 58. Transect TC-2.....	109
Figure 59. Recalibrated Section 1 YSG Depth Profile (TC-1).....	109
Figure 60. Recalibrated Section 1 YSG Depth Profile (TC-2).....	110
Figure 61. Youngest Expected Age Model (TC-1).....	110
Figure 62. Youngest Expected Age Model (TC-2).....	111
Figure 63. Nacimiento Fault	113
Figure 64. Section 1 Detrital Zircon Provenance.....	116
Figure 65. Section 2 Detrital Zircon Provenance.....	117
Figure 66. Combined Section 1 and 2 Detrital Zircon Provenance	119
Figure 67. Mount Pinos/Sierra Pelona Provenance	121

Figure 68. Blue Ridge Provenance	122
Figure 69. East Fork/Orocopia Mountains Provenance	123
Figure 70. Grain Population Percentage per Schist Body.....	125
Figure 71. Combined Data Provenance/ First Appearance.....	126
Figure 72. Detrital Py 1.....	128
Figure 73. Detrital Py 2.....	130
Figure 74. Palinspastic Reconstruction.....	131
Figure 75. Present Orientation Map.....	133

INTRODUCTION

Blue Ridge is a northwest-trending ridge located in the eastern San Gabriel Mountains, southern California (Figure 1). The ridge is comprised of Pelona schist that occurs as a structurally isolated block, bounded by the Fenner, San Andreas, and Punchbowl faults (Grove et al., 2003). Currently, Blue Ridge lies adjacent to Pelona schist of the East Fork block, which is located on the southwest side of the Punchbowl fault (Figure 2). However, the proximity of the Blue Ridge block to the East Fork block is an artifact of late Cenozoic lateral translations associated with the San Andreas fault system. Prior to right lateral displacements along the Punchbowl and San Andreas faults, the Blue Ridge block of Pelona schist was probably located adjacent to and between the Mount Pinos schist and Sierra Pelona schist to the west (Hill and Dibblee, 1953; James and Mattinson, 1988; Dillon et al., 1990; Dillon and Ehlig, 1993; Grove et al., 2003; Coffey et al, 2019) and Orocopia Mountains schist to the east (Crowell, 1962; Ehlig, 1981; Dillon and Ehlig 1993, Grove et al., 2003; Coffey et al, 2019) (Figure 3). Consequently, it is accepted by most workers that Blue Ridge is a structurally displaced portion of a larger dissected parent schist body from which the Mount Pinos, Sierra Pelona, Blue Ridge, and Orocopia mountains schist bodies are derived (Dibblee, 1967, 1968; Ehlig, 1968; Coffey et al, 2019).

Several criteria have been used to associate the four schist bodies including: (1) the resulting position in palinspastic reconstructions (Hill and Dibblee, 1953; James and Mattinson, 1988; Dillon et al., 1990; Dillon and Ehlig, 1993; Grove et al., 2003), (2) the similarity of stratigraphy (Ehlig, 1958, 1968; Haxel and Dillon,

1978; Haxel et al., 1987, 2002; Dawson and Jacobson, 1989; Grove et al., 2003), and (3) gross similarity of metamorphic grade (Ehlig, 1958; Woodford, 1960; Platt, 1976; Jacobson and Sorensen, 1986; Jacobson et al., 2011). However, there are some differences between the schist bodies and the criteria put forth; the degree of which may or may not be important.

Structurally, there are differences between the aforementioned schist bodies as well. The orientation of the Blue Ridge block has garnered some attention (Coffey, 2019) due to an approximately N70W plunging anticline and southwest dipping foliations that have been mapped by Dibblee (2002). These structural orientations are different than those of the Sierra Pelona block anti/synclinalia which have a general orientation of N20E (Hernandez, 2013). Blue Ridge and Sierra Pelona both lie within the present double restraining bend (aka Big Bend) of the San Andreas fault which exhibits an orientation of N65W. The Orocochia mountains block is dominated by an anticlinorium trending between approximately N65W and N55W (Jacobson et al., 2007) but lies along the N48W trend of the San Andreas fault. If Blue Ridge and Sierra Pelona are corrected for the Big Bend rotation, the anticlinoria orientations become N53W and N3E respectively. Even if only simple translation is responsible for the current position and orientation of the disparate blocks, block rotation of Blue Ridge may be missing in palinspastic reconstructions.

Further confusing this issue, some differences in cooling ages and detrital zircon provenance exist between the Blue Ridge and Orocochia mountains blocks (Grove et al., 2003; Jacobson, 1990; Jacobson et al., 2002; Jacobson et al., 2007).

This calls into question whether the Blue Ridge block is truly genetically related to the Mount Pinos, Sierra Pelona and Orocopia schist bodies in the sense that they are all derived from a larger homogeneous body. While the Sierra Pelona and Orocopia schist bodies have been studied extensively, the Blue Ridge block has received comparatively little attention in terms of detailed study of the structure, stratigraphy, and geochronology.

This research will focus on detailed mapping of the structure and stratigraphy of the central Blue Ridge block as well as the sampling of quartzofeldspathic schist for U-Pb detrital zircon age analysis. Additionally, detrital zircon provenance analysis will be conducted using the aforementioned samples and the integrated data set resulting from this study will be used for comparison to the Mount Pinos, Sierra Pelona, and Orocopia Mountains schist bodies.

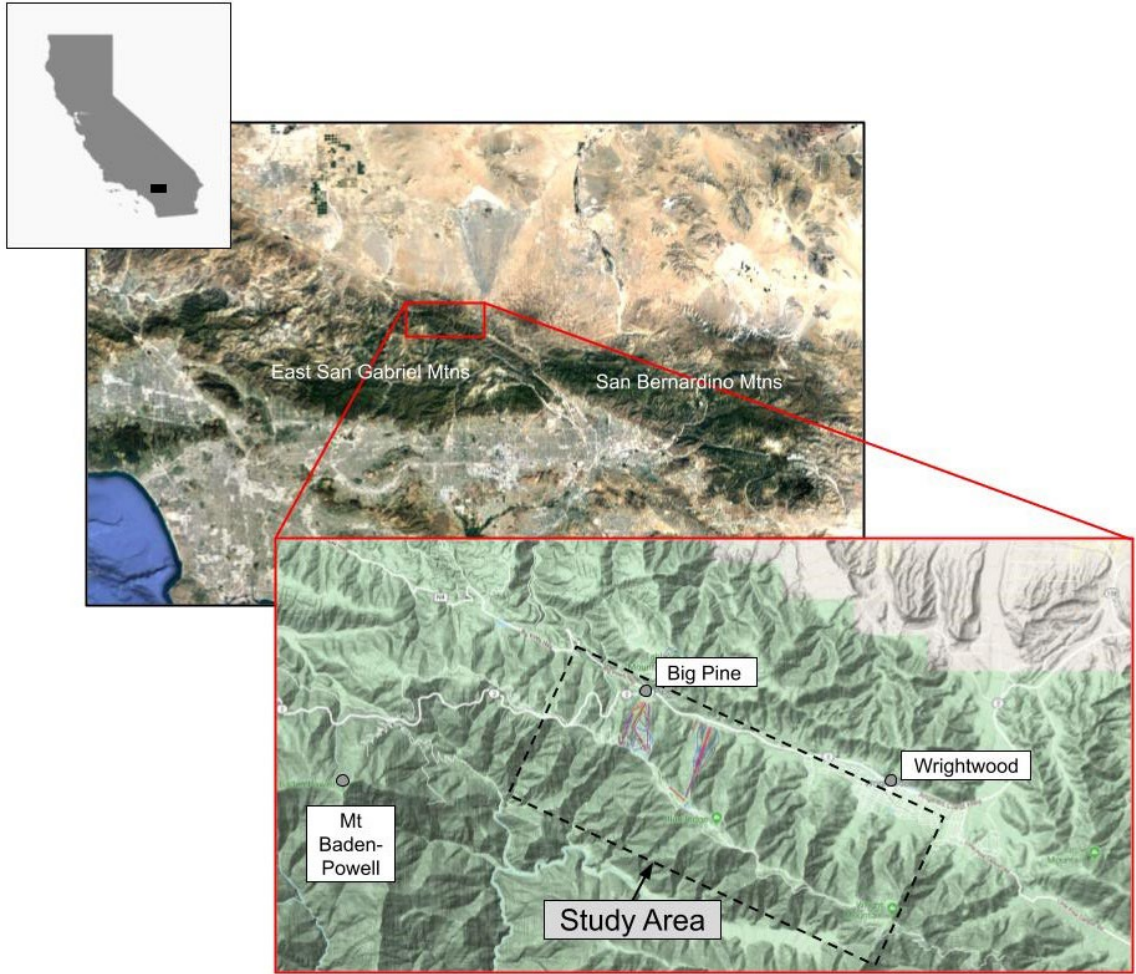


Figure 1. Overview map of the study area. Central Blue Ridge is located in the eastern San Gabriel Mountains, west-southwest of Wrightwood, California (modified from Google Earth/Google Maps).

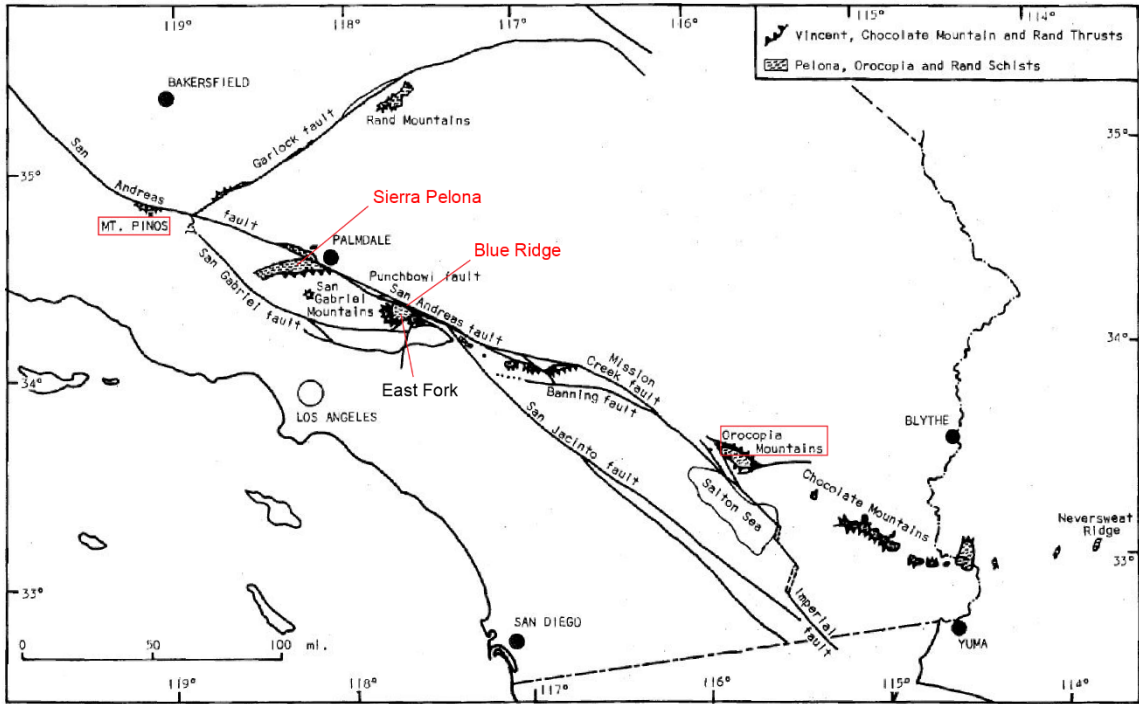


Figure 2. Area map showing current distribution of Mt. Pinos, Sierra Pelona, Blue Ridge, East Fork, and Orocopia Mountains schist bodies (modified after Ehlig, 1982).

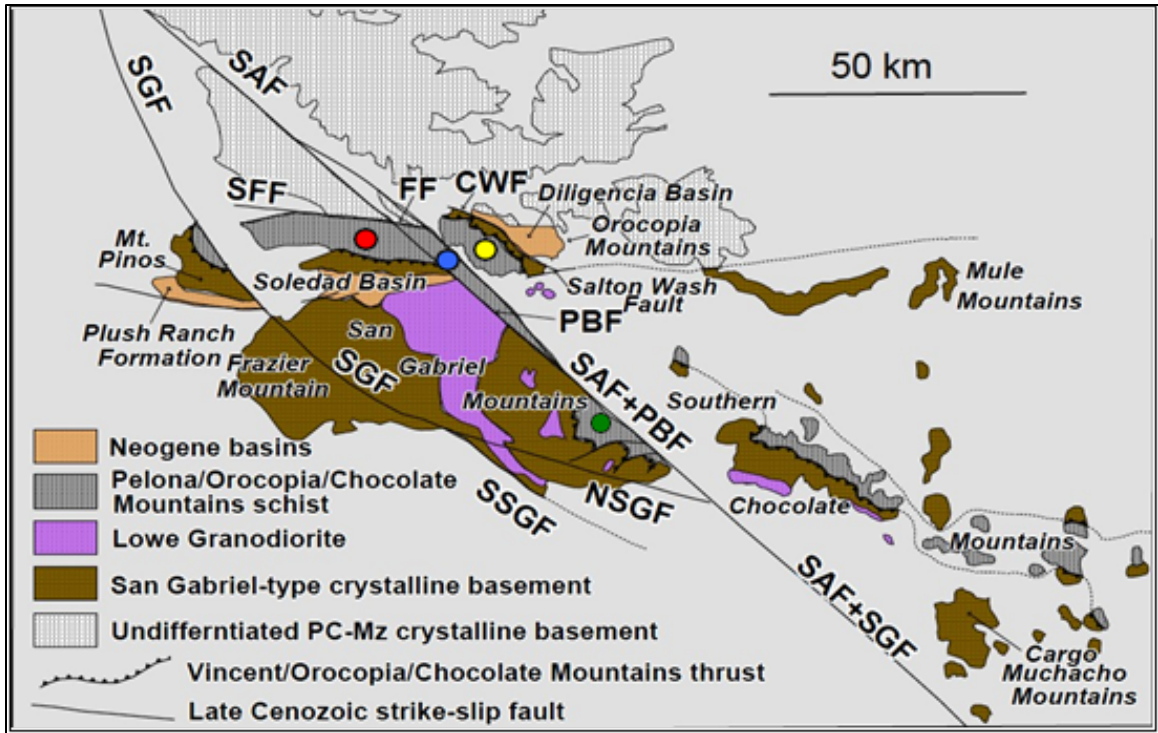


Figure 3. Palinspastic reconstruction showing relative positions of Blue Ridge (blue circle), East Fork (green circle), Sierra Pelona (red circle), Mt. Pinos, and Orocopia (yellow circle) schist bodies (after Hill and Diblee, 1953; Dillon and Ehlig, 1993; modified by Nourse, 2002).

Purpose and Objectives

The purpose of this study is to characterize the geology and structure of the Blue Ridge block, and to determine in more detail, the protolith age and provenance of the Blue Ridge Pelona schist for comparison with the Mount Pinos, Sierra Pelona, and Orocopia schist bodies. Previous mapping of Blue Ridge has only been published at the reconnaissance level and to date, age control for the Blue Ridge schist is poorly constrained due to a paucity of published detrital-zircon ages compared to the other Pelona schist bodies. Only two samples totaling seventy grains have been analyzed by Grove et al. (2003) and Jacobson et al. (2011) from the northwest area of the Blue Ridge block, but the middle and southeast areas remained unsampled at the onset of this work.

To accomplish the goal of this study; I intend to complete the following objectives: (1) Map the rock units comprising the central Blue Ridge schist body at 1:24,000 scale to 1:12,000 scale; (2) Measure and analyze foliations, folds, and faults to determine structural sequence and tectonic history; (3) Construct detailed cross-sections of the schist to constrain the subsurface for stratigraphic continuity and structure; (4) Compile thin section observations of metasandstones, metabasites, metacarbonates, and metacherts to determine whether metamorphic grade varies from deep to shallow structural levels; (5) Collect and analyze metasandstone samples for U-Pb geochronology and detrital zircon provenance; and (6) Integrate all data into a model for the tectonic evolution of Blue Ridge. I elaborate on these objectives below:

General Geology

It has been proposed and largely accepted that the Blue Ridge block is a displaced portion of the Mount Pinos, Sierra Pelona, and Orocopia Mountains blocks. If the Blue Ridge schist body is a part of the parent schist body from which the Sierra Pelona and Orocopia bodies are derived, large-scale anticlinoria present in the Sierra Pelona and Orocopia schist bodies, should be present within the Blue Ridge block and have similar orientation. Geospatial mapping of the largescale foliation patterns should show similar structural trend and orientation of the anticlinoria. However, if these features are not present or show differing orientation, foliation patterns will inform on an alternate deformational history such as local deformation and/or block rotation. Likewise, there should be similarities in metamorphic grade if the three areas were once connected.

Structure – Outcrop and Map-scale Folds

Preliminary mapping during a GSC 5030L project showed that outcrop scale folds were relatively abundant within sparse calc-silicate layers, displaying well-preserved symmetric folds and asymmetric S and Z folds. Outcrop scale fold hinges and axial plane measurements of symmetric and asymmetric folds will be recorded and analyzed geospatially to determine the direction of shortening and/or the direction of regional shearing within the Blue Ridge block. Fold tests will be conducted to determine if S and Z folds are parasitic folds with respect to large-scale folds, or if they are randomly distributed across large-scale folding trends.

Map scale folds will similarly be analyzed with respect to shortening direction by determining fold hinge and axial plane solutions of mapped foliation reversals. Comparison of the fold patterns of the Blue Ridge schist body with those of Sierra Pelona and Orocochia schist bodies will also inform on the possible relationship between them.

Post-metamorphic Faulting

During preliminary field mapping, it was observed that the stratigraphy exposed on three adjacent ridges did not appear to project along strike. Recent alluvium covered the drainages between the ridges, so no obvious structural disruption was apparent. Further mapping along the ridge revealed numerous small slicken-side exposures indicating the possible presence of a concealed fault between the two ridges. Additional fault plane exposures were located within roadcut outcrops on either side of the hypothesized fault which may define the local fault zone. To address this question, fault plane orientations and slip sense indicators will be measured and placed into fault groups

for further kinematic evaluation and determination of the possibility that cross faults exist within the block.

Protolith Age

Two apparently coherent stratigraphic sections will be sequentially sampled over a large area of the schist body to determine if there is a structurally deep to shallow variation in detrital zircon maximum depositional age (MDA) and provenance signature. This will test whether the stratigraphic section becomes younger up-section, recording normal stratigraphic deposition of the protolith, or is overturned as is suggested in other schist bodies such as the East Fork block (Morton and Miller, 2003) by the occurrence of metacherts structurally beneath metabasites. Because metacherts and metabasites are derived from protoliths of siliceous mud and abyssal basalts respectively, the inference is that metabasites occur at the base of the section and are overlain by metacherts in normal depositional setting. Additionally, evidence for a large, overturned syncline exists in the Narrows area of the East Fork block (Ehlig, 1982).

Detrital Zircon Provenance

Detrital zircon samples obtained during this study will increase the number of samples reported on Blue Ridge from two to seven and improve sample distribution over the schist body to the southeast. By combining detrital zircon analysis with detailed geologic and stratigraphic mapping, this study may provide information on provenance changes through time. Detrital zircon provenance will be evaluated with respect to regional patterns of igneous pluton age distribution following the methods of Grove et al. (2003) and Jacobson et al. (2011) and be compared to published detrital signatures of

other schist bodies such as Mount Pinos, Sierra Pelona, and Orocochia Mountains schists to determine degree of similarity or dissimilarity.

Regional Significance

In-depth study of the Blue Ridge schist body has important implications for the regional tectonic history of southern California and will answer several outstanding questions regarding the greater disposition of the Blue Ridge block.

Location and Access

Blue Ridge is a northwest-trending ridge in the eastern San Gabriel Mountains, located in portions of the Mescal Creek, Mount San Antonio, and Telegraph Peak USGS 7.5 minute quadrangles, southern California. The study area generally lies at elevations between 7,000 – 8,400 feet and is partially accessed via a Forest Service dirt road branching off state Hwy 2 at Inspiration Point overlook. Some dirt roads in the southeastern section are only accessible via 4-wheel drive vehicle and no access is available to the study area during the winter months due to snow cover and road closures along Hwy 2. A blanket of recent alluvium or colluvium covers most of the schist body except for roadcuts and most ridge lines but this normal for this rock type. Small exposures of the schist occur locally on most slopes but are distributed sparsely. A series of northeast-trending valleys that transect the area are usually covered with brush and devoid of outcrop.

Previous Work

General Geology

Previous mapping of Blue Ridge has been conducted at the reconnaissance level by Dibblee (1967) and Elig (unpublished), Dibblee and Minch (2002), and Morton and

Miller (2003). Dibblee and Minch (2002) provided the most coverage of the block, showing most foliations dipping to the SW with bands of reversals and numerous overturned folds. An undulating NW plunging anticline is shown trending approximately N70W.

Coffey et al (2019) mapped portions of the Punchbowl block, which lies west-southwest of the study area and included the northwestern tip of Blue Ridge. However, Blue Ridge was not the emphasis of the study, and the resulting geologic map depicts limited structural information. Cal Poly Pomona students have mapped a few small areas of the eastern Blue Ridge block for GSC 4910 and 5030 field classes, of which I participated in the latter, but the eastern Blue Ridge block has never been studied structurally in detail.

Metamorphic Facies

Jacobson (1980; 1983) analyzed approximately 50 thin section samples of quartzofeldspathic and mafic schist from Blue Ridge and determined that the schist was of the albite-epidote-amphibolite facies using mineralogical descriptions and ion microprobe analysis on white mica, chlorite, garnet, and amphibole.

Geochronology

Two samples (98-240 and BR218) of meta-sandstone from Blue Ridge have been collected and analyzed for U-Pb geochronology by Grove et al. (2003) and Jacobson et al. (2011). Comparatively, seven dated samples have been obtained from the Sierra Pelona schist body (Grove et al., 2003; Jacobson et al., 2011), ten dated samples from the Orocochia Mountains schist body (Grove et al., 2003; Jacobson et al., 2011; Sauer et al.,

2019), four dated samples from the East Fork schist body (Grove et al., 2003; Jacobson et al., 2011), and five from Mt. Pinos (Jacobson, 2011).

The youngest reported detrital zircon age for the Pelona schist group, defined by Grove et al. (2003) and Jacobson et al. (2011) as including the Mount Pinos, Sierra Pelona, Blue Ridge, and East Fork schist bodies is 66 Ma (Jacobson, 2011; Figure 4). However, re-interpretation of the data by the authors has led to the belief that ages less than 68 Ma from detrital zircon grains are of metamorphic origin (Dr. Carl Jacobson, personal comm.; Jacobson et al., 2017; Seymour et al., 2018). Consequently, the youngest accepted age from the Pelona schist group is 69 Ma for both Sierra Pelona and Blue Ridge. Mount Pinos, Sierra Pelona and East Fork schist bodies all show a relatively continuous spread of detrital zircon ages up to their respective youngest age. However, Blue Ridge is anomalous in that the youngest detrital zircon age of ~ 69 Ma (BR218) is preceded by the next youngest age of 79 Ma - an age gap of 10 Ma. This calls into question whether the youngest detrital zircon reported for Blue Ridge is real, since it is close to the cutoff age of 68 Ma for metamorphic ages. If the youngest age is real, the age gap may be the result of the low number of samples analyzed (two) as well as the low number of zircon grains per sample (Dr. Carl Jacobson personal commun.; Chapman, 2016).

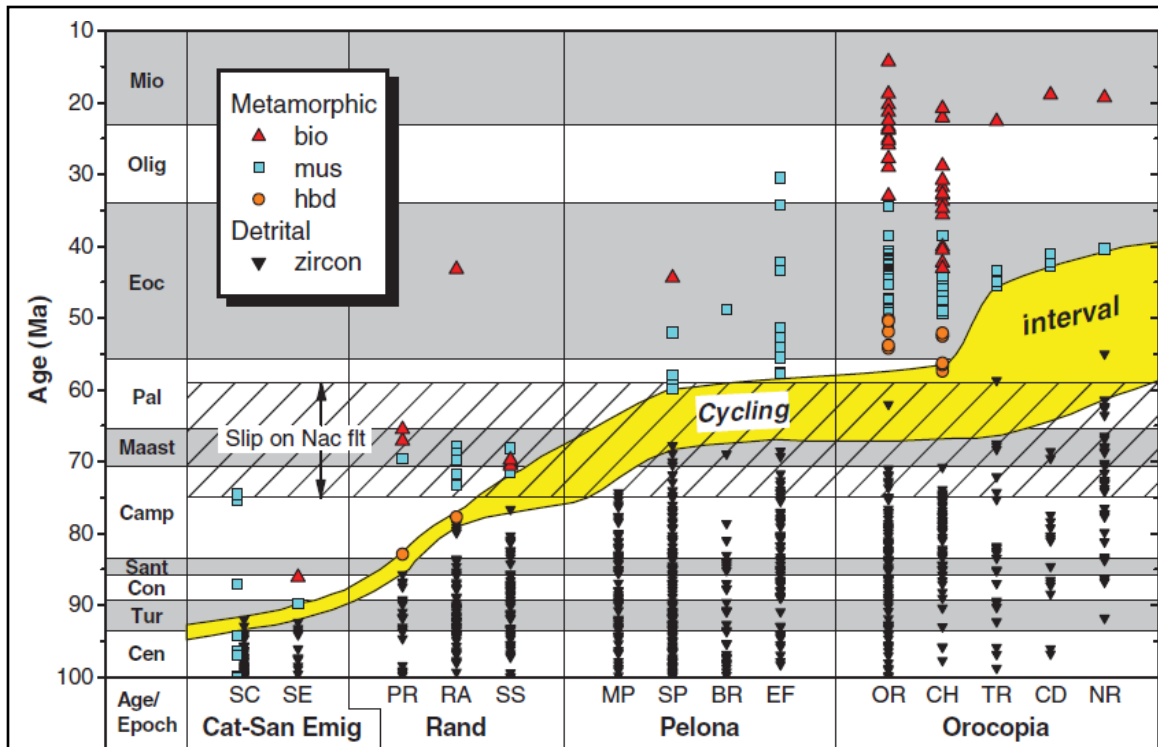


Figure 4. Protolith (black triangles) and metamorphic emplacement ages (red, blue, and orange) for schist bodies derived from detrital zircon grains and biotite/muscovite/hornblende respectively. Cycling interval indicates time interval to erode, transport, and deposit grains from source to trench. Note that ages become younger from northwest to southeast locations. BR = Blue Ridge (Jacobson, 2011).

Detrital Zircon Provenance

Provenance analysis of the of Blue Ridge samples (98-240 and BR218) is included in the works of Grove et al. (2003) and Jacobson et al. (2011). Both samples were combined to produce normalized percentage pie charts with age defined bins for tracing discrete igneous rock sources along the continental margin and inland areas. This percentage pie chart is intended to function as a visual reference whereby it can be compared to other schist body pie charts to quickly evaluate the relative percent contributions of the binned age groups. In interpreting these data, the authors used a pre-San Andreas palinspastic reconstruction of the western margin, including southern

California, southwestern Arizona, and northwestern Mexico, to infer source areas of the detrital grains and to interpret the marginal tectonic evolution of southern California.

Sources identified for the grains roughly include from west to east, the Sierran-Peninsular Ranges Arc (85–100 Ma bin and 100–135 Ma bin), the inland arc (70–85 Ma bin), and Proterozoic wall rocks (>300 Ma bin; the inclusion of all grains from 300 Ma up to and including Proterozoic grains are grouped into this bin because grains younger than Proterozoic and older than 300 Ma are rare as stated by the authors). The Jurassic arc (135–300 Ma bin) is distributed in a broad patchwork that underpins the Sierran-Peninsular Ranges Arc and extends eastward.

The pooled Blue Ridge samples show near equally high percentages of 80–100 Ma grains and 100–135 Ma grains. The next most abundant grains are listed as follows in descending order: 70–85 Ma grains; >300 Ma grains; and 55–70 Ma grains. The results of the Blue Ridge samples are similar to other Pelona group schist bodies, all of which have high percentages of 85–100 Ma and 100–135 Ma grains and variable lesser amounts of all other grain age categories.

Background

The Pelona Schist is part of a group of schist bodies known as the Pelona-Orocopia-Rand schists (Haxel and Dillon, 1978; Ehlig, 1981; Jacobson et al., 1988). These schist bodies are generally thought to be derived from trench sediments that were underplated beneath the North American crust as a result of initially normal, and then flat subduction of the Farallon plate during the Laramide orogeny (Crowell, 1968, 1981; Yeats, 1968; Burchfiel and Davis, 1981; Dickinson, 1981; Hamilton, 1988; May, 1989; Malin et al., 1995; Jacobson et al., 1996, 2002, 2007; Wood and Saleeby, 1997; Yin,

2002; Grove et al., 2003; Saleeby, 2003; Kidder and Ducea, 2006; Saleeby et al., 2007; Jacobson et al., 2011). In one model (Jacobson et al., 2011: Figure 5), flat subduction of the Farallon plate effectively removed large portions of the North American mantle lithosphere and lowermost crust, which allowed for the emplacement of the schist bodies at relatively shallow depths.

Later, middle Cenozoic extension aided in the exhumation of the schists, followed by late Cenozoic development of the San Andreas fault system, which further modified the relative positions of the schist bodies into the disparate exposures observed today (Crowell, 1962, 1981; Frost et al., 1982; Luyendyk et al., 1985; Crouch and Suppe, 1993; Dillon and Ehlig, 1993; Powell, 1993; Nicholson et al., 1994; Dickinson, 1996; Fritsche et al., 2001, Jacobson et al., 2011).

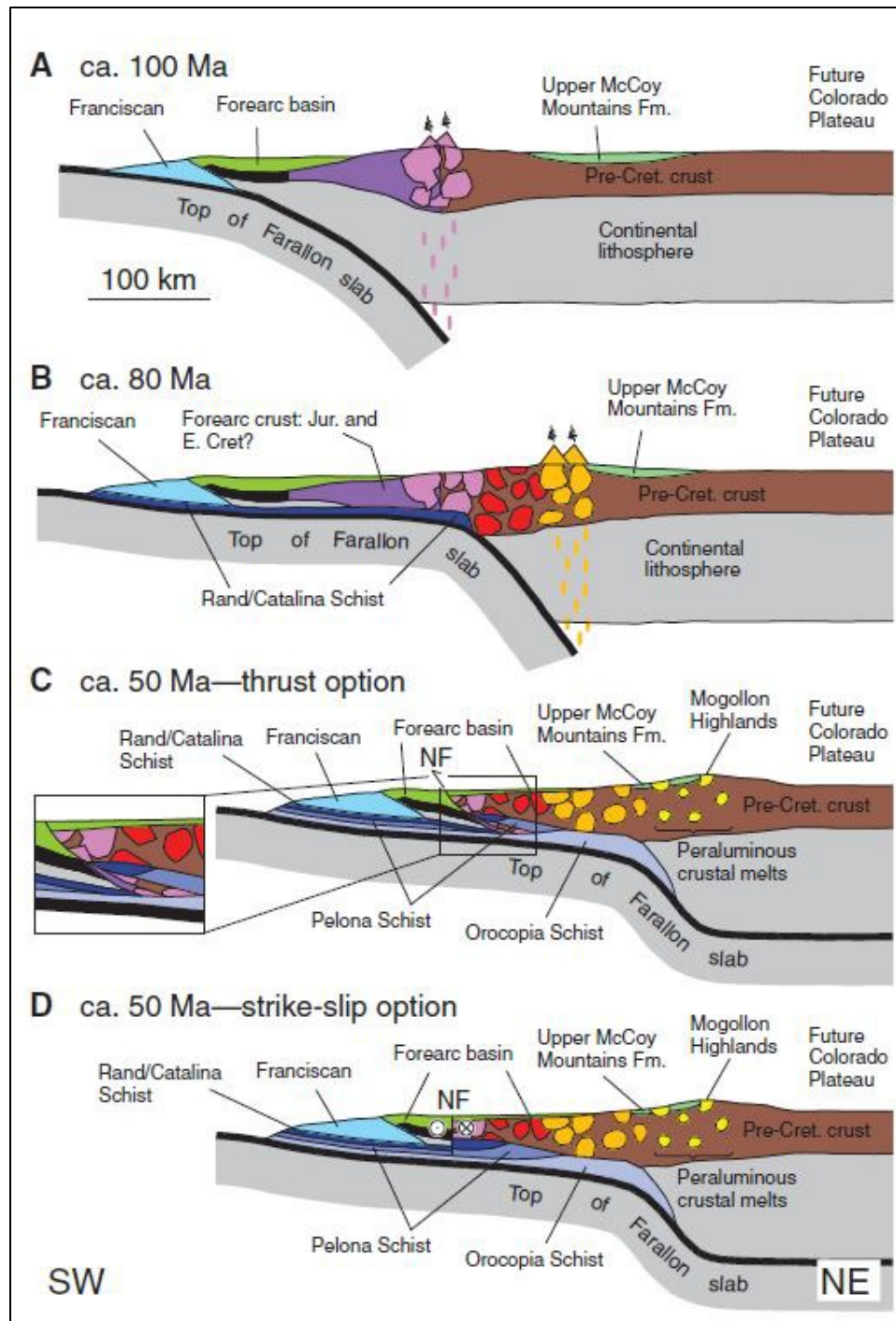


Figure 5. Model showing formation of the Rand/Catalina/Pelona/ Orocopia schists. A) Initial normal subduction of the Farallon plate beneath the North American arc crust and craton. B) Initiation of flat subduction of Farallon slab and underplating of trench sediments and emplacement of Rand/Catalina schists. C) Thrust option model for removal of the fore arc basin suite and inboard migration of magmatic arc. Thrusting predates emplacement of Pelona schist. D) Strike slip option model for removal of fore arc basin suite along Nacimiento fault. The authors favor a sinistral displacement option. Also shown is inboard migration of magmatic arc and emplacement of Pelona schist (source: Jacobson, 2011).

Research Questions

To address the objectives outlined in the first section of this thesis, I consider the following Research Questions:

General Geology

1. What is the general layout of the rock units (rock type, foliation trends, stratigraphy, exposed structural thickness)?
2. Does metamorphic grade vary from deep to shallow structural levels?

Folding

1. What are the orientations and geometries of outcrop scale folds; systematic or random; symmetric or asymmetric with measurable shear sense?
2. What are the orientations and geometries of map scale folds?
3. What is the relationship between outcrop scale and map scale folds? Specifically, are the small-scale folds parasitic S and Z folds, formed during development of map scale folds; or do they represent an earlier shearing event that has been overprinted by later map scale folding?

Faults

1. What evidence is there (if any) for late Cenozoic faulting and what is its significance?
2. Is the stratigraphy disrupted by hypothesized N-NE cross faults? If so, what are the fault types and how much displacement?

Geochronology

1. Is there a structurally deep to shallow variation in detrital zircon signature?
Specifically, is there a younging trend up-section, or is the section inverted?
2. How does the detrital zircon age and provenance signature compare with the two Blue Ridge samples (70 grains total) reported by Grove et al. (2003) and Jacobson et al. (2011)?
3. How does the detrital zircon signature from Blue Ridge compare with that of Sierra Pelona, Mt. Pinos, the Orocochia Mountains, and the adjacent East Fork Block?

Regional Tectonics

1. What do the syn-metamorphic structures and provenance signature reveal about the nature and configuration of the convergent plate boundary during late Cretaceous- early Paleogene (Laramide) time?
2. How does Blue Ridge fit into models for reconstruction of the San Andreas fault system?

Methods

Field Investigation - Attitude/Folds/Sample Collection

Geologic mapping of the stratigraphy, foliation attitudes, and fold measurements were carried out using a Brunton geologic transit compass. Fault striations and planes, sparsely exposed in outcrop within the eastern Blue Ridge block, were also measured with a Brunton compass, and slip sense of the fault surfaces was evaluated in the field

using criteria described and illustrated by Petit (1987). All structural data was analyzed using the Stereonet 10.0 (Allmendinger, 2011-2018).

Geologic Map Construction

GPS waypoints of geologic measurements and stratigraphic data were plotted on geo-registered versions of the Mescal Creek, CA, and Mount San Antonio, CA; USGS 7.5-minute quadrangle base maps using the Oziexplorer mapping program by D & L Software Pty Ltd. Adobe PDF's of subareas with detailed geologic data were then overlain on the same base maps in Adobe Illustrator to create the geologic map using standard geologic symbols. Stratigraphic units within the schist body were color coded to reflect representative mineralogies and mapping of the stratigraphy was carried out using foliation measurements to project subunits across hillslopes to determine general dip patterns and stratigraphic continuity of the schist body.

Cross-section Construction

Cross-sections were constructed using Adobe Illustrator. Initially, I considered constructing cross-sections on paper with the intention of scanning into Illustrator for finish work, but this approach was abandoned early in the process since the most accurate representation of the subsurface was needed in this study to determine stratigraphic continuities/discontinuities and the possible presence of concealed faults. I decided instead to create cross-sections entirely in Illustrator, despite the great increase in time needed to produce the cross-sections. The result is that apparent dip values, map-scale axial planes and stratigraphic thickness can be maintained at much greater accuracy than by using pencil, paper, and protractor.

Standard scale calculations were used to determine length and height values of the cross-sections and no vertical exaggeration is included in the vertical axis. In cases where the strikes of foliations were not perpendicular to the cross-section line, apparent dip values were calculated using the standard formula relating the tangent of the apparent dip value to the tangent of the angle between the measured strike and the cross-section line multiplied by the cosine of the measured dip value. Unit thickness is assumed to be constant since no field observations showed otherwise. However, this assumption may not be absolutely true. The axial planes of folds were determined first by bisecting the angle formed by the apparent dip values of the folds, and second, by using stereonet solutions to determine the fold axes. The two axial planes were then checked for reasonable agreement. In cases of generally parallel map scale folds, individual axial plane solutions determined for each fold were used, and not the average axial plane for the fold set. This was done to preserve the accuracy of the mapping and to possibly identify any later deformation of the fold sets. Unfortunately, in the interest of time conservation, the folds were left angular in appearance, but this will not affect the interpretation of the folding patterns in the cross-sections.

U-Pb Geochronology

Five samples of quartzofeldspathic gray schist (metasandstone unit) were collected for U/Pb detrital zircon age analysis from two sections where stratigraphy appeared to be coherent. Three samples, JNCM1942, 1943, and 1947, were collected by Dr. Nourse and myself in October 2019. Two additional samples, JN2056 and JN2060, were collected by Dr. Nourse during May 2020 and provided for this study. Finally, a metasandstone sample from the East Fork block (JN 2161) was collected by Dr. Nourse

and Garrett Stewart from Lupine Camp (south of the Punchbowl fault in Cabin Fork drainage) in August 2021. Bulk samples of the gray schist were collected in 2 kg bags and were processed in the Cal Poly Pomona rock lab using standard density, magnetic, and heavy liquid separation procedures including:

- Crushing the bulk samples mechanically and machine grinding into approximately 0.3 millimeter or smaller fragments.
- Gravity separation of the sample using the Gemini table to produce Grade A and B separates.
- Magnetic separation of Grade A and B fractions using a Frantz magnetic separator in horizontal and vertical modes.
- Heavy liquid separation of the Grade A and B fractions using Lithium Metatungstate.
- Drying separates under a heat lamp for 24 hours.
- Sorting of zircon grains from the separate and mounting on a slide using resin.
- Grinding of the slide to expose the interior of the zircon grains.

Detrital zircon mounts were analyzed at California State University Northridge. U-Pb ages are accepted for analysis in this study using a 70–110% concordance filter. Ages older than 800 Ma use $^{207}\text{Pb}/^{206}\text{Pb}$ ages.

DATA/RESULTS

Schist Subunits and Protoliths

The Pelona Schist of Blue Ridge is subdivided into 9 field-described subunits as delineated by various colors on the geologic map of Plate 1 (Appendix A). Sample sites representative of hand specimens and geochronology samples are also located on Plate 1.

Mineral assemblages observed in the field are augmented by corresponding thin section analyses described in more detail below (see Table 1).

By far the most abundant map unit is a muscovite-bearing quartzofeldspathic **grayschist**, derived from graywacke sandstone, siltstone, and associated pelitic muds. The grayschist is subdivided into three varieties based on chlorite content and weathering character. Less abundant are interlayered bodies of **mafic schist**, probably derived from submarine basalt or basaltic andesite flows. These are subdivided into actinolite-epidote greenschist, hornblende-rich schist, and spotted mafic schist. Very subordinate to the grayschist and greenschist are layers of **calcsilicate gneiss** and **quartzite** derived from siliceous carbonate and chert, respectively. These lithologies form important marker units useful for assessing possible Cenozoic fault disruption of the Blue Ridge stratigraphy. Finally, three varieties of **banded schist** mapped on Plate 1 represent places where different varieties of grayschist and mafic schist are interlayered on a decimeter scale, rendering a banded appearance to the outcrop. Essential details of the Blue Ridge schist subunits are described below:

Grayschist

All three grayschist subunits contain significant muscovite with variable proportions of chlorite. Where the rock is light gray and exhibits a silvery sheen, it is mapped as “muscovite-rich grayschist” (Figure 6). A “chlorite-rich” variety of grayschist has greenish hue, but still exhibits a phyllosilicate shimmer due to the mixture of muscovite a chlorite. A third subunit of grayschist that weathers light yellowish-brown contains more chlorite as well as epidote and possible actinolite. This subunit is

distinguished in a couple places to emphasize discontinuity of the stratigraphy between ridges.



Figure 6. Outcrop of muscovite-rich grayschist exposed on slope north of Blue Ridge campground.

Thin sections reveal that most grayschists contain garnet and epidote, the former likely derived from clay minerals in the protolith. Sphene (titanite) is also a common accessory mineral. Although the muscovite, garnet, and chlorite are indicative of a pelitic bulk composition, the epidote and sphene suggest a calcareous component that might be expected from graywackes derived from magmatic arc source regions.

In many grayschists, chlorite has been partially or completely upgraded to biotite. This transition is typically observed only in thin section, e.g., geochronology sample JN

2056 (Figure 7). In some cases, such as geochronology sample JN 2060 at microwave camp, biotite forms porphyroblasts larger than 1 mm, and chlorite is absent. Both of the above samples also contain abundant garnet, confirming a lower amphibolite facies metamorphic grade.



Figure 7. Close up of metasandstone geochronology sample JN 2056, collected northwest of Blue Ridge campground. In thin section, this sample contains garnet and displays replacement of chlorite with biotite.

Mafic Schist

Mafic schist is easily distinguished from greyschist in the field on the basis of sharply contrasting green or black coloration and lack of muscovite sheen. Subunits mapped as “greenschist” preserve the classic albite-epidote-amphibolite facies mineral assemblage with epidote, chlorite, and actinolite visible in hand specimen, imparting a distinctive

dark-green color (Figures 8, 9). Garnet is commonly observed in thin section. The hornblende-rich mafic schist subunit is noticeably black in the field, although several thin sections reveal that hornblende is intergrown with epidote and chlorite. Garnet was present in one sample. The hornblende schist is interpreted to be at slightly higher metamorphic grade than the greenschist in that it is assumed that actinolite has transitioned to hornblende. “Spotted mafic schist” is a third subunit that is probably a variety of hornblende-rich schist based on similar mineralogy. This rock is distinguished by large white albite porphyroblasts within a hornblende-rich matrix that results in a spotted appearance. One spotted schist (sample JNBR1811B) has biotite and epidote and garnet in the dark matrix, but no hornblende.



Figure 8. Greenschist unit of Northwest Ridge, viewed to the northwest toward Angeles Crest Highway. To the right of this photo is a thick underlying map unit of calcsilicate gneiss.



Figure 9. Close up of the Northwest Ridge greenschist unit.

In general, all of the mafic schist subunits have much lower abundance of quartz and muscovite compared to the grayschist. Most thin sections preserve abundant epidote and actinolite or hornblende with variable amounts of garnet. Biotite commonly replaces chlorite. Garnet is especially prominent at greenschist sample localities JN2062 and JN2058 (Figure 10). As described later, the observed mineral assemblages in the mafic schist subunits are collectively consistent with a mafic igneous protolith, metamorphosed to lower amphibolite facies.



Figure 10. Greenschist with brown garnet and white albite porphyroblasts, exposed in roadcut southwest of microwave camp at sample site JN 2058. This sample also contains abundant epidote and actinolite, along with minor biotite but no chlorite, confirming a lower amphibolite facies metamorphic grade.

Calcsilicate Gneiss

The most visually interesting subunit of the schist is a calcsilicate gneiss composed of recessively weathered carbonate-rich layers that alternate with resistant quartzite layers interpreted to be metachert. The gneiss commonly displays tight folds that result from contrasting competence between carbonate and metachert layers. Individual mappable calcsilicate gneiss layers vary in thickness from 1 m to > 50 m and are continuous along strike for hundreds of meters. Outcrops have a distinct orange color due to hematite content in the carbonite component (Figure 11). This rock is generally resistant and

sparsely vegetated compared to the surrounding greyschist and greenschist units. The calcsilicate gneiss outcrops with asymmetric Z and S folds shown in Figures 12-14 record a syn-metamorphic deformational event that is described later in the Structure section.



Figure 11. Calcsilicate gneiss underlain by greyschist on Microwave Ridge. View southeast toward Mt. San Antonio.



Figure 12. Outcrop of calcisilicate gneiss with west-vergent Z folds. View south towards Iron Mountain and East Fork San Gabriel canyon from Northwest Ridge.



Figure 13. Outcrop of calcisilicate gneiss with southwest-vergent S folds. This exposure is on the south slope of Blue Ridge, southeast of Microwave Ridge. View is to the northwest.



Figure 14. Metachert layers define S folds in calcsilicate gneiss from stratigraphic interval containing mixed Z and S folds on Northwest Ridge. View is to the south.

Six thin sections cut from the calcsilicate gneiss contain variable amounts of quartz and calcite (or dolomite), depending on where the samples were cut, in addition to garnet, diopside, hornblende, epidote, hematite, and muscovite. Biotite is present in one sample. These mineral assemblages are consistent with lower amphibolite facies metamorphism of a calcsilicate protolith.

Quartzite (metachert)

The least abundant subunit of the Blue Ridge schist is a light gray to light purple quartzite that tends to be associated with the greenschist unit (Figure 15). This rock resembles quartzites described from other bodies of the Pelona-Orocopia-Rand schist in southern

California and is similarly interpreted to represent metachert. Most layers have thicknesses between 20 cm and 1 m, with the exception of larger outcrops observed south of Inspiration Point and along the ridge transected by cross section E (described later). Like the calcsilicate gneiss unit, these metachert layers constitute important stratigraphic marker units as they appear to outcrop continuously for long distances. Unfortunately, few were encountered during the course of this study. No thin sections were cut from this unit.



Figure 15. Metachert layer associated with greenschist unit on east slope of Microwave Ridge

Banded Schist

Three varieties of this hybrid unit are mapped on Plate 1 to delineate areas of schist characterized by centimeter-to decimeter-scale compositional banding (Figure 16). At outcrop scale the banded schist displays alternating layers of muscovite or chlorite-rich

grayschist with greenschist. The mapped color corresponds to which lithology is most abundant. Four thin sections were cut from the banded greenschist subunit to assess compositional variability. The felsic layers were generally found to be garnet-muscovite±chlorite±biotite-quartz albite schist, whereas the mafic layers are muscovite±garnet-chlorite-biotite-epidote±actinolite±hornblende-albite schist.



Figure 16. Example of banded schist unit from folded region northwest of Blue Ridge campground.

Porphyroblastic Andalusite Schist

This distinctive rock was observed at only one place at the roadcut location of Sample JNCM1944. In the field it was best described as a quartz-mica schist with prominent 5-to-10 mm gray porphyroblasts. Analysis of 2 thin sections confirms the porphyroblasts to be andalusite. The assemblage of muscovite-garnet-biotite-andalusite-quartz±albite demonstrates a pelitic protolith (shale or clay-rich mudstone) and a lower amphibolite facies metamorphic grade.

Geologic Map and Representative Cross Sections

A detailed geologic map is presented in this section that illustrates the subunit distribution of portions of Blue Ridge, as well as general foliation patterns, fold axes, and sample locations (Plate 1, Appendix A). This new mapping is combined with previous reconnaissance level mapping by Dibblee (1967) and Elig (unpublished), Dibblee (2002), and Morton and Miller (2003) for greater coverage and context. Mapping of the subunits, cross-section lines, black foliation symbols, fold, and anticline/syncline axes are from this study. Subunits are color-coded and divided into; greyschist (light gray), green schist (green), hornblende-rich schist (black), spotted hornblende-rich schist (black with white spots), banded greyschist (light gray with dark gray bands), calc-silicate gneiss (orange), and metachert (red) (Figure 17). Additionally, a variation of greyschist that weathers yellowish gray is color-coded yellow to show stratigraphic discontinuity along ridgelines.

Previous mapping that is shown includes green foliation symbols from Dibblee (1967) and Elig (unpublished), and blue foliation symbols from Dibblee (2002). Blue foliation symbols with closed triangles are approximate measurements (Dibblee, 2002) and should be taken with a degree of uncertainty. Map Figures below are ordered from NW to SE and divided into subareas 1-3.

Geochronology sample locations are depicted in blue and thin section sample locations are depicted in purple. Note that thin sections were cut and analyzed for all geochronology samples as well.

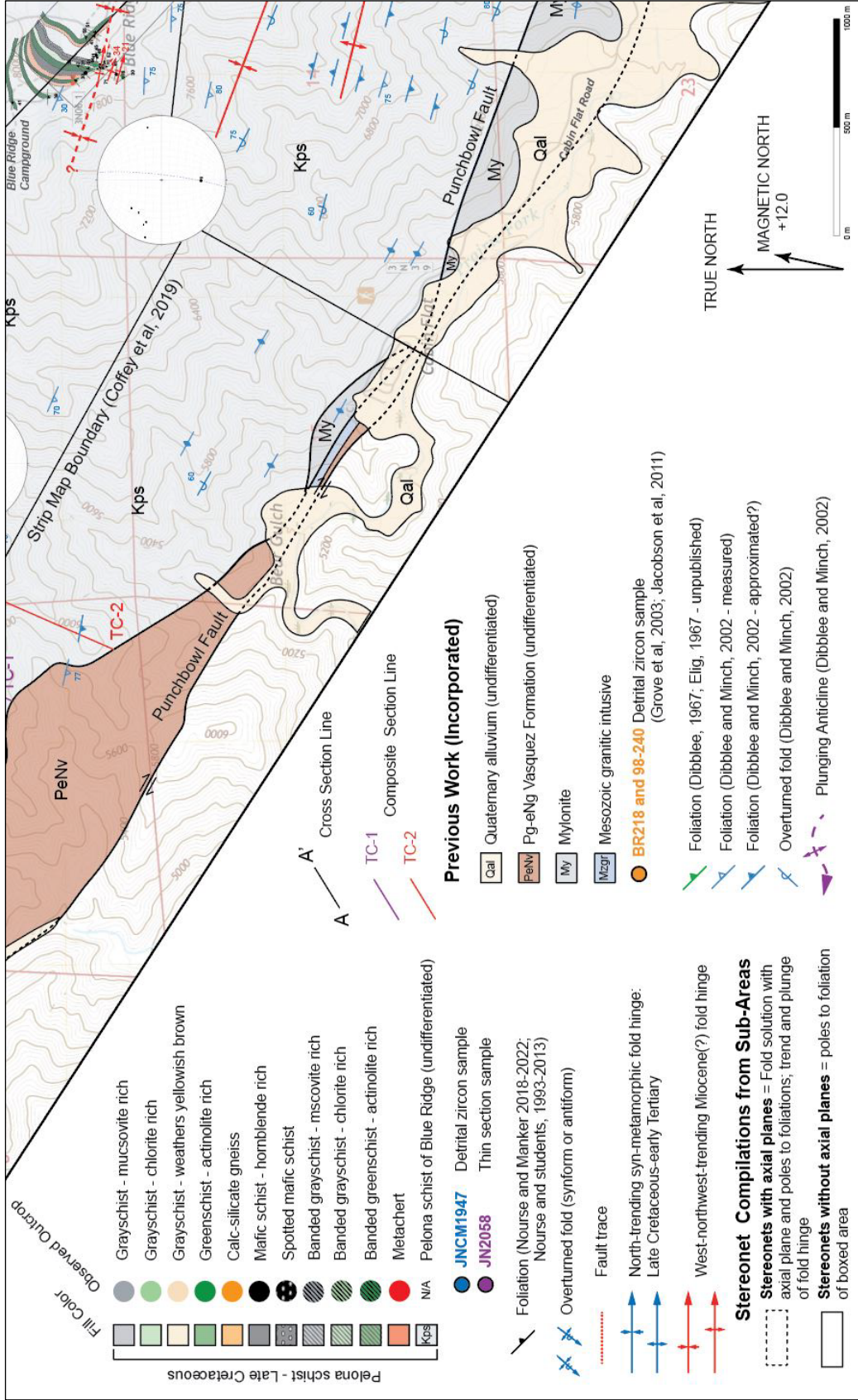


Figure 17. Map legend for the following map Figures.

Field mapping shows that gross foliations in the northwest area are generally dipping to the south or southwest (see geologic map Plate 1; and cross-sections A-E, Figures 18-24). Several dip reversals on the south slope of Blue Ridge define a series of west-northwest trending folds. However, just east of sample JNBR1814, a marked change in foliation strike occurs. A tightly folded section with north-northeast trending hinges defines the structure until sample JN2057 where southwest dips resume. In the vicinity of Blue Ridge Camp, the foliations define a consistently east-southeast-dipping section of schist at least 1,374 meters thick (see geologic map Plate 1 and cross-section G, Figures 23 and 24). East of sample JN2060 are several dip reversals that define northerly trending fold hinges.

The belt of schist with northerly-striking foliations and relatively tight folds (with short wavelengths) continues to Guffy Camp. This structural style contrasts with foliation patterns mapped by Dibblee (2002) on the north and south slopes of Blue Ridge, and by Nourse and Stewart (this study) along Cabin Fork Road south of Guffey Camp. In those areas, foliations generally strike northwest, and dip reversals define map scale folds with longer wavelengths and northwest-trending hinges. Cross-sections have been selected to show both map-scale fold sets and to test for stratigraphic continuity.

Subarea 1 (Figure 18) contains five cross-section lines (A-E,) that generally follow ridgelines where the schist is particularly well exposed. In map view, the area of cross-section A is dominated by grayschist (due to time constraints, this cross-section was not illustrated). This contrasts with the area of cross-section B (Figure 19) which is comprised of variable grayschist, greenschist and a conspicuous layer of calc-silicate gneiss which does not appear to project to the west along strike. This apparent

stratigraphic discontinuity is repeated on the ridges of cross-sections C and D (Figures 20 and 21) where marker beds of calc-silicate gneiss on ridge C do not appear to project along strike to ridge D. Additionally, a subunit of grayschist on ridge D that weathers yellowish gray does not project along strike to ridge C. Further to the east, the ridge marked by cross-section E (Figure 22) is dominated by banded grayschist which is overlain by green and gray schists and a marker bed of calc-silicate gneiss. Beneath the banded schists, are thick beds of grayschist. This ridge does not appear to line up stratigraphically with ridge D either. The possibility of faults offsetting the stratigraphy in this area is discussed further in subsequent sections of this paper.

The ridges marked by cross-sections A-E exhibit bands of east-west to northwest trending folds located on the south slope of Blue Ridge. In contrast, the area marked by cross-section F (Figure 24) is dominated by complex northeast trending folds (previously described) within banded and un-banded grayschist.

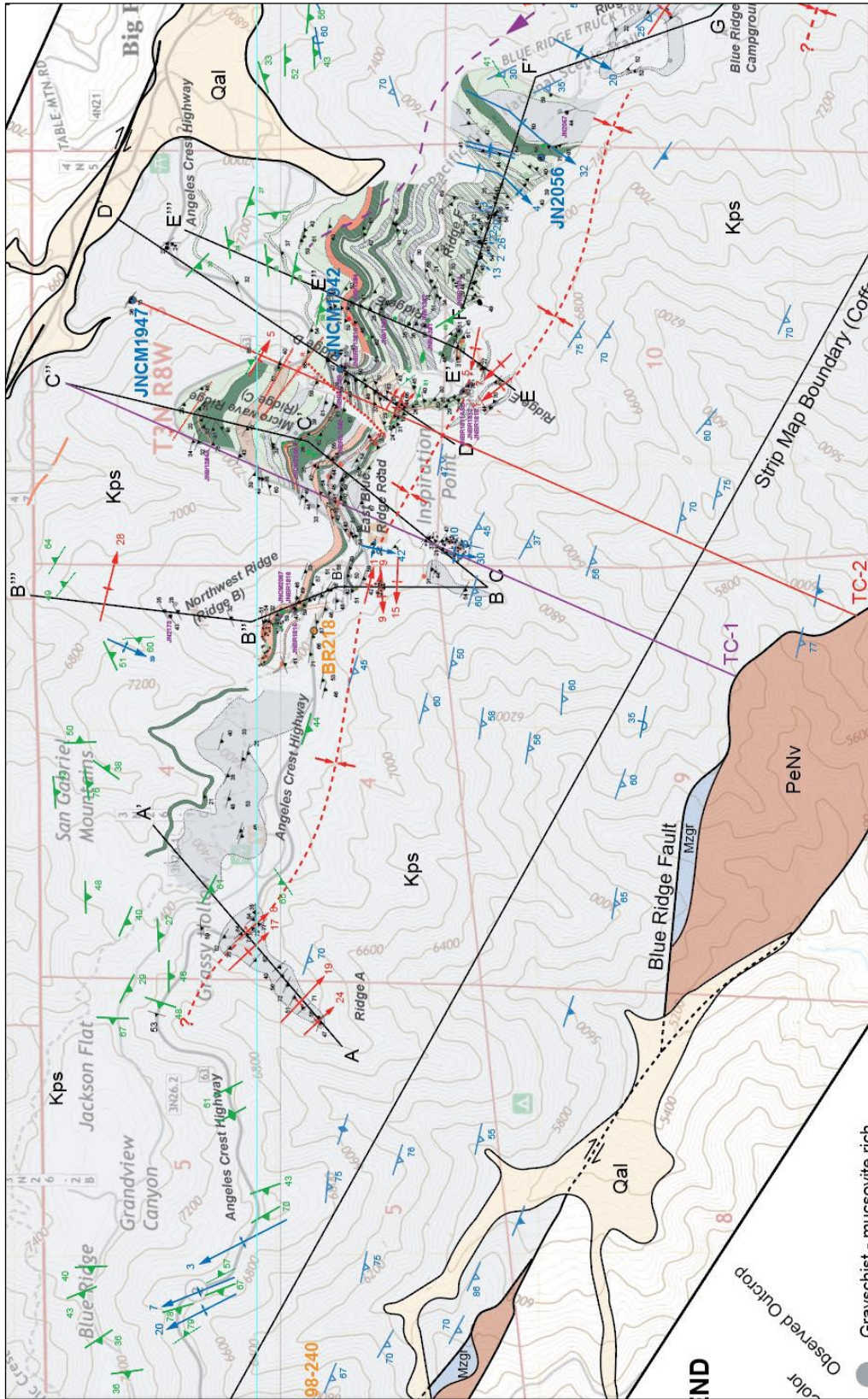


Figure 18. Geologic map of subarea 1.

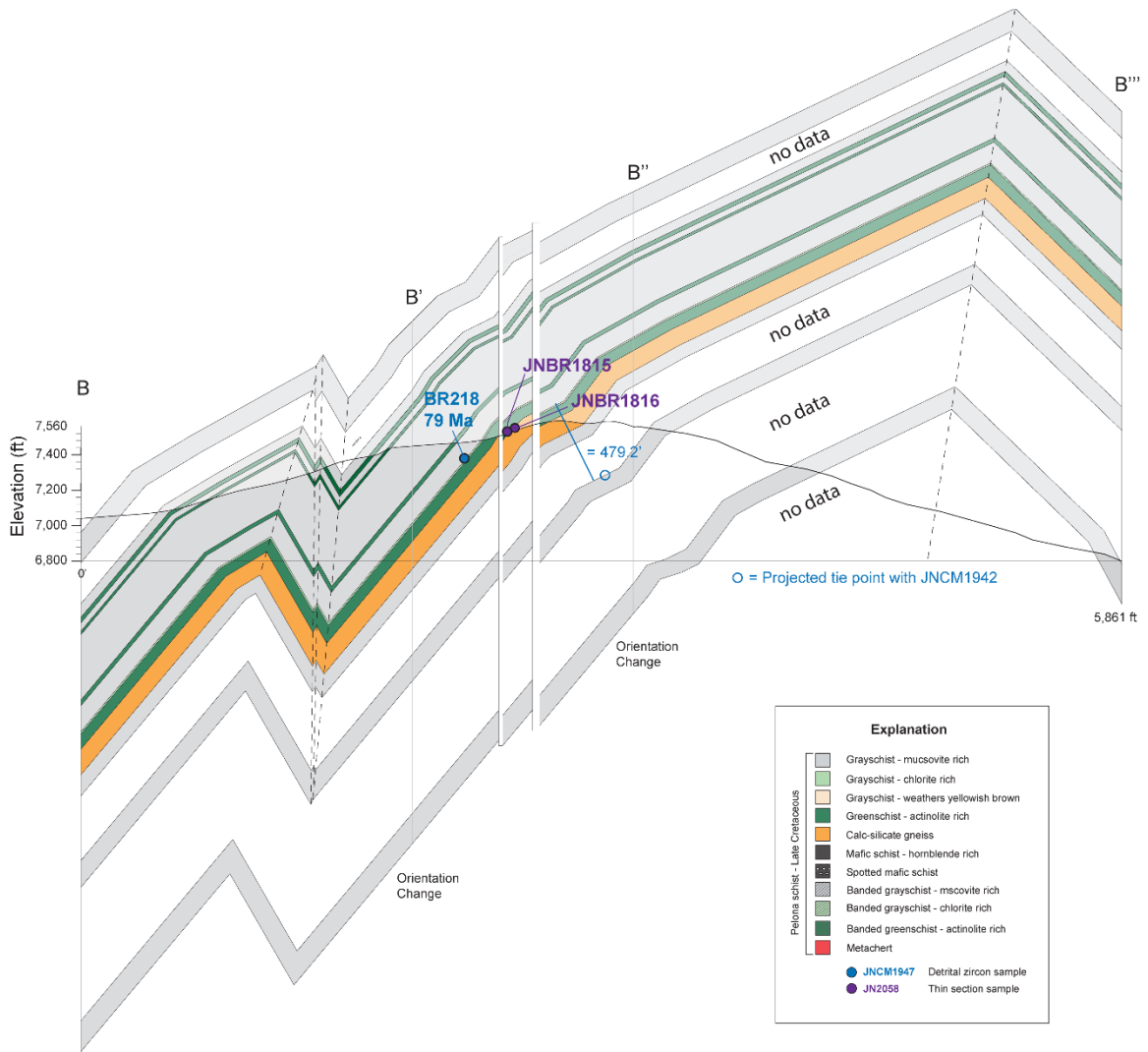


Figure 19. Cross-section B showing folding in variable schist and offset calc-silicate layering. Folds verge to the northeast. Note that basal subunits consist of grayschist (quartzofeldspathic schist) and upper subunits consist of calc-silicate gneiss and greenschist (mafic schist) indicating that they are interlayered or interleaved. Geochronology sample site BR218 (Grove et al., 2003; Jacobson et al., 2011) is shown with YSG age.

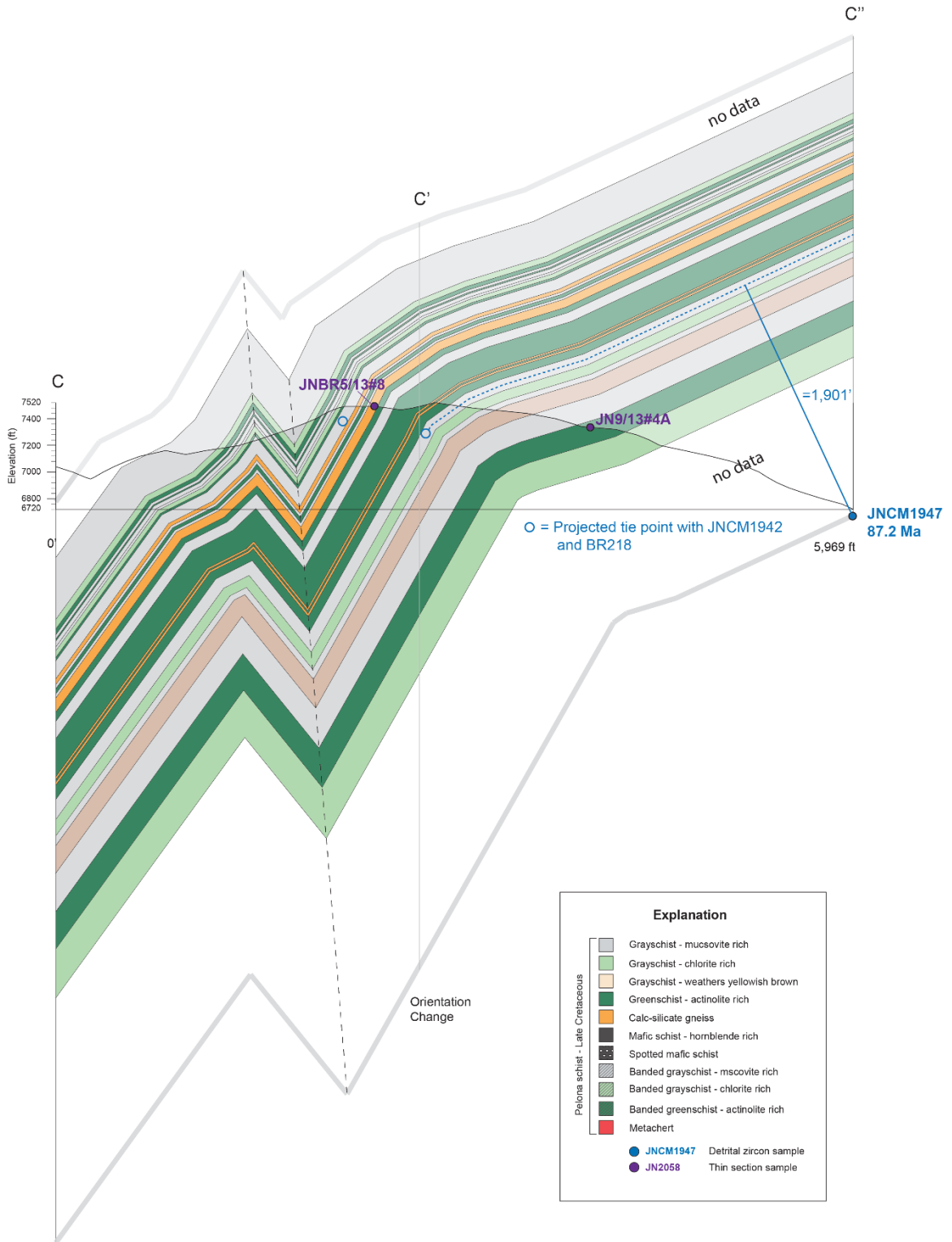


Figure 20. Cross-section C showing folding and variable schist with four calc-silicate layers. Note basal and upper grayschist. Geochronology sample site JNCM1947 is shown with YSG age.

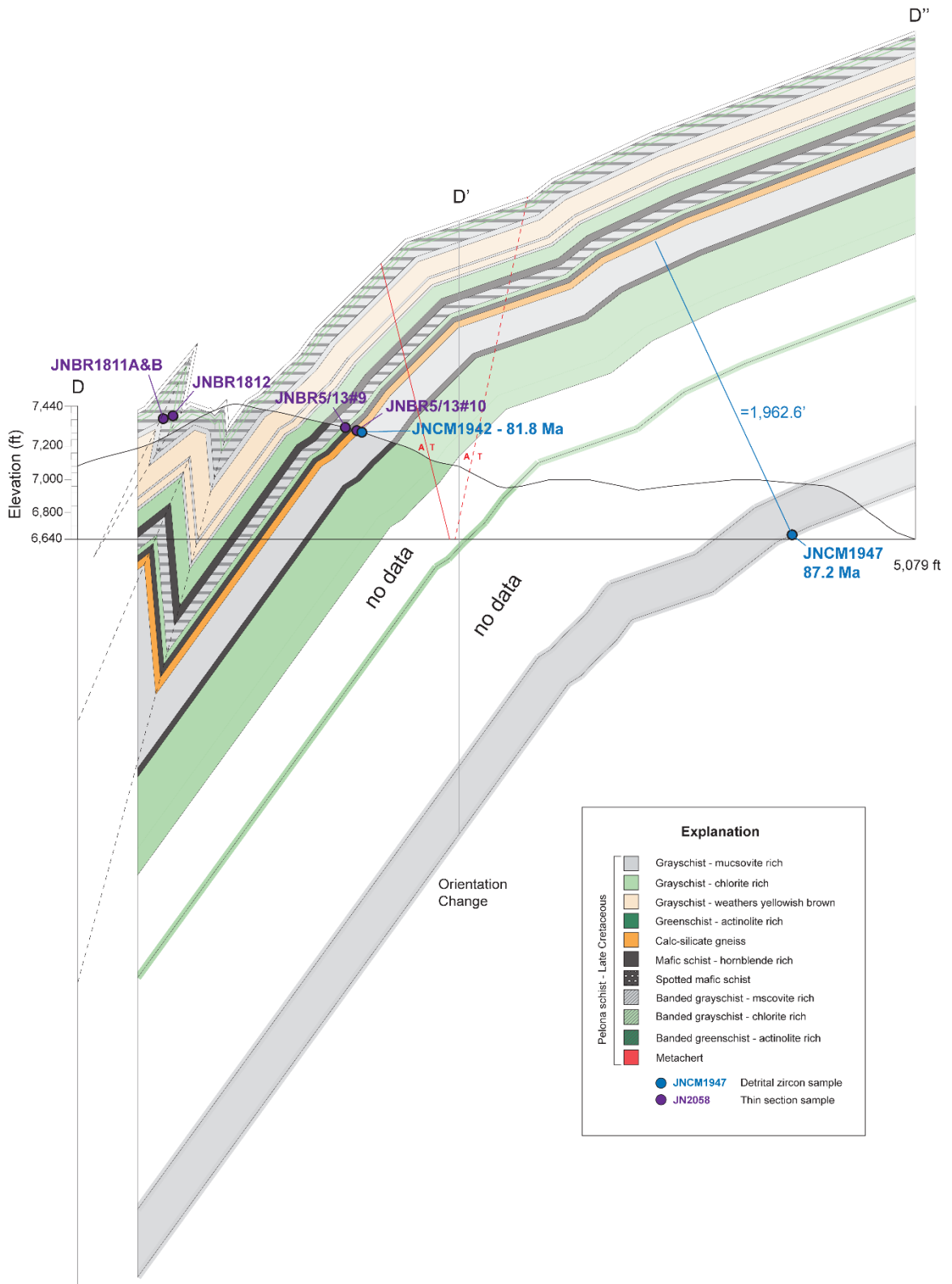


Figure 21. Cross-section D showing complex folding in banded schist of upper section. Folds verge NE.

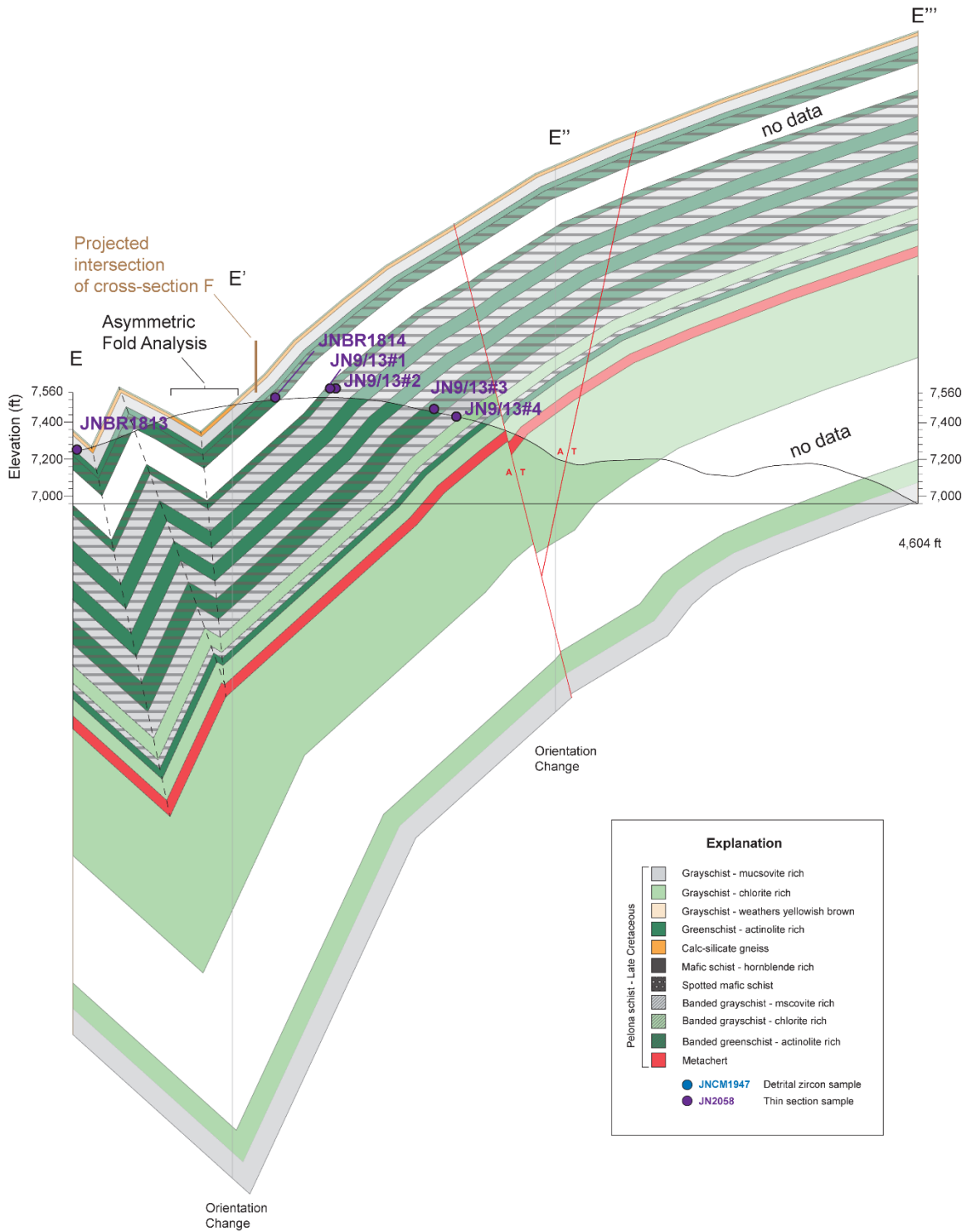


Figure 22. Cross-section E showing folding in pre-dominantly banded gray and greenschist underlain by mostly chlorite -rich grayschist. Folds verge to the SW. Red lines indicate Reidel shears (R and Y) synthetic to San Andreas fault system.

In subarea 2 (Figure 23) cross-section G (Figure 24) follows the northwest-southeast trending spine of Blue Ridge and maps relatively un-interrupted stratigraphy dipping to the southeast with several dip reversals indicating northeast trending folds. Cross-section G is characterized from northwest to southeast by an initially south dipping foliation pattern that changes to a southeast dipping foliation pattern. This defines a narrow band bordered to the northeast and southwest by previously mapped foliation patterns dipping to the southwest and south respectively. To the south, previous mapping of the foliations by Dibblee and Minch (2002) indicates the presence of west-northwest trending folds. Lithologically, cross-section G is diverse with alternating beds of greenschist, greenschist, hornblende-rich mafic schist, metachert, calc-silicate gneiss, and banded schist. Note, cross-sections F and G have been combined in illustration to preserve stratigraphic continuity between geochronologic samples (Figure 24).

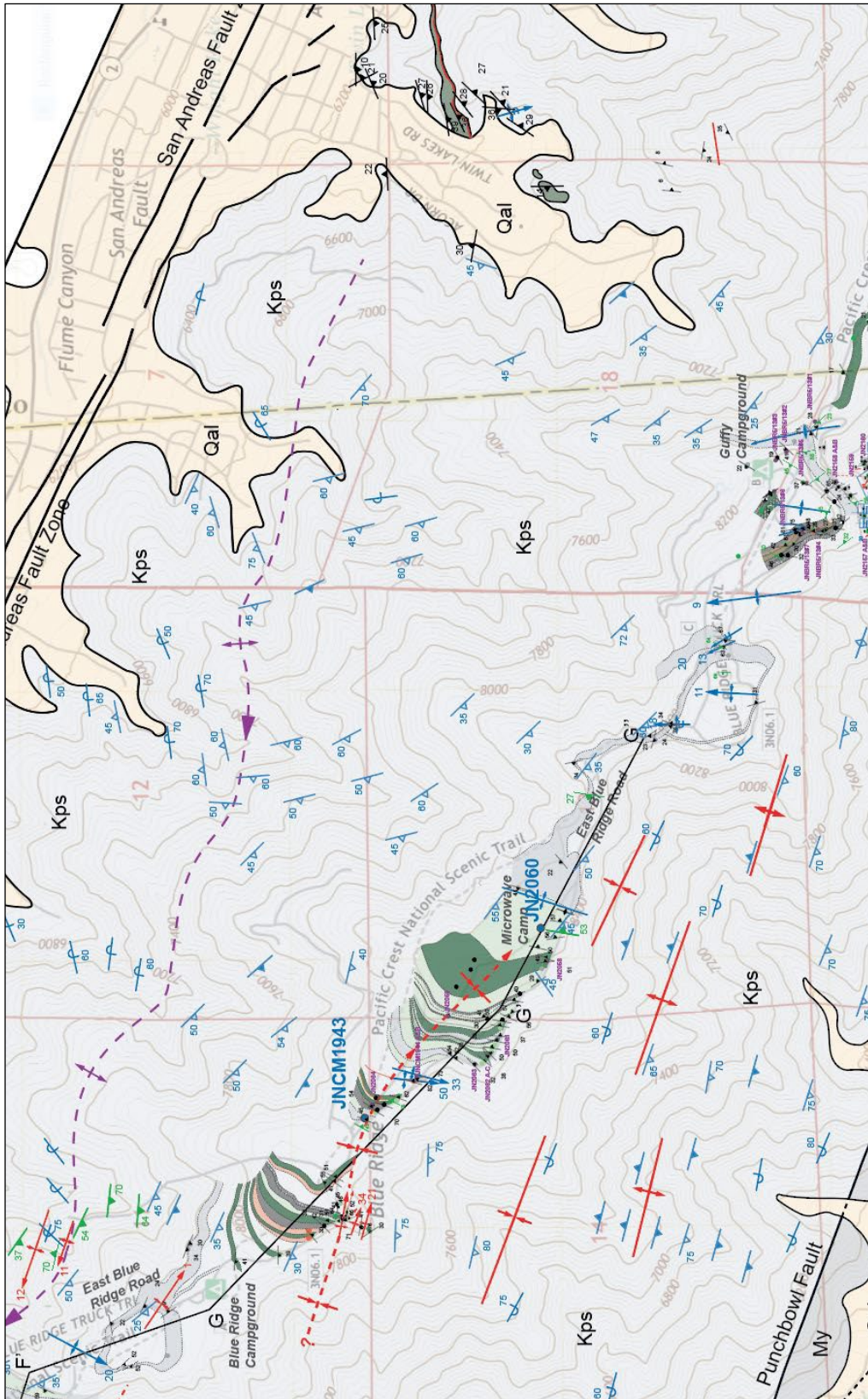


Figure 23. Geologic map of subarea 2.

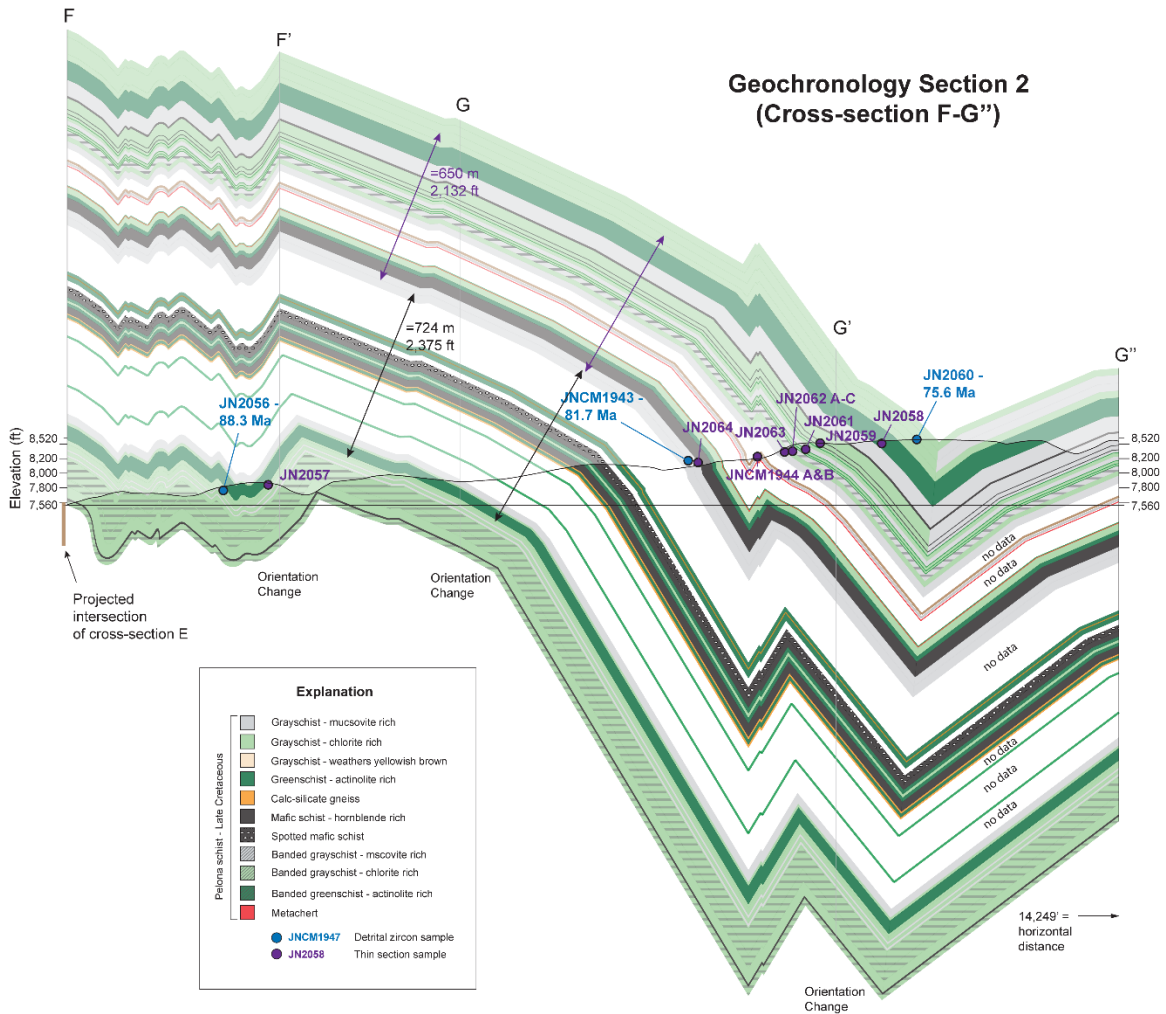


Figure 24. Cross-sections F and G, combined here for the purpose of geochronology sample tracing. Note complex short wavelength folding in cross-section F contrasting with longer wavelength folds in cross-section G. Folds verge sub-vertically to the NW and SE.

Subarea 3 (Figure 25) is characterized by detailed mapping of the Guffey Camp area and areas to the south that approach the trace of the Punchbowl fault. Complex folding is pervasive, indicating west-northwest to northwest trending folds and north-northwest trending folds. Some of these folds have asymmetries indicating top-to-the-southwest vergence. Previous mapping of foliations to the west and north of Guffy Camp show foliation patterns dipping to the west and southwest respectively. Farther east,

foliations on the southwest face of Wright Mountain generally dip south, with some dip reversals that define easterly fold hinges.

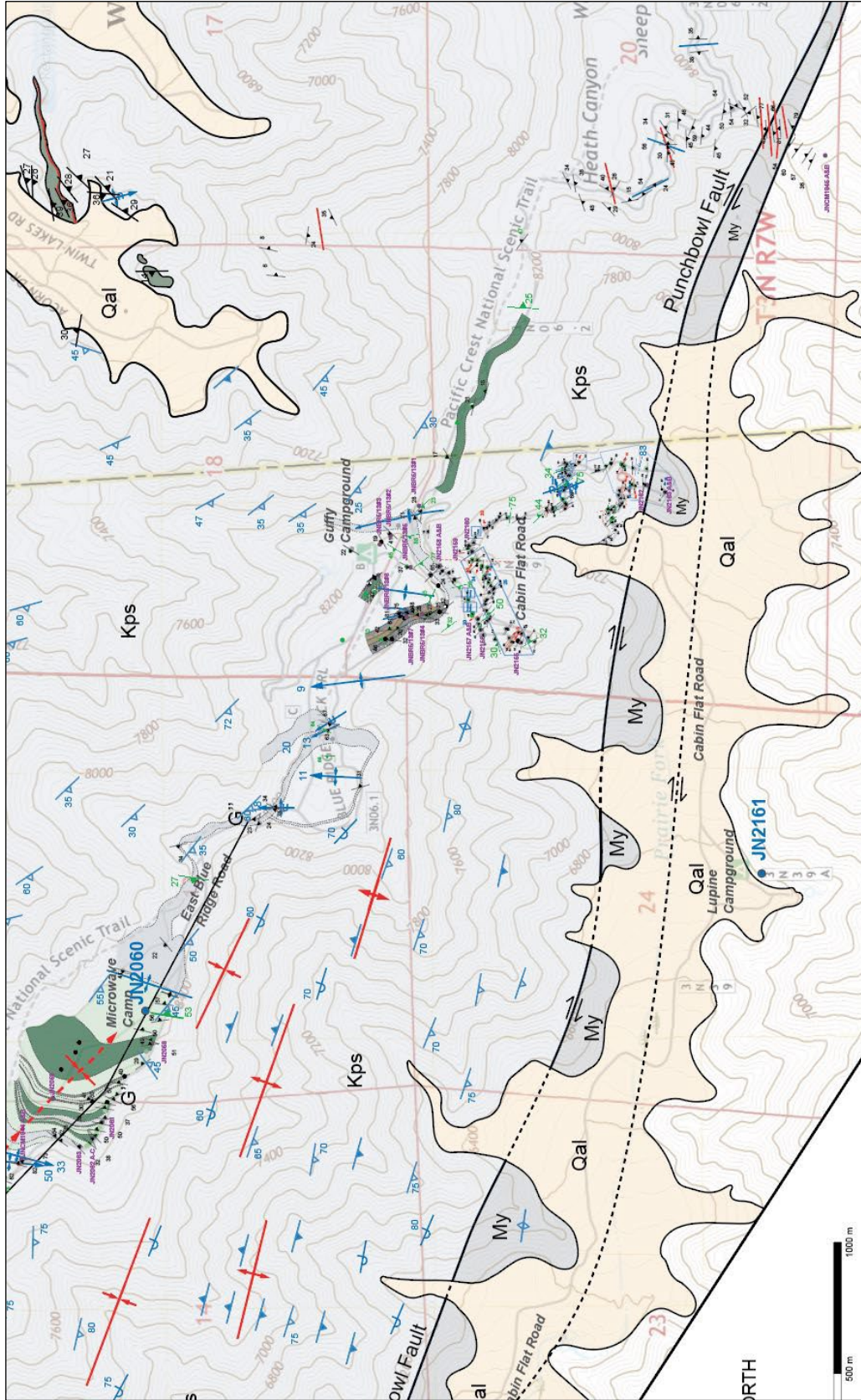


Figure 25. Geologic map of subarea 3.

Thin Section Analysis

Dr. Nourse carried out petrographic analysis of representative rock samples and thin sections from Blue Ridge during summer 2020 as part of his preparation work for “virtual” mapping projects for GSC 5030L and GSC 4910L. Additional thin sections were cut and analyzed during spring and summer of 2021. Table 1 presents a summary of observed mineral phases in 62 thin sections. The primary emphasis was to assess protolith types and metamorphic grade. Included for comparison are descriptions of several thin sections cut from the East Fork block and Sierra Pelona. Sample locations are plotted on Plate 1 and various cross sections of Figures B, C, D, E, and F-G’. To evaluate potential up-section variations in metamorphic grade, the samples are listed from shallow to deep structural level for each given sub-area.

Protolith

Using general guidance provided in Tables 17-1, 19-1, and 20-1 of Williams, Turner and Gilbert (1972) and p. 384-385 of Best (1982), six general protolith types may be inferred from the bulk compositions of metamorphic mineral assemblages of Table 1. Following previous studies of the Pelona-Orocopia-Rand schists (Muehlberger and Hill, 1958; Ehlig, 1981; Graham and Powell, 1984; Jacobson, 1983a, 1990, 1995), four main protoliths (graywacke, mafic igneous rock, chert, and dirty carbonate) occur in abundance on Blue Ridge. Metamorphic counterparts of these protolith types are subdivided into the units mapped on Plate 1.

The most abundant rock unit in the study area is **muscovite ± chlorite grayschist**. In addition to quartz and albite that predominate, and ubiquitous epidote, this rock yields abundant aluminous minerals (muscovite, biotite, and garnet). Chlorite is present in

several samples, but commonly transitions to biotite. The mineral assemblage is generally indicative of a pelitic protolith with a strong quartzofeldspathic component (Williams, Turner and Gilbert, 1972). In accordance with previous studies of the Pelona-Orocopia-Rand schists cited above, the greyschist is interpreted to be derived from a graywacke / turbidite sequence, deposited in a trench setting at the Farallon-North American convergent plate boundary.

The **greenschist and mafic schist** subunits generally contain much lower amounts of quartz and muscovite, although the “banded greenschist” samples preserve thin layers of garnet-muscovite-quartz-albite that alternate with darker layers rich in mafic and calcareous minerals. Ubiquitous occurrence of sphene, garnet, hornblende (and/or actinolite), albite, and sometime chlorite are strongly suggestive of a mafic igneous protolith; i.e., basalt or gabbro or basaltic andesite (Williams, Turner and Gilbert, 1972).

The **calcsilicate gneiss** subunit is distinguished by alternating bands of rusty carbonate mineral and quartz. Observed mineral assemblages are rich in calcite (or dolomite) and quartz, and contain variable amounts of garnet, amphibole, and sometimes diopside. This assemblage corresponds to “calcsilicate” or “calcareous” protolith types of Williams, Turner and Gilbert (1972).

A fourth subunit, **metachert**, was not sampled for thin section analysis. Hand samples contain quartz and minor muscovite. Spessartine garnet is probably abundant, as it is in metacherts of Sierra Pelona (Graham and Powell) and the Rand Schist (Jacobson, 1995; Nourse, pers. comm., 2022).

Two thin sections (JNCM1944A&B) were cut from a rare outcrop of muscovite-rich schist with distinctive coarse porphyroblasts. The assemblage of muscovite-garnet-biotite-andalusite-quartz (Table 1) indicates a strongly aluminous (pelitic) protolith, probably a shale given relatively low percentage of albite porphyroblasts that distinguish the metagraywacke protolith.

Finally, several samples contain mineral assemblages suggestive of ultramafic protoliths (Table 1). These include two samples very rich in actinolite or talc, (interpreted to be metamorphosed peridotite or dunite), and two amphibolite samples with very high color index that contain epidote and hornblende but no albite, potentially derived from pyroxenites. The protoliths of these samples are debatable at these metamorphic grades.

In general, the inferred protoliths for the collection of thin sections in Table 1 (graywacke, basalt, chert, dirty carbonate) are compatible with a marine trench or accretionary prism depositional setting. The mechanism for causing the observed repetitive interlayering of the greyschist, mafic schist metachert and calcsilicate gneiss subunits at Blue Ridge remains a subject of debate that is relevant to the Pelona-Orocopia-Rand schists in general.

Metamorphic Grade

Assessment of metamorphic grade draws heavily upon detailed electron microprobe work and thermo-barometric studies of Sierra Pelona (Graham and Powell, 1984), the East Fork block (Jacobson, 1983a), and the Rand Mountains (Jacobson, 1995). Graham and Powell documented an inverted metamorphic gradient (increasing grade up section) in Sierra Pelona, based on systematic distribution of three groups of index minerals developed in “metabasite,” metagraywacke, and metachert bulk compositions.

Identified metamorphic zones include greenschist facies, garnet—bearing albite-epidote-amphibolite facies, and garnet-hornblende-bearing oligoclase amphibolite facies. A similar inverted metamorphic gradient, including a deeper level blueschist zone, was documented in the Rand Mountains by Jacobson (1995), but most samples collected from the East Fork-Fish Fork area of the East Fork block show only subtle upward metamorphic grade increases within the greenschist facies as the Vincent thrust is approached (Jacobson, 1983a). Additional helpful guidance for assessing metamorphic grade from index minerals is provided by Tables 19-2 and 20-2 of Williams, Turner and Gilbert (1972).

Two general conclusions are drawn from the mineral assemblage data on Blue Ridge:

(1) The majority of Blue Ridge schist subunits were metamorphosed at lowermost amphibolite facies, or at the boundary between greenschist and amphibolite facies. Without detailed electronic microprobe work such as that described by Graham and Powell (1984) and Jacobson (1995), metamorphic grade determination is based on qualitative analysis of mineral assemblages. Many of the semi-pelitic greenschist samples contain garnet and biotite; commonly chlorite is observed to be replaced by biotite. Chlorite and biotite together are suggestive of the transition from greenschist to uppermost greenschist facies. The greenschist and mafic schist samples frequently contain hornblende and garnet. A few contain actinolite and chlorite, but these also have hornblende and biotite, respectively, suggestive of the greenschist-lower amphibolite transition. The hornblende schists and spotted mafic schists probably represent the oligoclase zone of amphibolite facies. Muscovite, epidote, quartz, and feldspar occur in

all of the greyschists and most greenschists, but these are not good index minerals for metamorphic grade. The calcsilicate gneiss subunit contains garnet and rare diopside, again suggesting metamorphic grades higher than greenschist facies.

(2) There does not appear to be a systematic up-section variation in metamorphic grade. Much time was spent correlating the samples to structural position on the cross-sections of B through FG'' (Figures 19-22 and 24), but unfortunately most are at similar upper greenschist-lower amphibolite metamorphic grades, despite an upward-younging relationship documented in detrital zircon data (see below). The one exception may be the Guffy Campground / Prairie Fork Road transect (Table 1), where the majority of hornblende schists and spotted mafic schists occur at higher structural levels. These rocks represent the highest metamorphic grades encountered in the Blue Ridge block (oligoclase zone of the amphibolite facies).

Comparison to Sierra Pelona and East Fork Blocks

A thin section of greyschist collected in Bouquet Canyon at fairly deep structural levels of Sierra Pelona. This sample contained coarse biotite but no chlorite or garnet and probably represents the transition from greenschist to upper greenschist facies. Five thin sections analyzed from the East Fork block preserve mainly greenschist facies mineral assemblages (see also Jacobson, 1983a). Two samples of green mafic schist from San Antonio Canyon (MB#2 and #6, derived from the Pelona schist of Mt. San Antonio) preserve a classic greenschist mineral assemblage (quartz-chlorite-epidote-actinolite-albite). A metasandstone sample (JN 2161) from Lupine Camp directly south of the Punchbowl fault contains no garnet or biotite, and grain size significantly finer than the greyschists on Blue Ridge. Two other samples of fine-grained greyschist-metasandstone

(JNCM1945A&B) collected along strike ~ 2 km contain biotite, but no garnet or chlorite, similar to the assemblage in the Bouquet Canyon sample.

As mentioned previously, uppermost greenschist and amphibolite facies mineral assemblages do occur at higher structural levels of Sierra Pelona, in proximity to the Vincent thrust (Graham and Powell, 1984). Blueschist facies mineral assemblages similar to those described by Jacobson (1995) from deep structural levels of the Rand Mountains do not appear to be exposed in the Sierra Pelona, East Fork, or Blue Ridge schist bodies.

Table 1. Thin Section Summary

Table 1: Central Blue Ridge Thin Section Summary									
	² Sample Number	³ UTM East	³ UTM North	Collected By:	Date Collected	Field Name	Metamorphic Mineral Assemblage	⁵ Metamorphic Grade	⁵ Inferred Protolith
Cross Section 1 Sub-Area	JNCM1947			Nourse&Manker		Grayschist	gt-ep-bio-musc-qtz-ab	lower amphibolite	pelitic graywacke
	JN2173			Nourse	8/28/2021	Grayschist	bio ² -act-sph-gt-ep-musc-qtz-ab	lower amphibolite	pelitic graywacke
	JN9/13#4A			Nourse		Greenschist	sph-chl-qtz-musc-ep-hbl-d-ab	lowermost amphibolite	basalt
	JNCM1942			Nourse&Manker		Grayschist	gt-bio-ep-musc-qtz-ab	lower amphibolite	pelitic graywacke
	JNCM2068			Nourse&Manker		Calcsillate Gneiss	musc-gt-qtz-calcite	lower amphibolite	dirty carbonate w/chert
	JNBR5/13#10			Nourse		Calcsillate Gneiss	mag-gt-hbl-d-musc-ep-qtz	lower amphibolite	dirty carbonate w/chert
	JNBR5/13#9			Nourse		Greenish Grayschist	bio-sph-musc-ep-chl-qtz-ab	uppermost greenschist	pelitic graywacke
	JNBR5/13#8			Nourse		Calcsillate Gneiss	ep-bio-calcite-qtz	lowermost amphibolite	dirty carbonate w/chert
	JNCM2067			Nourse&Manker		Greenschist?	qtz-gt-bio-ep-musc-ab	lowermost amphibolite	dirty carbonate w/chert
	JNBR1816			Nourse		Calcsillate Gneiss	hem-hbl-d-bio-qtz-calcite	lower amphibolite	dirty carbonate w/chert
	JNBR1815			Nourse		Greenschist	gt-sph-ep-chl-musc-qtz-ab	lowermost amphibolite	dirty carbonate w/chert
	JNBR1811A			Nourse		Banded Greenschist	musc-chl-bio-ep-ab interlayered w/ bio-musc-qtz-ab	lowermost amphibolite	basalt
	JNBR1811B			Nourse		Spotted Mafic Schist	sph-gt-qtz-musc-bio-ep-ab	lower amphibolite	basalt
	JNBR1812			Nourse		Grayschist	sph-act-ep-musc-qtz-ab	uppermost greenschist	pelitic graywacke
Cross Section 2 Sub-Area	JN2054			Nourse		Banded Greenschist	bio-sph-gt-chl-ep-musc-ab interlayered w/ gt-musc-bio-qtz-ab	lowermost amphibolite	basalt / pelitic graywacke
	JN2055			Nourse		Banded Greenschist	gt-musc-qtz-ab interlayered w/ chl-ep-act-bio-ab	lowermost amphibolite	basalt / pelitic graywacke
	JN2056			Nourse		Grayschist	gt-bio-chl-ep-musc-qtz-ab	lowermost amphibolite	pelitic graywacke
	JN2057			Nourse		Grayschist	bio-act-ep-musc-qtz-ab	uppermost greenschist	pelitic graywacke
	JN2064			Nourse		Amphibolite	hem-sph-qtz-ep-hbl-d	lower amphibolite	pyroxenite?
	JNCM1943			Nourse		Grayschist	gt-ep-hbl-d-act-musc-qtz-ab	lower amphibolite	pelitic graywacke
	JNCM1944A			Nourse&Manker		Porphyroblastic Schist		lower amphibolite	mudstone
	JNCM1944B			Nourse&Manker		Porphyroblastic Schist		lower amphibolite	mudstone
	JN2063			Nourse		Grayschist	gt-ep-bio-musc-qtz-ab	lower amphibolite	pelitic graywacke
	JN2062A			Nourse		Greenschist	mgt-ep-qtz-gt-ab-act	lower amphibolite	basalt
	JN2062B			Nourse		Greenish Grayschist	musc-ep-act-gt-qtz-ab	lower amphibolite	pelitic graywacke
	JN2062C			Nourse		Greenish Grayschist	bio-musc-ep-act-gt-qtz-ab	lower amphibolite	pelitic graywacke
	JN2061			Nourse		Greenschist	musc-ep-gt-act-bio-qtz-ab	lowermost amphibolite	basalt
	JN2059			Nourse		Amphibolite	gt-sph-qtz-ep-hbl-d	lower amphibolite	pyroxenite?
JN2058			Nourse		Greenschist	mgt-musc-bio-ep-gt-act-qtz-ab	lowermost amphibolite	basalt	
JN2060			Nourse		Grayschist	sph-gt-bio-musc-qtz-ab	lower amphibolite	pelitic graywacke	
Cross-section E Sub-Area	JN9/13#4			Nourse					
	JN9/13#3			Nourse		Banded Greenschist	sph-gt-chl-ep-musc-qtz-ab	lower amphibolite	basalt
	JN9/13#2			Nourse		Banded Grayschist	gt-bio--chl-ep-qtz-ab layers alternate w/ sph-act?-musc-chl-bio-ab	lowermost amphibolite	pelitic graywacke
	JN9/13#1			Nourse		Banded Grayschist	sph-gt-bio-chl-ep-qtz-ab	lowermost amphibolite	pelitic graywacke
	JNBR1814			Nourse		Banded Grayschist	sph-ep-chl-musc-qtz-ab	uppermost greenschist	pelitic graywacke
Guffy Camp/ PrairieFork Road Sub-Area	JNBR1813			Nourse		Greenish Grayschist	sph-bio-ep-chl-musc-qtz-ab	lowermost amphibolite	pelitic graywacke
	JNBR5/13#7			Nourse		Marble	musc-ep-calcite	upper greenschist	dirty carbonate
	JNBR5/13#6			Nourse		Greenschist	mgt-calcite-chl-qtz-ep-hbl-d-ab	lower amphibolite	basalt
	JNBR5/13#5			Nourse		Greenschist	mgt-calcite-qtz-bio-ep-hbl-d-ab	lower amphibolite	basalt
	JNBR5/13#3			Nourse		Greenschist	mgt-musc-chl-gt-ep-hbl-d-ab	lower amphibolite	basalt
	JNBR5/13#2			Nourse		Spotted Mafic Schist	mgt-musc-qtz-ep-hbl-d-ab	lower amphibolite	basalt
	JNBR5/13#1			Nourse					
	JN2158A			Nourse&Stewart		Spotted Mafic Schist	gt-qtz-hem-ep-hbl-d-ab	lower amphibolite	basalt
	JN2158B			Nourse&Stewart		Grayschist	graphite-qtz-bio-calc-ep-musc-ab	lowermost amphibolite	pelitic graywacke
	JN2160			Nourse&Stewart		Talc Schist	sph-calcite-act-musc-ep-talc-ab		ultramafic?
	JN2159			Nourse&Stewart		Spotted Mafic Schist	hem-calcite-ep-hbl-d-ab	lower amphibolite	basalt
	JN2157A			Nourse&Stewart		Greenschist	bio-sph-gt-chl-ep-act-ab	lowermost amphibolite	basalt
	JN2157B			Nourse&Stewart		Greenschist	sph-bio-gt-chl-ep-act-ab	lowermost amphibolite	basalt
	JN2156			Nourse&Stewart		Grayschist	graphite-bio-chl-musc-qtz-ab	lowermost amphibolite	basalt
JN2155			Nourse&Stewart		Greenschist	gt-qtz-sph-ep-act-ab	lowermost amphibolite	basalt	
Miscellaneous Blue Ridge Thin Sections	JNBR5/13#4			Nourse		Greenish Grayschist	muc-chl-ep-qtz-ab	uppermost greenschist	pelitic graywacke
	OW#6			Oliver Wolfe	spring 2014	Calcsillate Gneiss	di-calcite-qtz	lower amphibolite	carbonate w/chert
	OW#104			Oliver Wolfe	spring 2014	Banded Greenschist	chl-hbl-d-act-ep-ab layers alternate w/ musc-chl-qtz-ab	uppermost greenschist	basalt / pelitic graywacke
	OW#122			Oliver Wolfe	spring 2014	Greenish Grayschist	act-musc-chl-qtz-ab	uppermost greenschist	pelitic graywacke
	OW#127			Oliver Wolfe	spring 2014	Calcsillate Gneiss	calcite-qtz ribbons	uppermost greenschist(?)	carbonate w/chert
	OW#143			Oliver Wolfe	spring 2014	Actinolite Schist	qtz-chl-actinolite	uppermost greenschist(?)	ultramafic?
	OW#203			Oliver Wolfe	spring 2014	Greenschist	chl-act-ep-ab	uppermost greenschist	basalt
OW#205			Oliver Wolfe	spring 2014	Calcsillate Gneiss	gt-di-ep-ab-qtz	lower amphibolite	dirty carbonate w/chert	
E. Fork Block	MB#2			Nourse	winter 2003	Greenschist	qtz-sph-ep-chl-actinolite-ab	upper greenschist	basalt
	MB#6			Nourse	winter 2003	Greenschist	qtz-sph-ep-chl-actinolite-ab	upper greenschist	basalt
	JNCM1945A&B			Nourse		Fine Grayschist	chl-bio-qtz-ab	uppermost greenschist	pelitic graywacke
	JN2161			Nourse&Stewart		Fine Grayschist	sph-ep-musc-qtz-ab	upper greenschist	pelitic graywacke
Sierra Pelona	BouqueCyn			Nourse&Jacobson		Grayschist	graphite-bio-ep-musc-qtz-ab	lowermost amphibolite	pelitic graywacke

Notes: ¹ Mineral ID by Jon Nourse; ² See Plate A for map locations; Samples listed from shallow to deep structural level within a given sub-area; ³ UTM datum = NAD27 ConUS; ⁴ Mineral assemblages listed in order of increasing relative abundance; Mineral abbreviations: gt=garnet, chl=chlorite, musc=muscovite, bio=biotite, act=actinolite, hbl=hornblende, sph=sphene, di=diopside, calcite=calcite or dolomite, ab=albite, qtz=quartz; mgt=magnetite(?), hem=hematite(?), and=andalusite (or other aluminosilicate?); ⁵ Metamorphic grade and inferred protolith follow pages 384-85 and Tables 19-1 and 20-1 of Williams, Turner, and Gilbert (1972)

Structure

Syn-metamorphic and Post-metamorphic Folds

The Pelona schist of Blue Ridge is characterized by complex folding at various scales, geometries, and orientations. As shown on Plate 1, abundant folds are distinguished at map scale by dip reversals in foliation. Additional folds at outcrop scale are manifested as asymmetric “S” and “Z” folds associated with systematic shearing, and symmetric isoclinal folds probably related to flattening or pure shear. Interpretation is complicated by the fact that two or more trends of fold hinges exist, implying different compression directions. Another challenge is sorting out which folds developed during metamorphism (presumably during Late Cretaceous-early Tertiary subduction of the schist protoliths) as opposed to folds with larger wavelengths that likely formed after metamorphism.

Map-scale Folds

Map-scale folds are numerous in the study area and are identified by mapped foliation patterns. Stereonet solutions for best-fit cylindrical fold axes and corresponding axial planes were calculated for each fold group and placed on index maps for visual reference (Figures 26 - 28). The geographic distribution of folded foliation is shown by the same set of stereonet on Plate 1. Two groups of fold orientations exist: 1) west-northwest trending fold axes and 2) northerly trending fold axes (Figures 29 and 30). Axial planes of folds generally form perpendicular to principal stress orientations and can be used to determine the direction of shortening. Those folds with dipping axial planes are asymmetric and provide additional information about sense-of-shear that that may be associated with folding. This structural information can also be used to evaluate possible

local rotation due to transform boundary shearing and/or larger block rotations when averages of the axial planes are compared to local axial planes of a fold group.

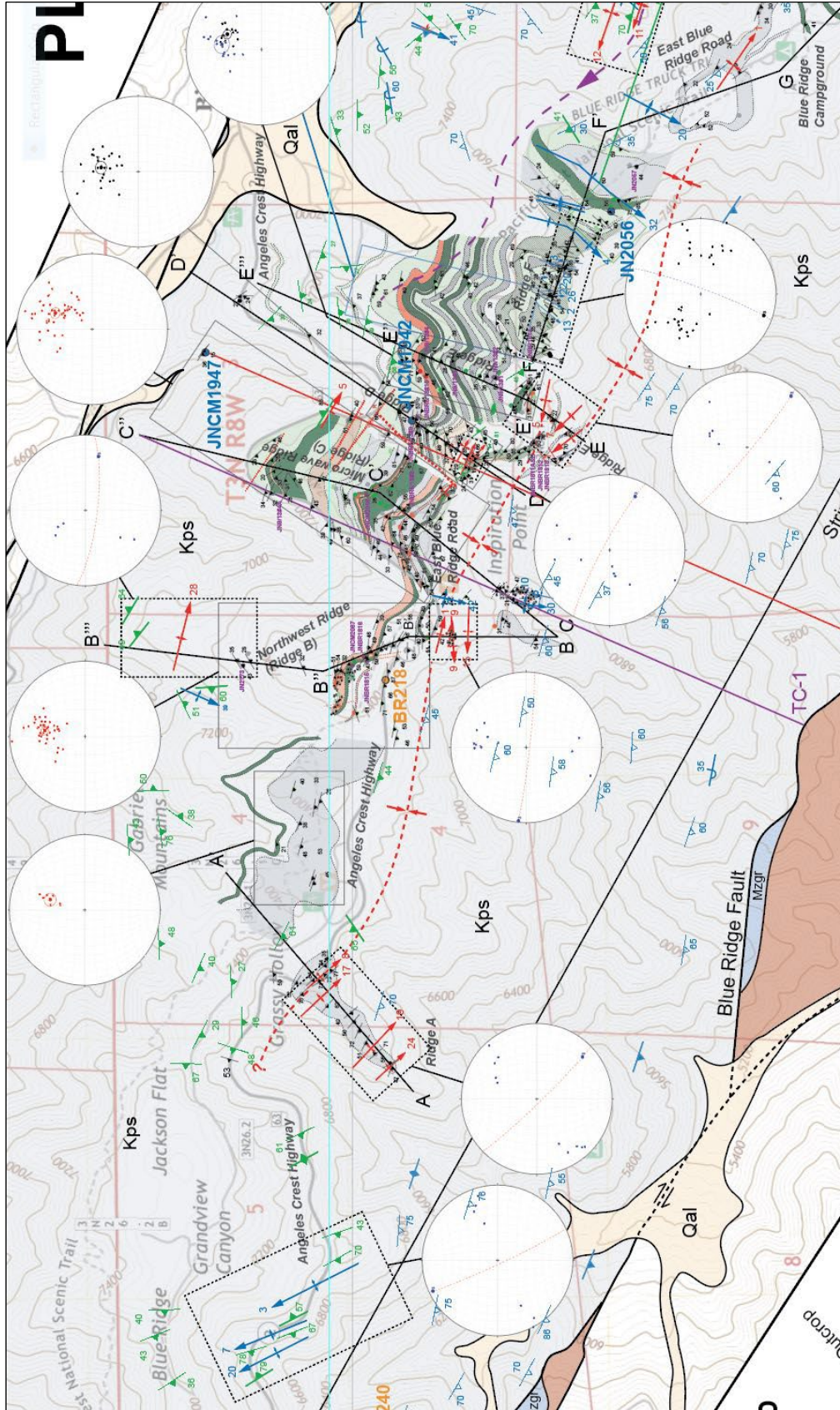


Figure 26. Map of subarea 1 showing distribution of map-scale folds and stereonet poles with average axial planes. Poles to foliations are shown. Also shown are stereonets with SW dipping foliation cross-section line.

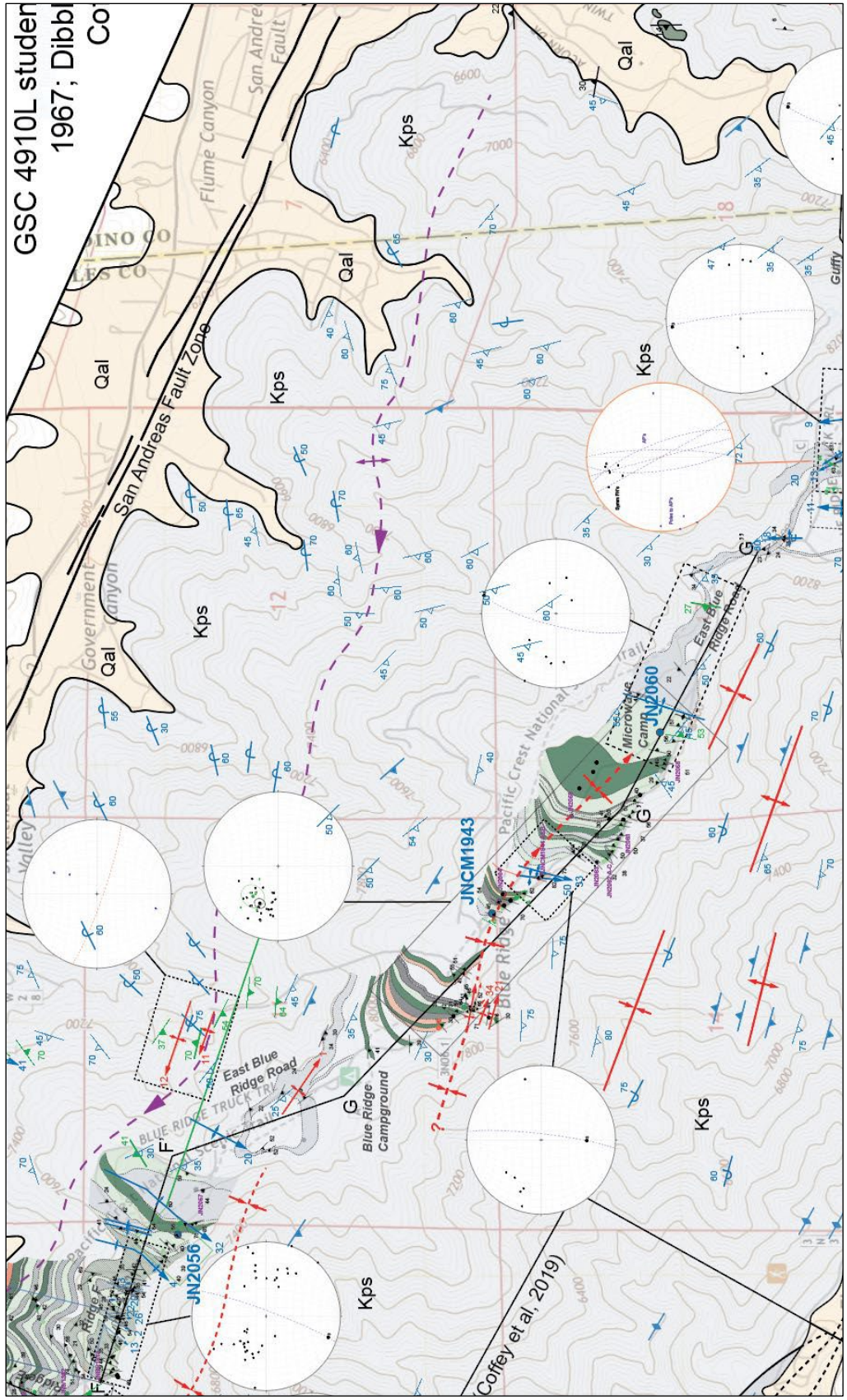


Figure 27. Subarea 2 map showing distribution of map-scale folds and stereonets with average axial planes. Poles to foliations are shown. Also shown are stereonets with SW dipping foliation poles for ridge cross-section line G.

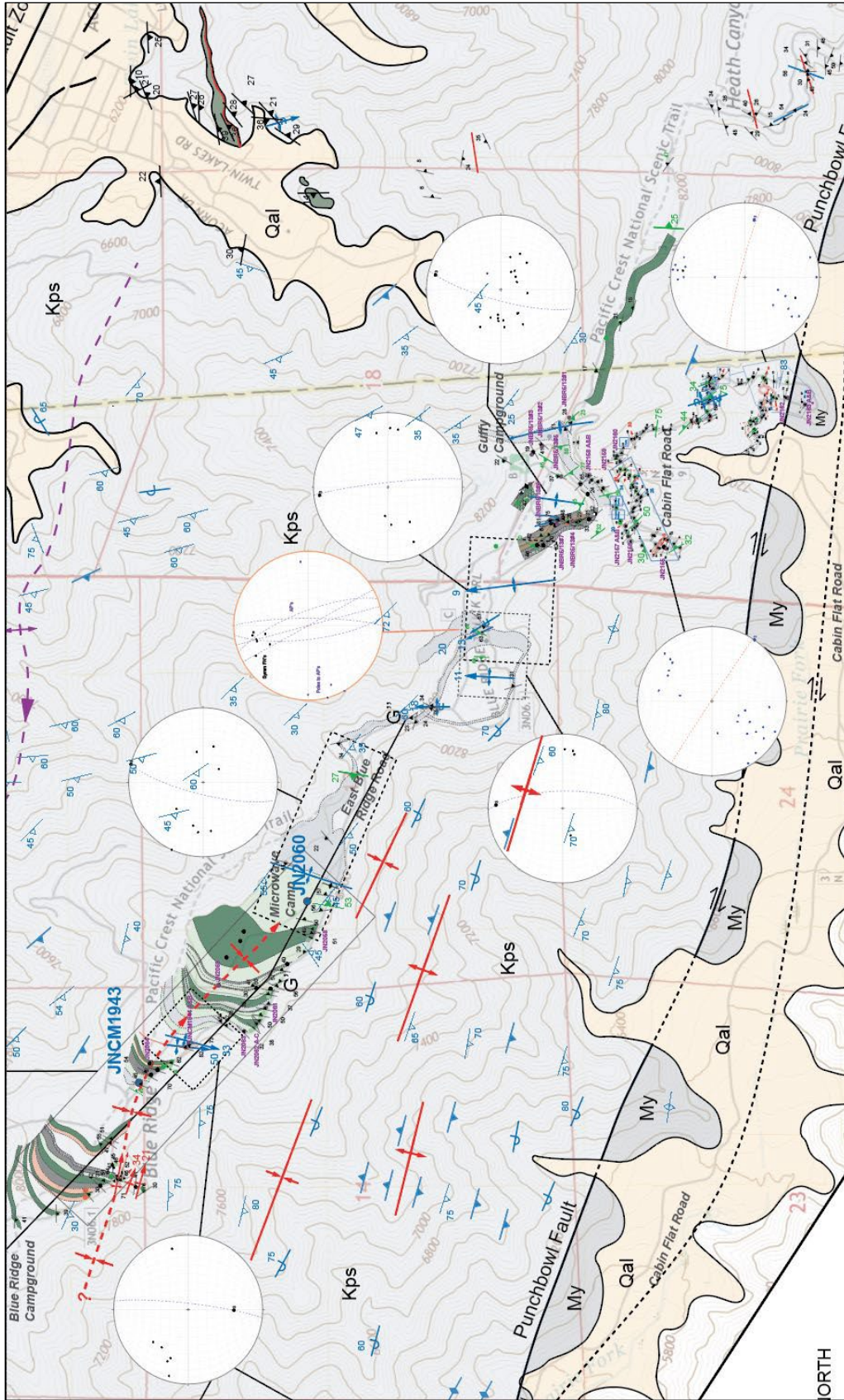


Figure 28. Subarea 3 map showing distribution of map-scale folds and stereonets with average axial planes. Poles to foliations are shown.

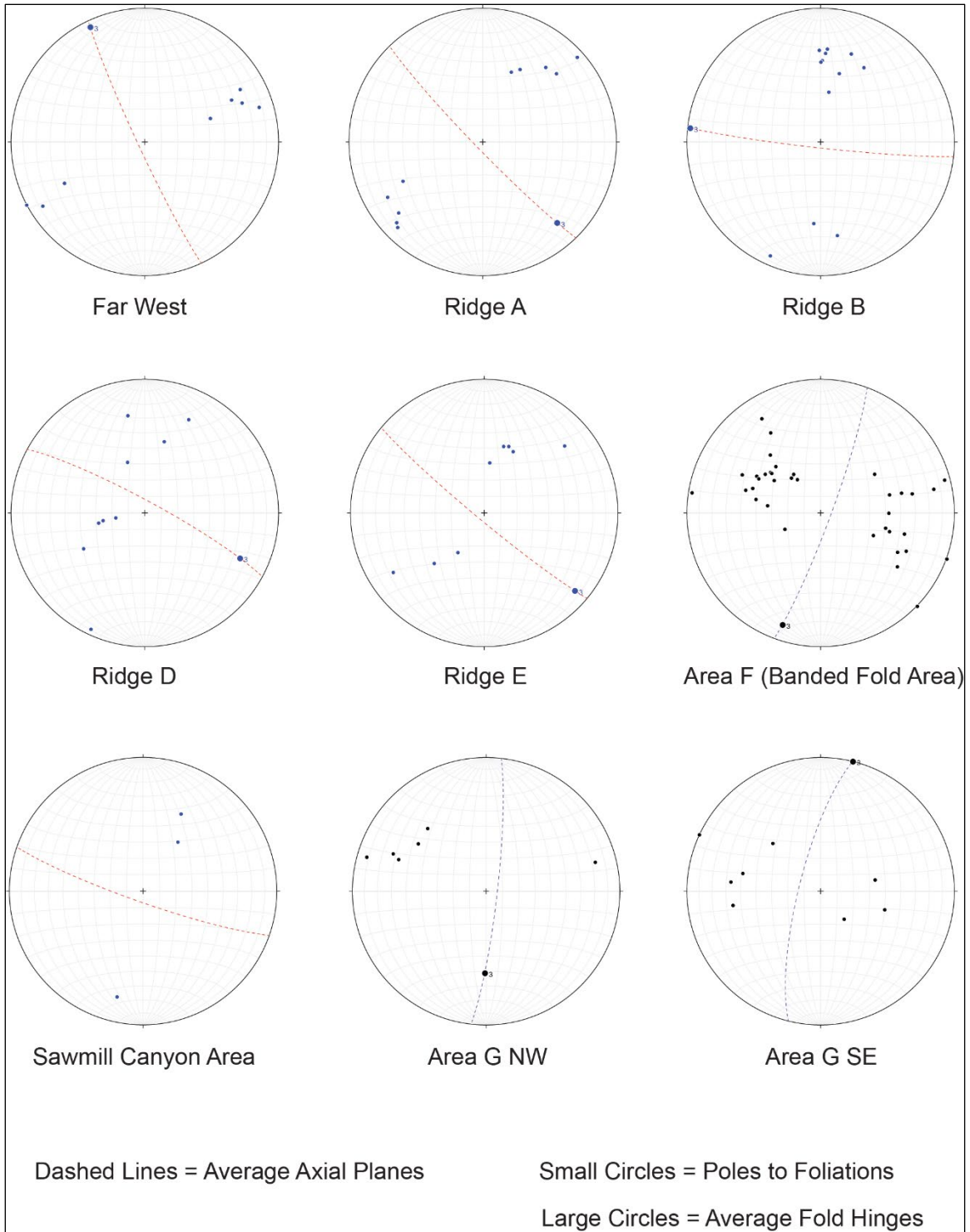


Figure 29. Stereonets of map-scale folds arranged from northwest to southeast locations (see index maps above for locations). The large black dots represent best-fit cylindrical fold axes calculated by the Stereonet program. Axial planes (shown in red and purple) simultaneously bisect the fold limbs and contain the fold axis.

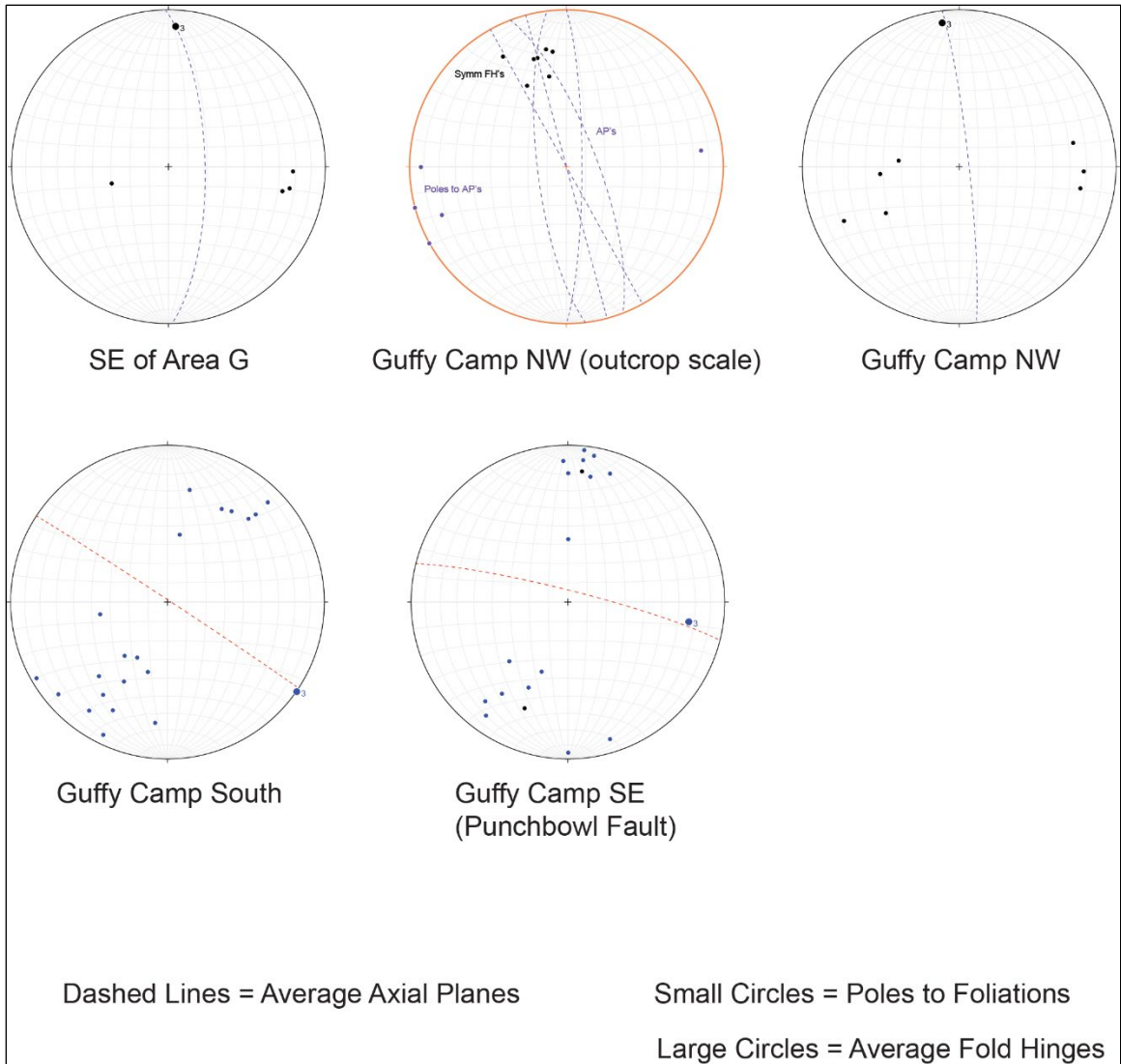


Figure 30. Stereonets of map-scale folds arranged from northwest to southeast locations (see index maps above for locations). The large black dots represent best-fit cylindrical fold axes calculated by the Stereonet program. Axial planes (shown in red and purple) simultaneously bisect the fold limbs and contain the fold axis. Stereonet with orange border is outcrop scale.

Figure 31 shows all poles to foliations and the average axial plane for the NE trending fold group. The pole to the axial plane indicates the direction of maximum principal stress is N72W-S72E and the average interlimb angle of the fold group is 100 degrees.

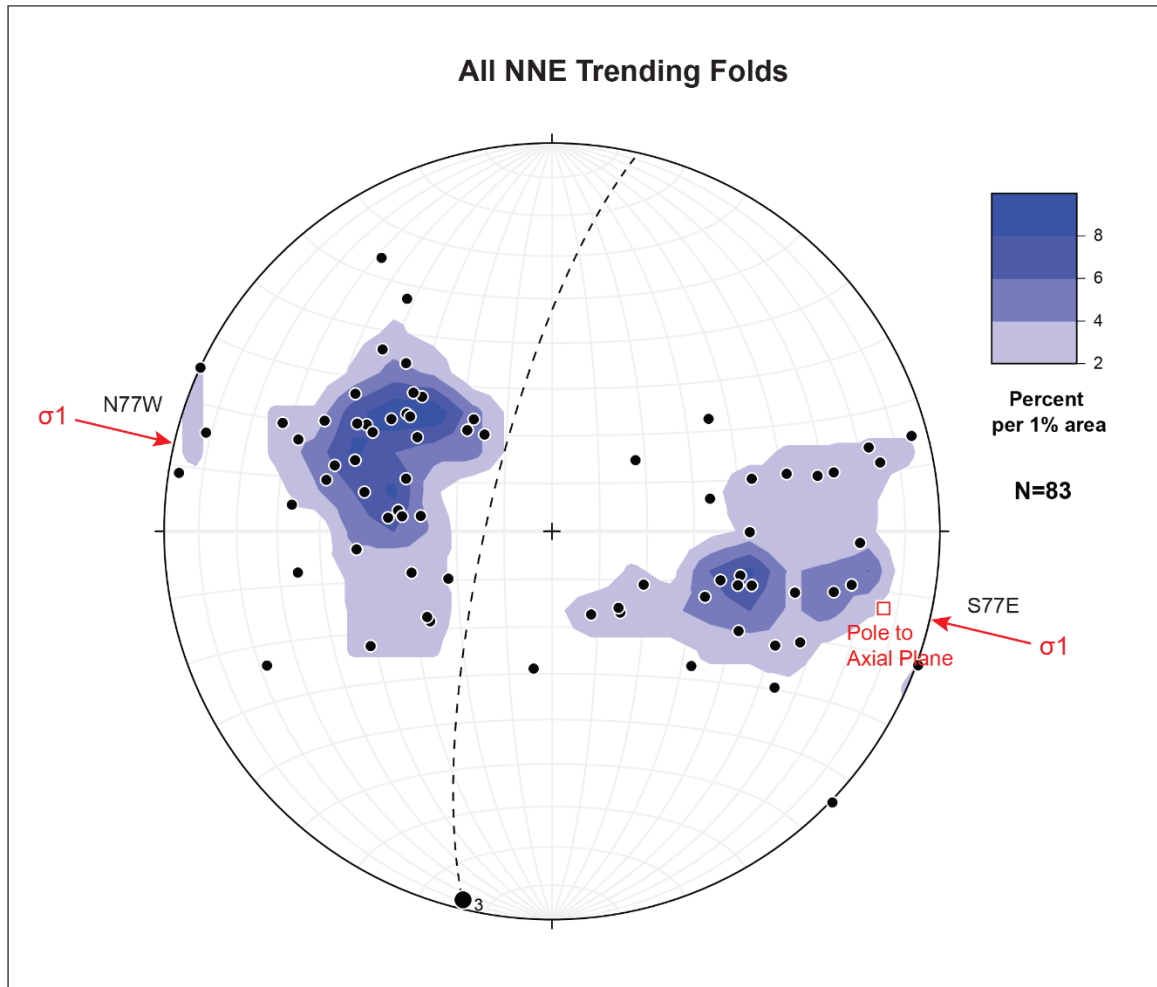


Figure 31. Stereonet showing all NE trending folds defined by foliation poles. The calculated average axial plane for the fold group is shown.

Figure 32 shows all poles to foliations and the average axial plane for the west-northwest trending fold group. The pole to the axial plane indicates the direction of maximum principal stress is N29E-S29W. The wide scatter pattern indicates that the folds have been disrupted by a later folding event, local faulting, or local block rotation.

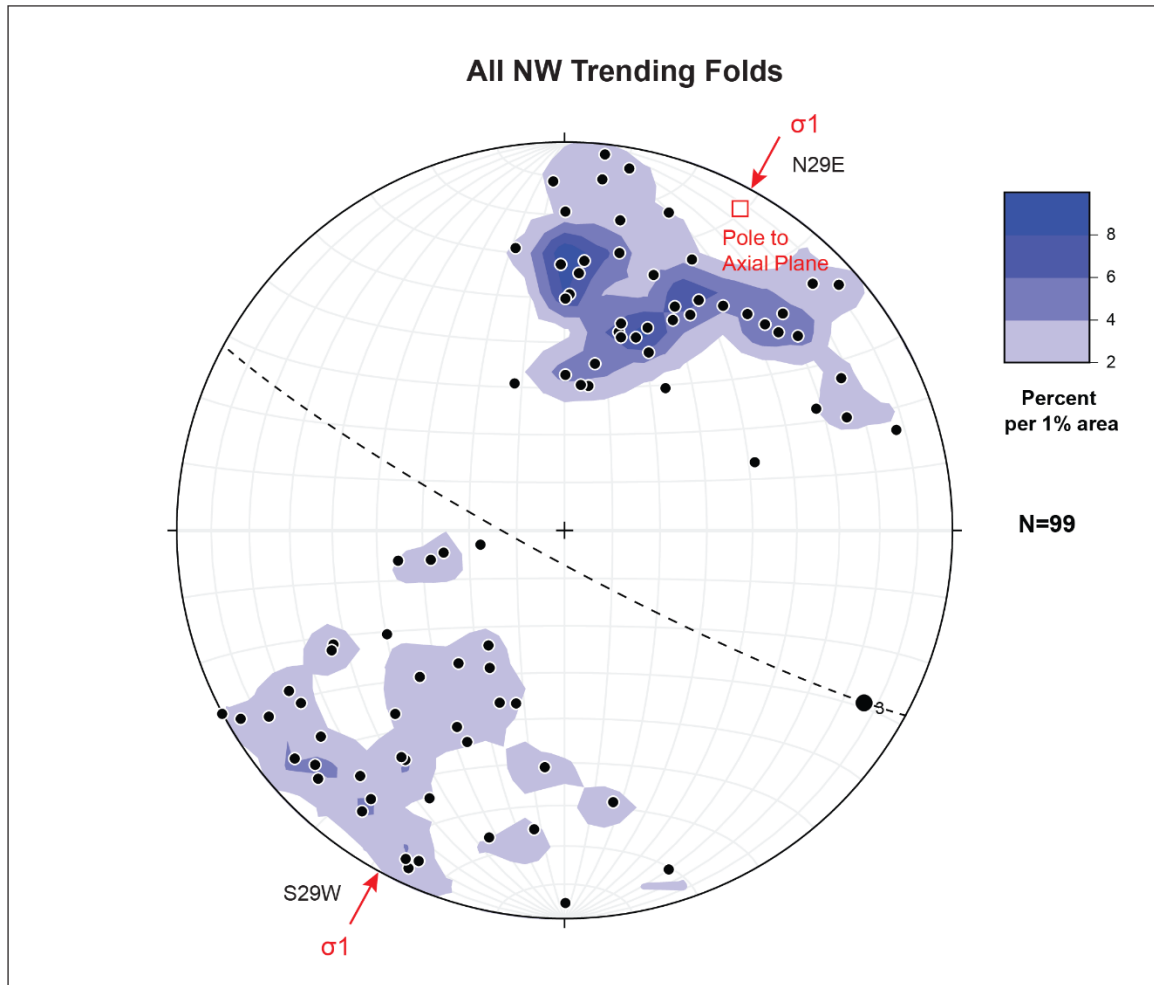


Figure 32. Stereonet showing all WNW trending folds defined by foliation poles. The calculated average axial plane for the fold group is shown.

Outcrop-scale Folds – S, Z, and Symmetric Isoclinal Folds

Outcrop scale folds in the study area are represented by symmetric and asymmetric folds. Axial planes are generally sub-parallel to local foliation and symmetric folds are isoclinal, indicating that significant flattening of the schist has occurred. Asymmetric folds (S and Z folds) may indicate regional shearing direction, or local flexural slip within opposite limbs of larger folds (also known as parasitic folding). Regional shearing produces asymmetric folds when, in this case, the upper plate of a

subduction zone (North American plate) exerts traction on the subducting plate (Pelona schist) causing shearing to occur in both plates. This shearing rotates pre-existing folds antithetic to the movement direction of the lower plate (Pelona schist) and should be pervasive within the schist body near the plate boundaries. In theory this sounds straightforward, but within the study area there are abundant domains of symmetric isoclinal folds that likely record flattening strain driven by tectonic loading. Parasitic folds form when pre-existing folds within a layer are rotated clockwise or counterclockwise as layers bounding the folds experience flexural slip during a secondary megascopic folding phase. Differentiating between the two types requires performing fold tests. In this section, results are presented on fold tests performed on several areas where asymmetric folds were measured.

Ridge B (Northwest Ridge)

In the area of Ridge B (cross-section B), thirteen asymmetric S and Z folds were measured in calc-silicate layers (Figure 33). Three of the folds are characterized as S folds and ten are characterized as Z folds (as viewed down the plunge of the fold hinges). Fold hinges are tightly grouped with south or southeast trends and moderate to shallow plunges. Gross foliation is dipping approximately thirty-five degrees to the south and axial planes of the S and Z folds have strikes subparallel to the foliation with slightly steeper dips (Figure 33A). Because the axial planes are sub-parallel to foliation and do not conform to other axial plane orientations in the area belonging to map scale folds, these asymmetric folds are interpreted to have been formed during regional shearing and are therefore “syn-metamorphic”. Measured orientation data was unfolded about local foliation to evaluate shearing direction (Figure 33B). The ten measured Z folds

demonstrate top to west-southwest vergence as viewed down plunge in outcrop and imply a motion direction of east-northeast for the subducting plate relative to North America. However, the S folds show top to east-northeast vergence implying a motion direction of west-southwest for the subducting plate and are problematic in this interpretation. The convergence vector of the Farallon plate with the North American plate is widely accepted to be roughly northeast but this is not the only regional shearing event to have affected the schist body. Exhumation processes may have involved channelized extrusion (Chapman, 2016) which would be opposite the subduction direction. Another interpretation of the data is that a second oblique shearing event can make Z folds appear to be S folds.

Regardless of the antithetic shearing of the S folds, the dominant shearing direction shown by the Z folds is examined here. The direction of lower plate motion is orthogonal to the mean fold hinge and is oriented at N78.5E. To account for the Big Bend deflection in the trace of the San Andreas fault, the plate motion direction is rotated clockwise by 17 degrees yielding a motion direction of S84.5E (Figure 33C). If the shearing data is correctly interpreted to be regional, this implies that the Blue Ridge block has undergone clockwise rotation of approximately 40 degrees since exhumation if the convergence vector of the Farallon plate is assumed to be approximately N45E. Evidence for the convergence vector will be explored in the Discussion section.

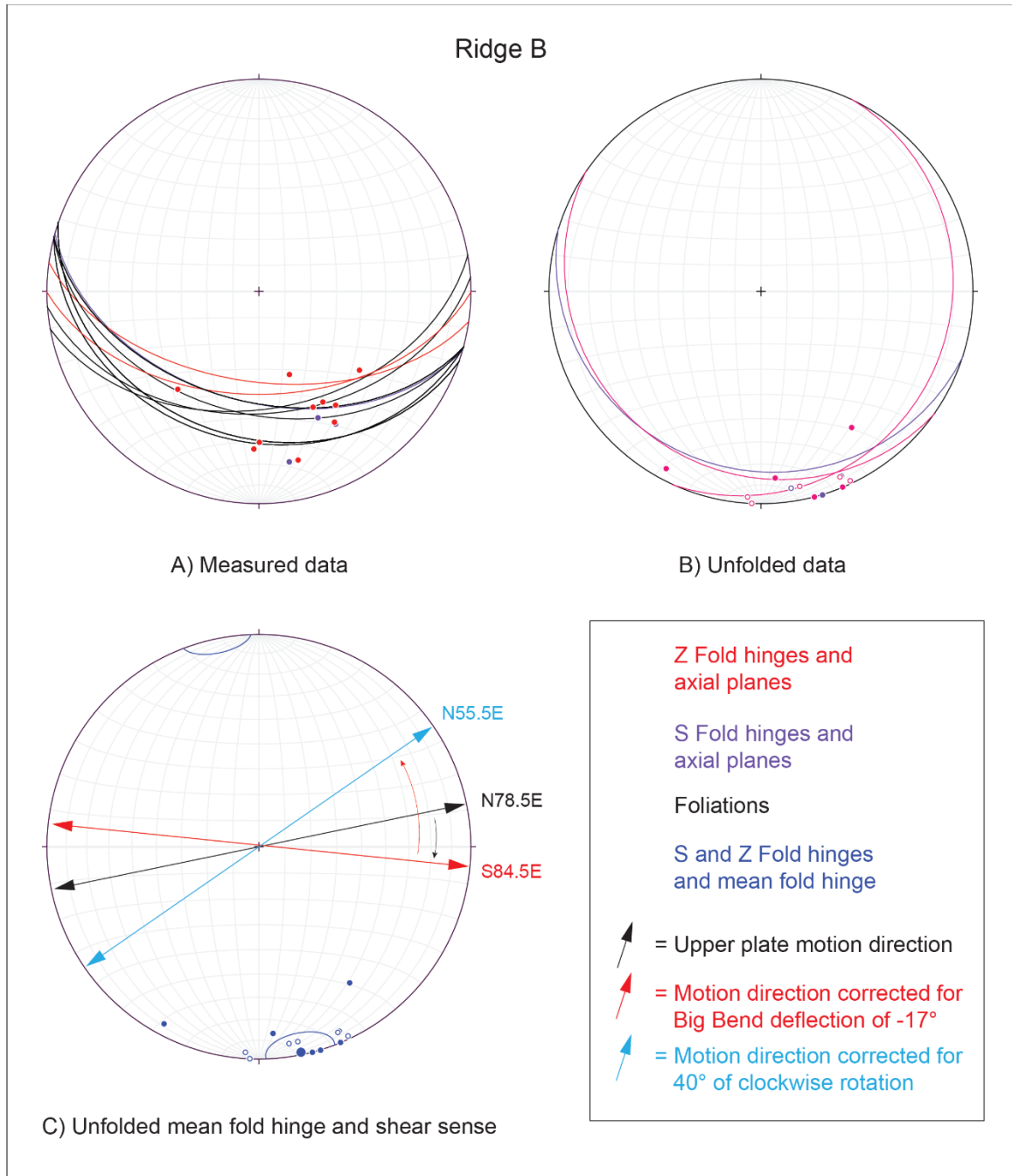


Figure 33. Stereonet plots showing A) Measured fold hinges of S and Z folds and axial planes at location Ridge B and local foliations; B) Unfolded measurements about local foliation; and C) unfolded mean fold hinge with derived plate motion direction (black) and plate motion direction corrected for “big bend” deflection (red). Blue arrow indicates upper plate motion resulting from implied backrotation of 40 degrees.

Banded Fold Area (Cross-section F)

The area defined by cross-section F is characterized by gray schist with darker compositional layering (possibly amphibole?) which gives the schist outcrop a banded appearance and hosts abundant asymmetric folds. Seven Z fold hinges and 11 S fold hinges were measured from opposite limbs of a map-scale synform. In this area, several map-scale folds with north-northeast trending hinges exist. When S and Z folds are plotted along with the respective axial planes, they show a syncline pattern consistent with flexural slip S folds on the left and Z folds on the right limbs of the map scale fold (Figure 34A). Figure 34B shows the average axial plane and poles to foliations that define map-scale folds in this area. Fold hinges have generally shallow plunges. This is one of the best examples of flexural slip encountered in the study area. Together, the map scale and outcrop scale folds document syn-metamorphic structures associated with WNW-ESE directed Laramide shortening.

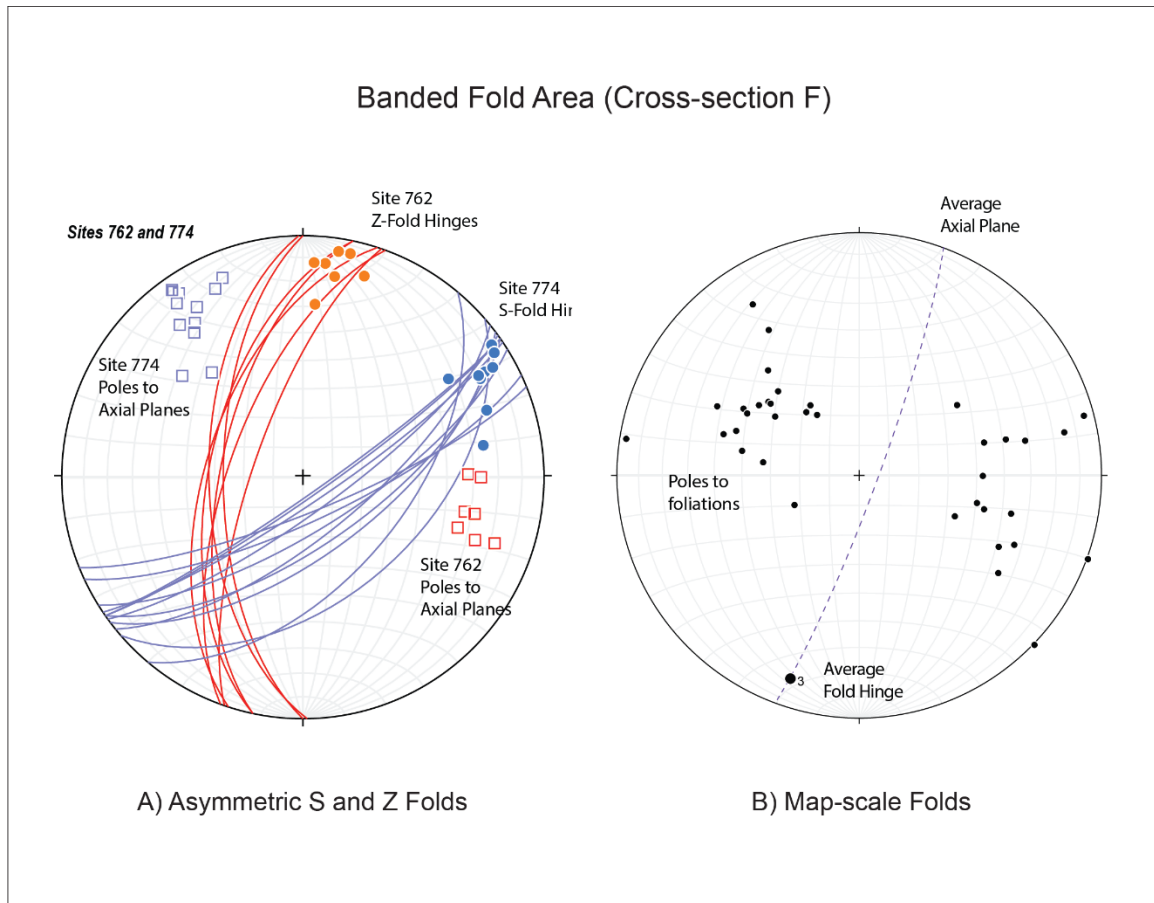


Figure 34. Stereonet plots of asymmetric flexural slip folds (A) on Map-scale folds (B).

Ridge E Syncline

In the area of Ridge E, exposures of calc-silicate occur on the north and south limbs of an east/west trending map-scale syncline that show many well-developed S and Z folds. Two Z folds were measured on the north limb and seven S folds on the south limb. Again, S and Z folds were recorded/described as viewed down the plunge of the fold hinges. S and Z fold axial planes have strikes subparallel to the local foliations but dip slightly steeper, as in the case of Ridge B described above (Figure 35A). When fold hinges and axial planes for each limb are unfolded about local foliation, a similar pattern

to that of Ridge B is shown with the exception that no ambiguous data is shown for vergence direction (Figure 35B). Here, both the S and Z folds show top to west-southwest vergence as viewed down plunge in outcrop. This implies a top to east-northeast motion direction for the subducting plate relative to North America. The average fold hinge for the S folds shows a lower plate motion direction of N77.4E for this area of the schist. Correction for the SAF Big Bend rotation yields a plate motion direction of S85.6E (Figure 35C). Strikingly, the Ridge B folds show a nearly identical plate motion direction as Ridge E, although the Ridge B data is somewhat bi-directional. It should be noted that the S fold data set was used to calculate the vergence direction for the Ridge E syncline since the Z fold data set is comprised only of two measurements with the same trend and plunge. The vergence direction for the Z folds would show a plate motion direction of S88E (uncorrected) and S71E (corrected), which is consistent with the general vergence direction of the S fold data set but is likely not representative of what the average Z fold vergence would be due to the low number of measurements.

This site is especially significant to interpretation of the tectonic history because the data show that the S and Z folds were not caused by flexural slip during map scale folding of the calcisilicate horizon. Instead, the west-vergence documented by fold asymmetries on both limbs of the synform represents an early shearing event (probably associated with Laramide subduction of the schist). Creation of the map scale synform occurred later, as clearly documented by this “fold test.” Furthermore, the compression direction related to the later folding event is markedly different, approximately N45E. Also, as in the case of Ridge B, the data from Ridge E implies that the Blue Ridge block has undergone clockwise rotation of approximately 40 degrees since exhumation.

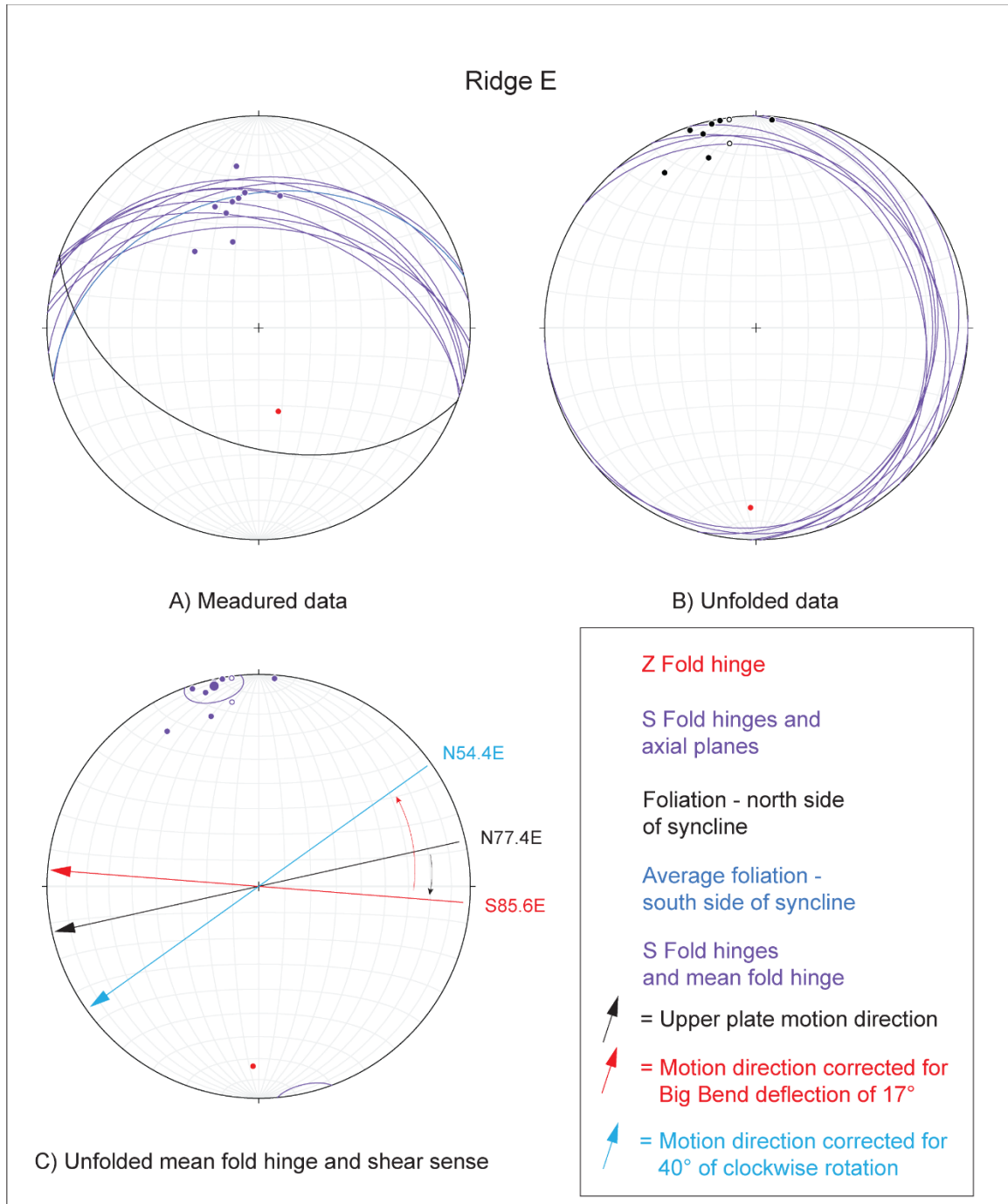


Figure 35. Stereonet plots of asymmetric folds on north and south side of map-scale syncline. A) Measured fold hinges of S and Z folds and axial planes at location Ridge E and local foliations; B) Unfolded measurements about local foliation; and C) unfolded mean fold hinge with derived plate motion direction (black) and plate motion direction corrected for “big bend” deflection (red). Blue arrow indicates upper plate motion resulting from implied backrotation of 40 degrees.

Faults

Faults within the Blue Ridge schist are not exposed in abundance. However, numerous small slicken-side exposures exist in accessible outcrops and road cuts. Due to time constraints, a sample area was studied which focused on ridges C and D (cross-sections C and D). Additionally, mapping conducted by Dr. Nourse and his mapping class located several faults in the area south of Guffy Camp.

Ridges C and D

At the toe of Ridge D (cross-section D) in the Hwy 2 road cut are several faults exposed in gray schist which are parallel to each other and separated by a couple of meters. Fault gouge, approximately 5 cm thick, is associated with the exposed fault planes as well as some striated surfaces. Because this is a road cut and the faults are viewed into the fault plane, the total thickness of the gouge zone is unknown since much of it may have been removed during road construction. The fault planes are oriented at 10 degrees clockwise to the San Andreas fault zone and show right lateral sense of movement, indicating that they are Reidel shears, synthetic to the SAF which has a strike of N60-65W in this area.

Similarly, a fault is located at the toe of ridge C in the Hwy 2 road cut. This fault is characterized by a white gouge zone approximately 0.5-0.75 m thick within reddish-brown weathered mafic schist (Figure 36B). Orientation of the fault plane is parallel to the SAF and is interpreted as a Y shear plane synthetic to the SAF.

Numerous slicken-sides occur on outcrops of gray and mafic schist along a dirt road paralleling ridge D, bordering the area in which the hypothesized fault is located to the west (Figure 36A).

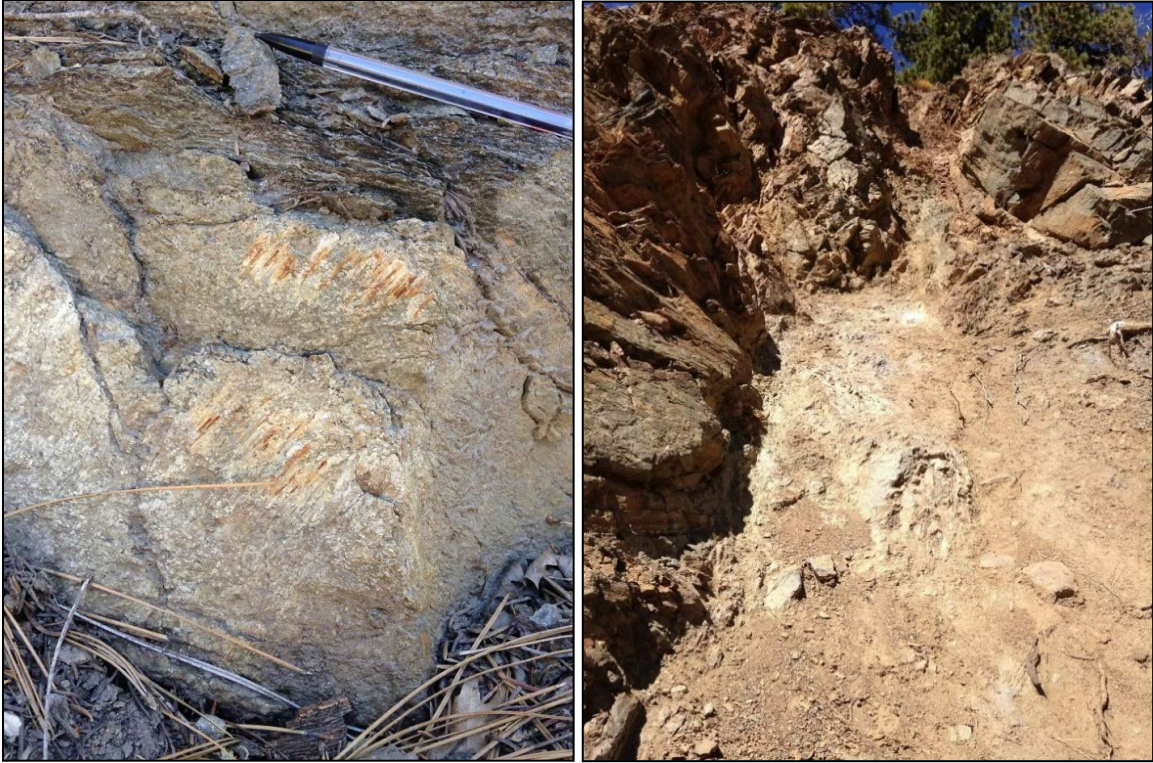


Figure 36. A) Left – Slickenside with down to the left motion. B) Right – Fault gouge in roadcut on Hwy 2. Fault plane is oriented parallel with SAF and is probably a Y-shear.

U-Pb Geochronology

Five samples of chl-musc-quartzofeldspathic grayschist (metasandstone) were collected from different structural levels of the Blue Ridge Pelona schist along two stratigraphic sections to assess detrital zircon provenance and maximum depositional age (MDA). One additional sample of metasandstone was taken from Lupine Camp, south of the Punchbowl fault in the East Fork block. The resulting U-Pb zircon results are presented below in the form of concordia diagrams and probability density age plots. The complete data sets containing spot numbers, U-th concentrations, isotopic ratios, calculated ages, and discordance values are tabulated in Appendix C.

Section 1 is a composite section from three ridges represented by cross-sections B, C, and D (Figures 19, 20, 21) and contains samples JNCM1947 and JNCM1942, located in stratigraphic sequence from deep to shallow levels. Included in the upper part of this section is the previously published detrital zircon sample BR218 (Grove et al. 2003; Jacobson et al., 2011). This sample was taken along Angeles Crest Highway just north of Inspiration Point. It outcrops at a higher structural level than JNCM1942 and is also a quartzo-felspathic greyschist (Figure 19).

Section 2 is an apparently coherent stratigraphic section represented by cross-section FG'' (Figure 37). Subsection F-G'' has relatively few folds and contains samples JN2056, JNCM1943, and JN2060, also located in sequence, from deep to shallow levels. The structural thicknesses determined from balanced cross-section FG'' are approximately 724 m (2,375 ft) from sample JN2056 at the base of the section to JNCM1943, and 650 m (2,132 ft) from sample JNCM1943 to sample JN2060 at the top of the section. Total structural thickness for the dated interval is 1,374 m (4,507 ft). The original stratigraphic thickness was probably much more, given that these are metamorphic rocks that record significant flattening strain.

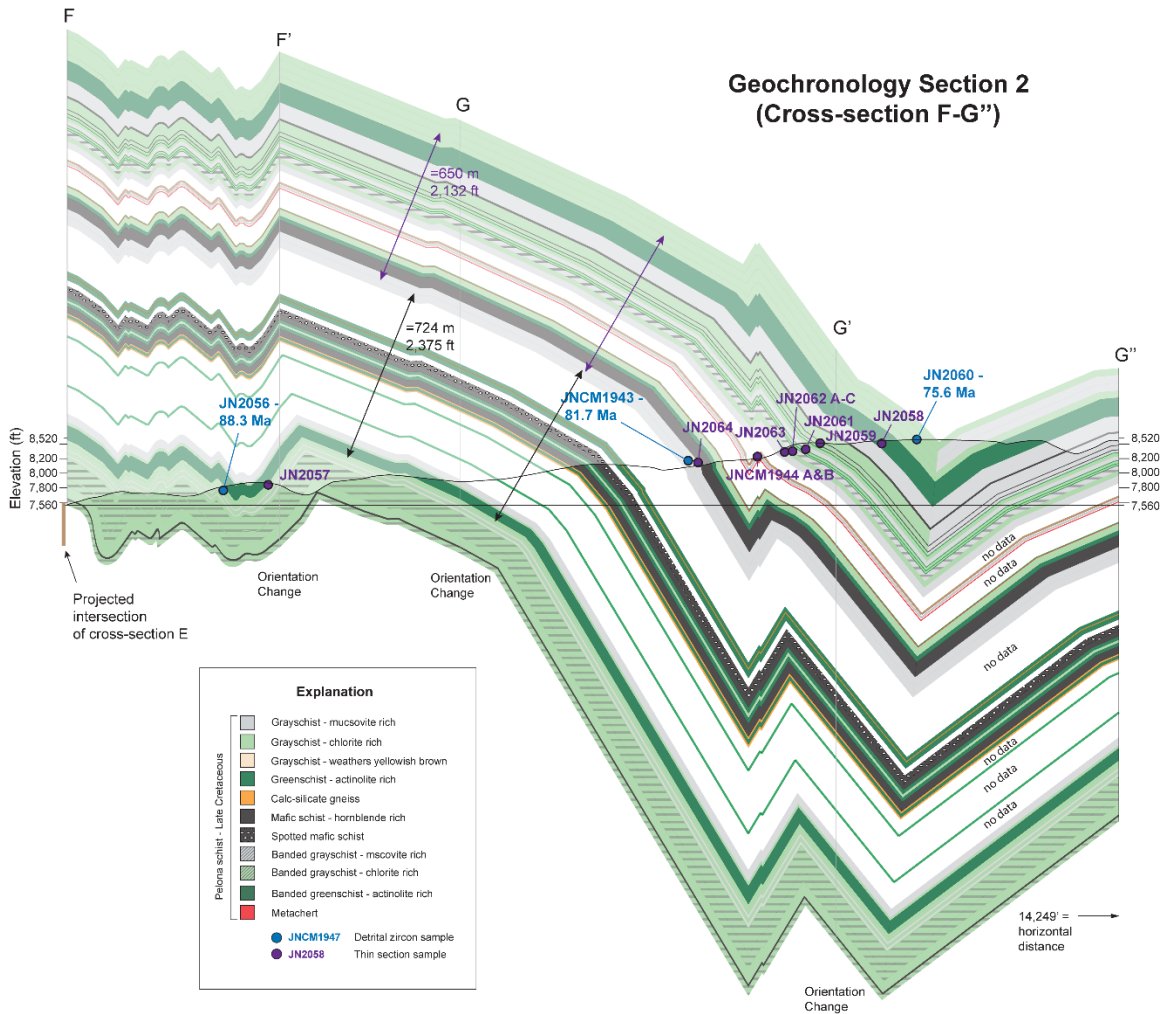


Figure 37. Cross-section F-G'' comprising Geochronology Section 2 showing location of detrital zircon sample sites (blue) with YSG age and thin section sample sites (purple). Structural thickness intervals and corresponding values are shown between detrital zircon sample sites.

A sample from the East Fork block was also collected during this study for overall comparison to the Blue Ridge block. Sample JN2161, taken from a prominent outcrop directly south from the area near Lupine Camp is also a quartzofelspathic grayschist. The sample is finer grained than Blue Ridge samples, and the metamorphic mineral assemblage is lower grade.

Concordia Plots

Concordia plots for the U-Pb analyses were generated in Isoplot v. 4.5 (Ludwig, 2007) for all samples (Figures 38 - 49). Two plots are provided per sample: 1) All analyses shown, and 2) A version showing only Mesozoic analyses for clarification.

Below is a short summary of each sample plot.

Section 1 Samples (deep to shallow)

Sample JNCM1947 yielded 41 viable zircon analyses; 2 highly discordant grains are omitted from the plot: Three grains had Mesoproterozoic $^{207}\text{Pb}/^{206}\text{Pb}$ ages of 1082, 1332, and 1483 Ma. Of the remaining 38 analyses two yielded Jurassic $^{206}\text{Pb}/^{238}\text{U}$ ages, the rest were Cretaceous, with ages ranging from 87 to 144 Ma.

Sample JNCM1942 yielded 31 zircons; three highly discordant analyses are omitted from the plot. One of four Proterozoic grains has a concordant age of 1807 Ma: the other three record Cretaceous lead loss, with $^{207}\text{Pb}/^{206}\text{Pb}$ ages of 1578, 1712, and 1775 Ma. The remaining 24 analyses yielded Cretaceous $^{206}\text{Pb}/^{238}\text{U}$ ages between 82 and 120 Ma.

Section 2 Samples (deep to shallow)

Sample JN2056 yielded 21 viable zircons (one was apatite). Eighteen of these grains had Cretaceous $^{206}\text{Pb}/^{238}\text{U}$ ages ranging from 88 to 116 Ma. Of the remaining three grains, one had a near-concordant Proterozoic $^{207}\text{Pb}/^{206}\text{Pb}$ age of 2483 Ma. The other two yielded highly discordant $^{207}\text{Pb}/^{206}\text{Pb}$ ages of 1048 and 2335 Ma and are interpreted to have experienced Cretaceous lead loss.

Sample JNCM1943 yielded 40 analyses total: 37 Cretaceous grains and three Proterozoic grains.

Sample JN2060 yielded 87 total grains. Of the 87 grains, ten turned out to be apatite, and one had very large errors. The remaining 76 zircons yielded a more complex age distribution than any of the other Blue Ridge samples. Twelve Proterozoic grains preserve $^{207}\text{Pb}/^{206}\text{Pb}$ ages between 1043 and 1752 Ma. The rest of the analyses yielded mainly Cretaceous $^{206}\text{Pb}/^{238}\text{U}$ ages (56 grains), with 6 Jurassic and 2 Permian grains rounding out the population.

All samples from the Blue Ridge block are derived predominantly from Mesozoic source rocks with a small contribution of Proterozoic grains. In contrast, sample JN2161 from Lupine Camp of the East Fork block has a much higher Proterozoic component, consistent with previous studies by Jacobson et al. (2011). 44% of 85 analyses yielded Proterozoic $^{207}\text{Pb}/^{206}\text{Pb}$ ages between 1150 and 2560 Ma. 41 of the remaining 48 grains preserve a wide range of Cretaceous $^{206}\text{Pb}/^{238}\text{U}$ ages between 70 and 136 Ma. Five Jurassic, one Triassic, and one Permian analyses round out the age distribution. Sample JN2161 thus highlights the difference in source rock contribution between the East Fork and Blue Ridge blocks.

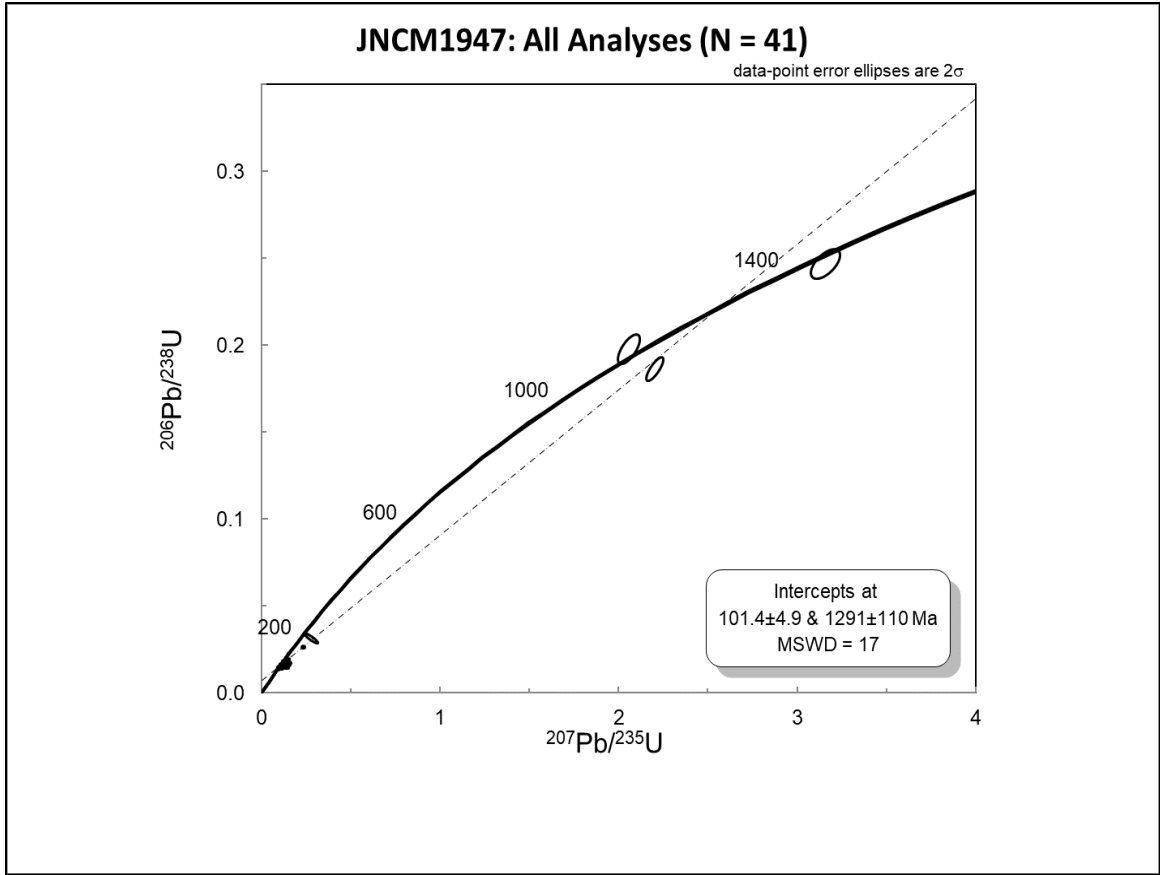


Figure 38. Concordia plot showing all analyses from JNCM1947 (Section 1).

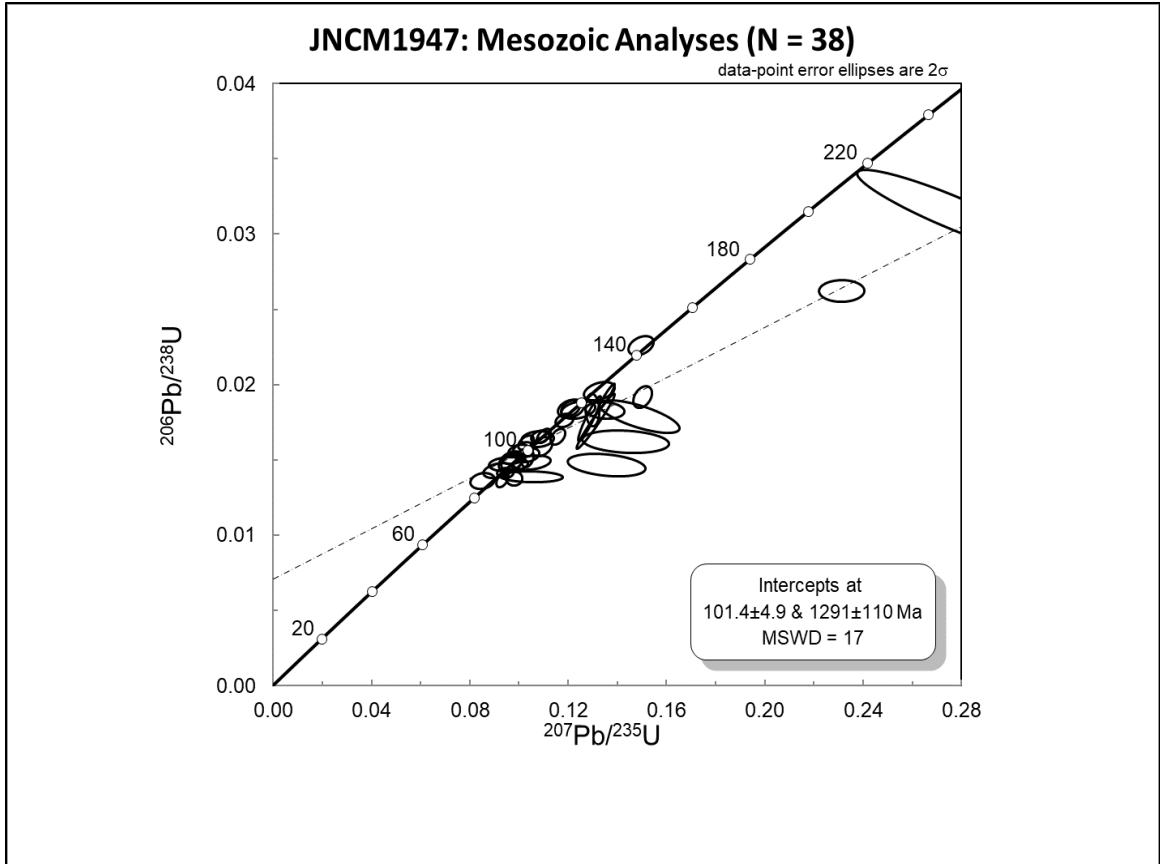


Figure 39. Concordia plot showing only Mesozoic analyses from JNCM1947 (Section 1).

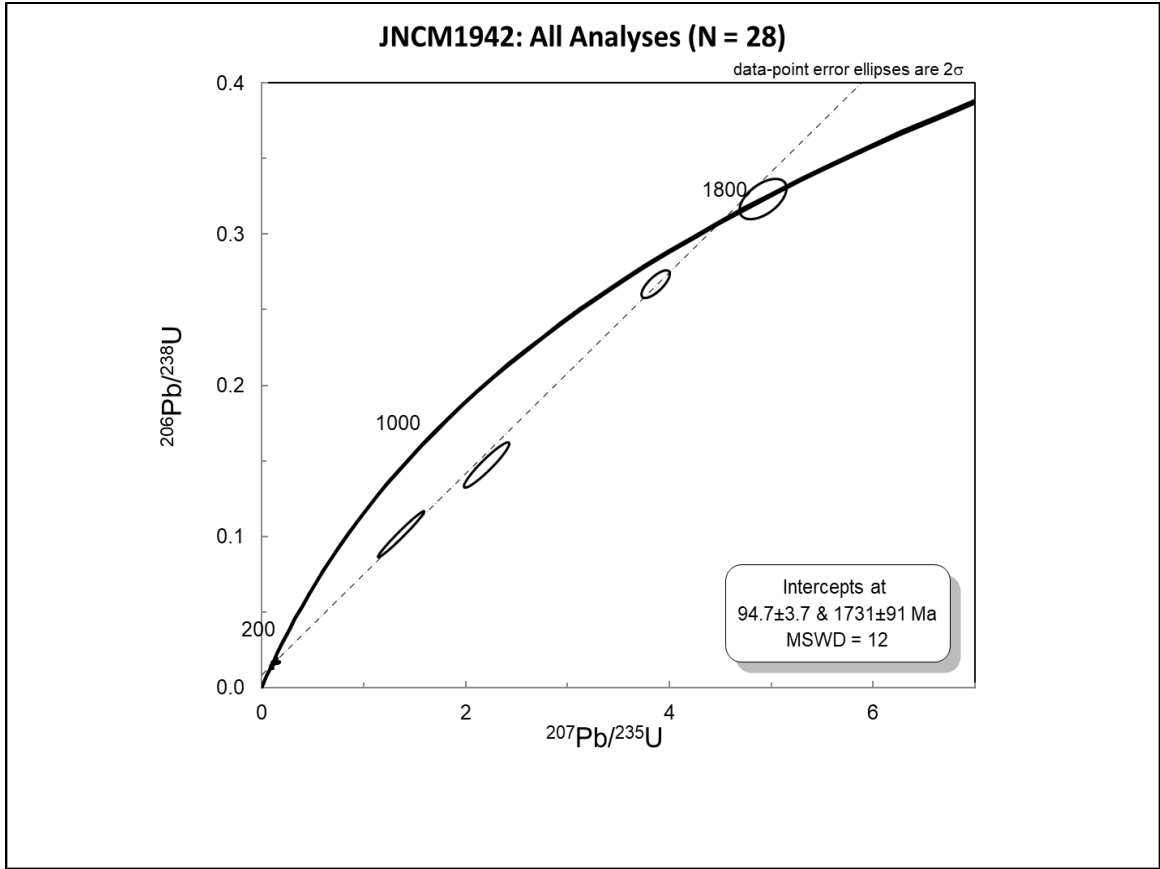


Figure 40. Concordia plot showing all analyses from JNCM1942 (Section 1).

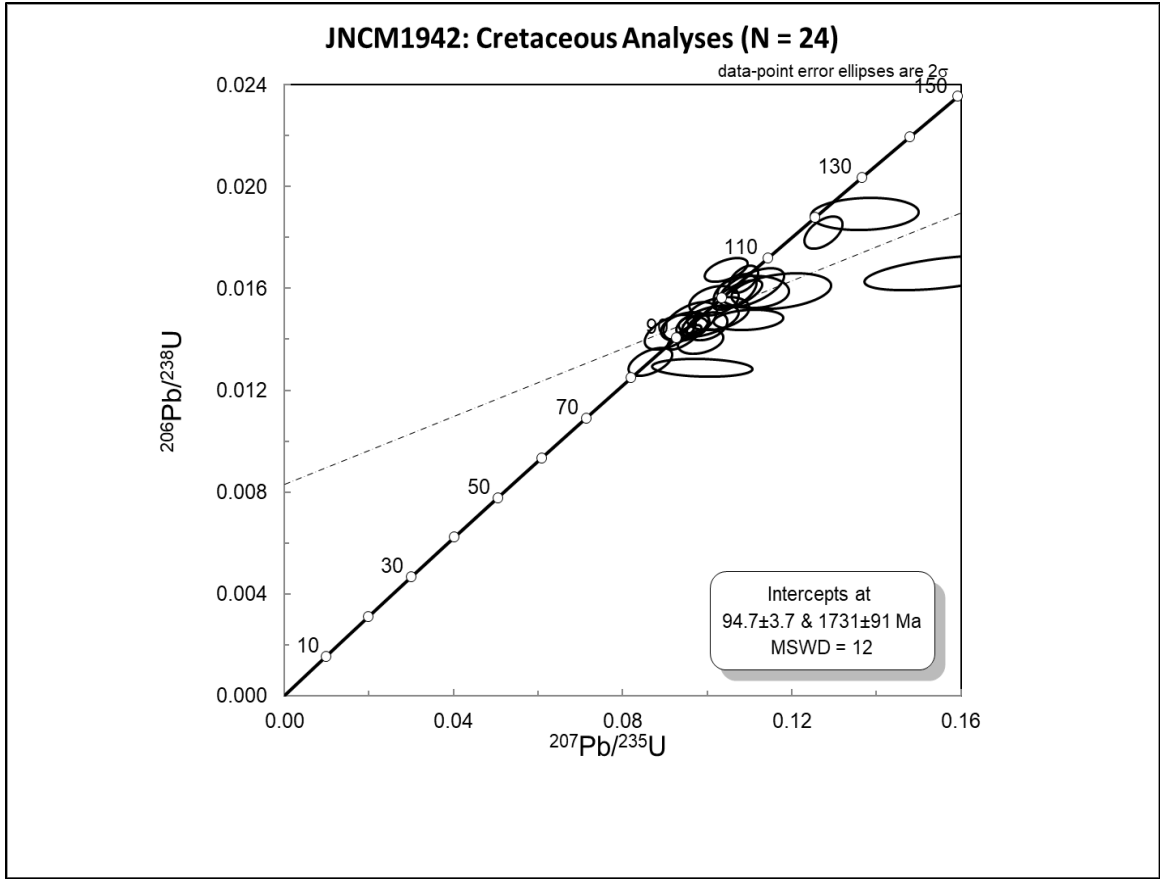


Figure 41. Concordia plot showing only Mesozoic analyses from JNCM1942 (Section 1).

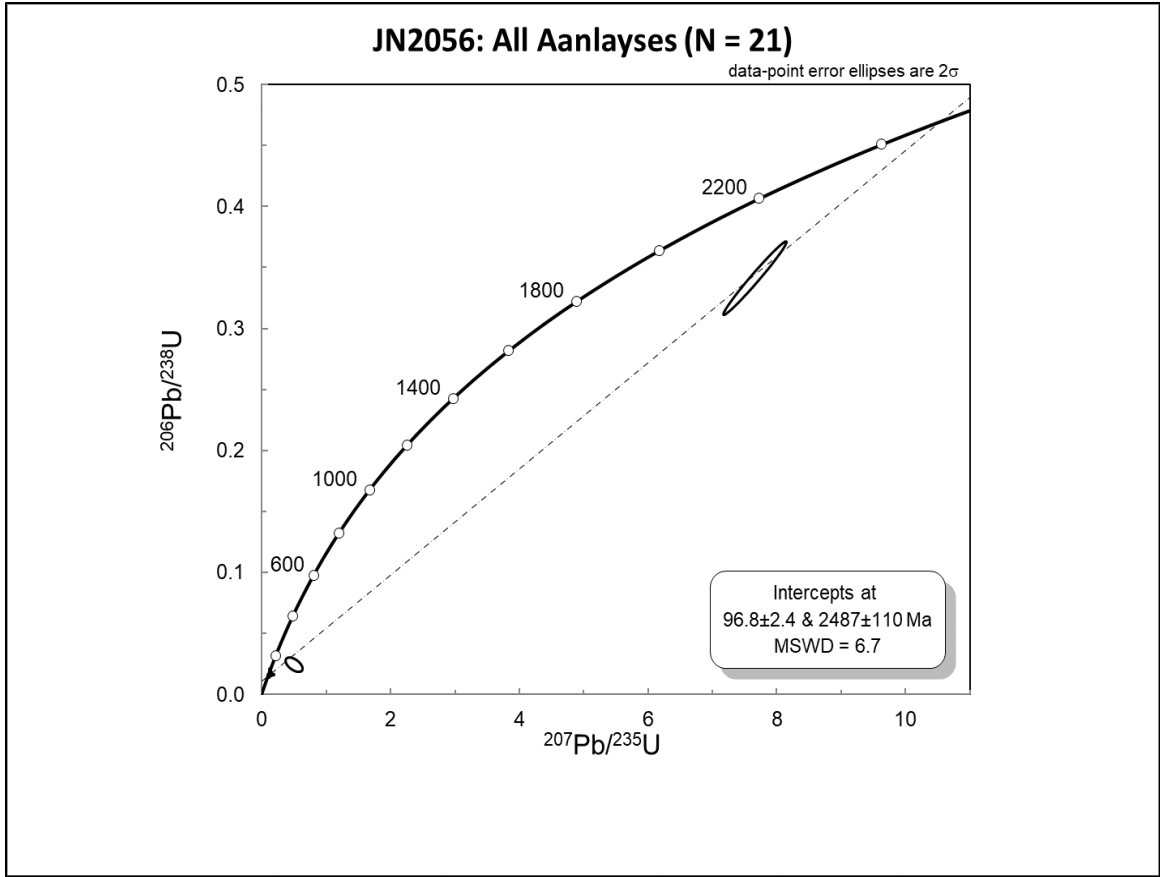


Figure 42. Concordia plot showing all analyses from JN2056 (Section 2).

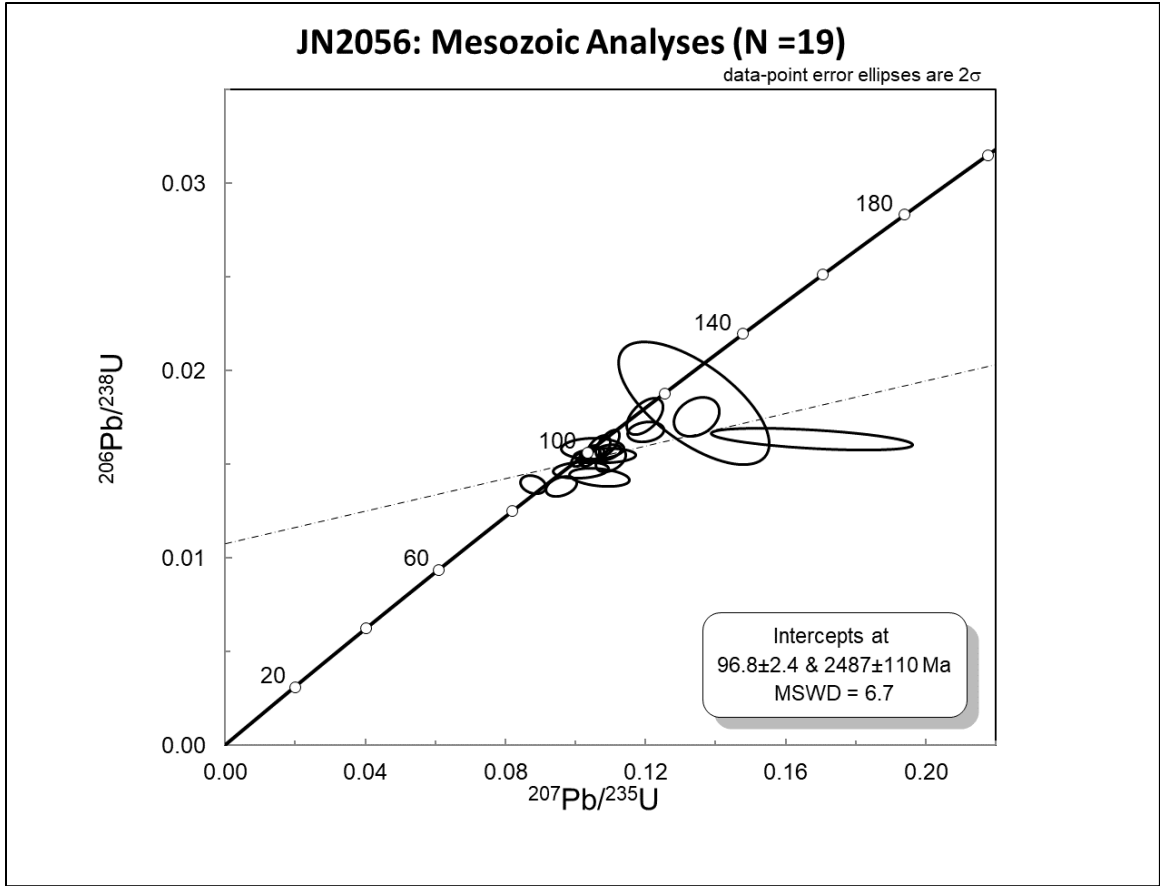


Figure 43. Concordia plot showing only Mesozoic analyses from JN2056 (Section 2).

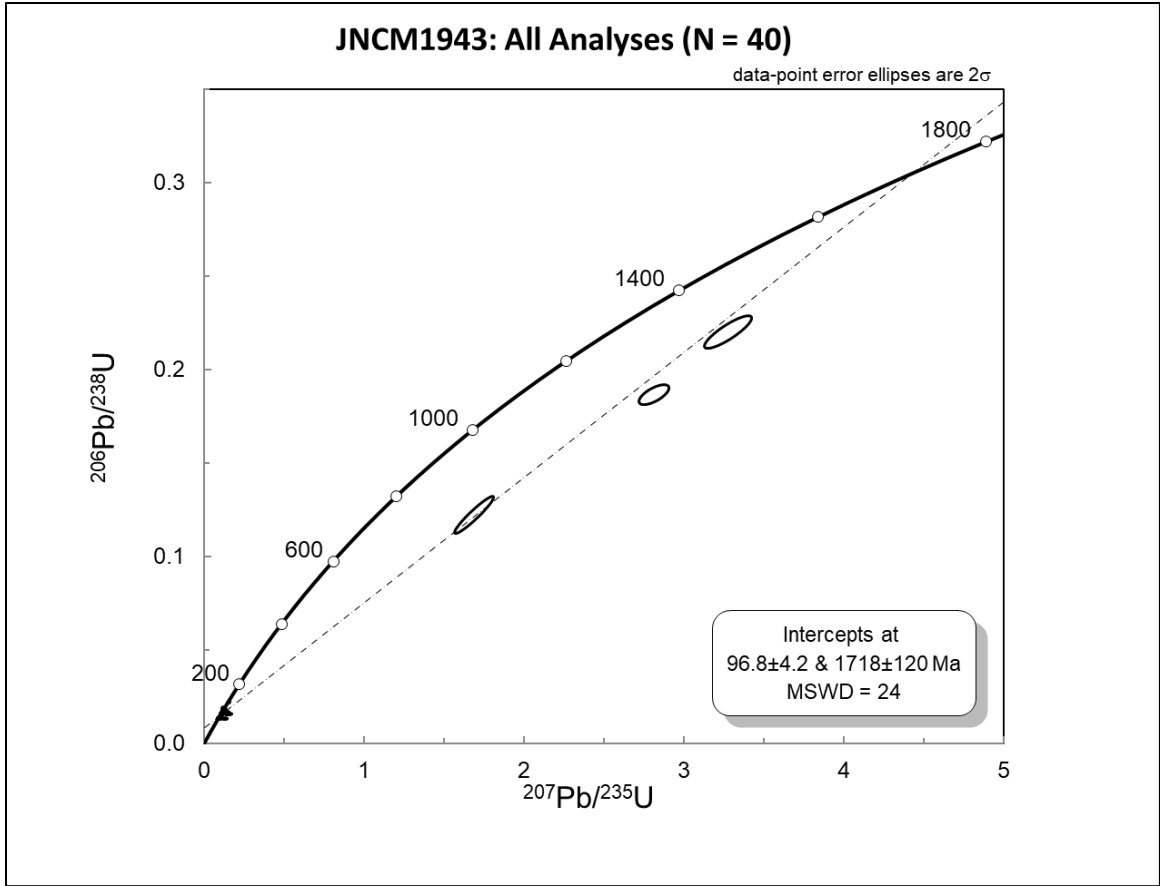


Figure 44. Concordia plot showing all analyses from JNCM1943 (Section 2).

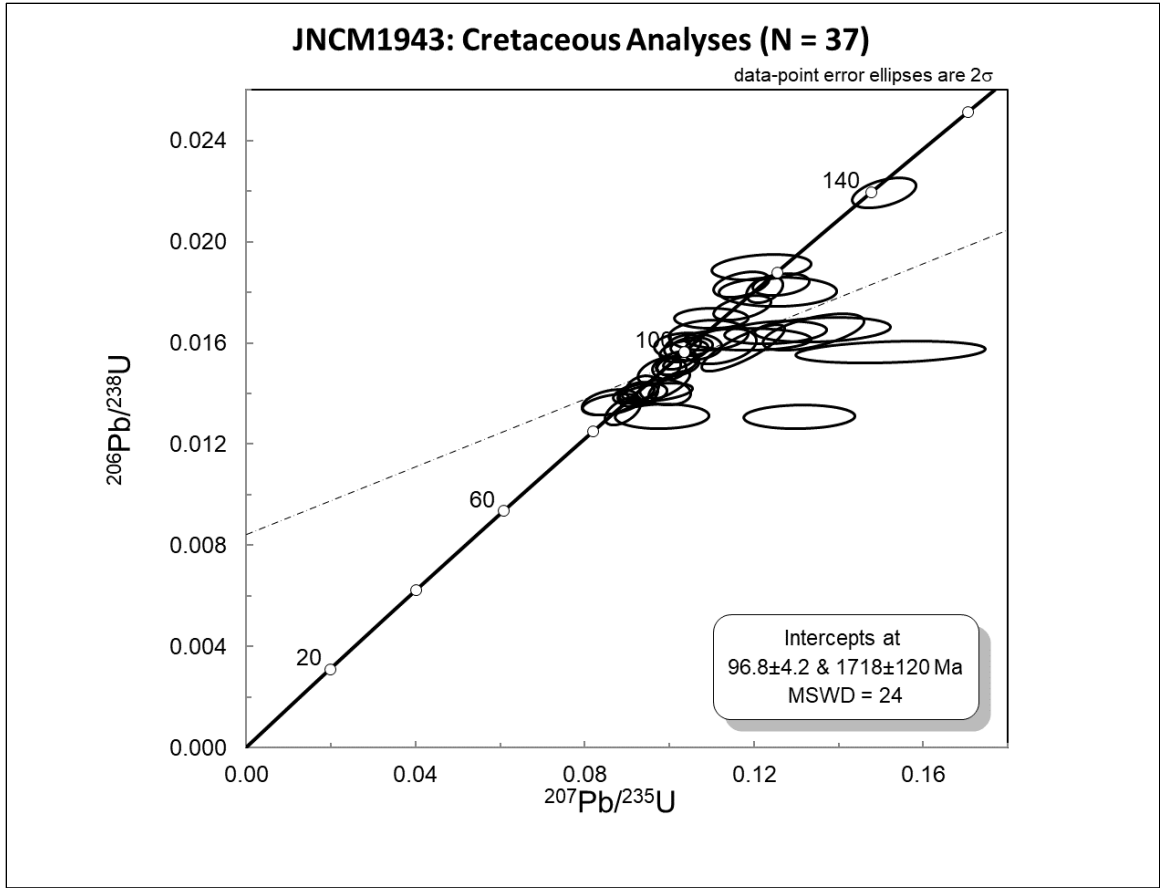


Figure 45. Concordia plot showing only Mesozoic analyses from JNCM1943 (Section 2).

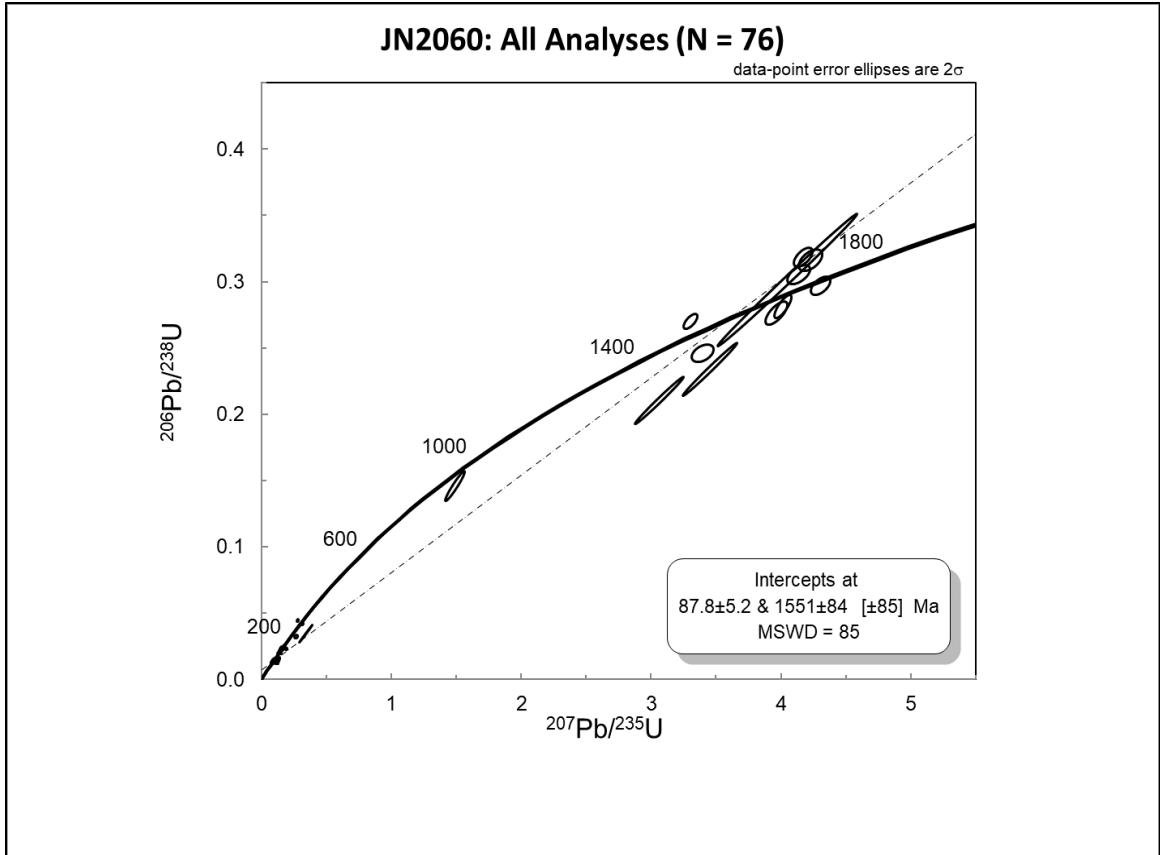


Figure 46. Concordia plot showing all analyses from JN2060 (Section 2).

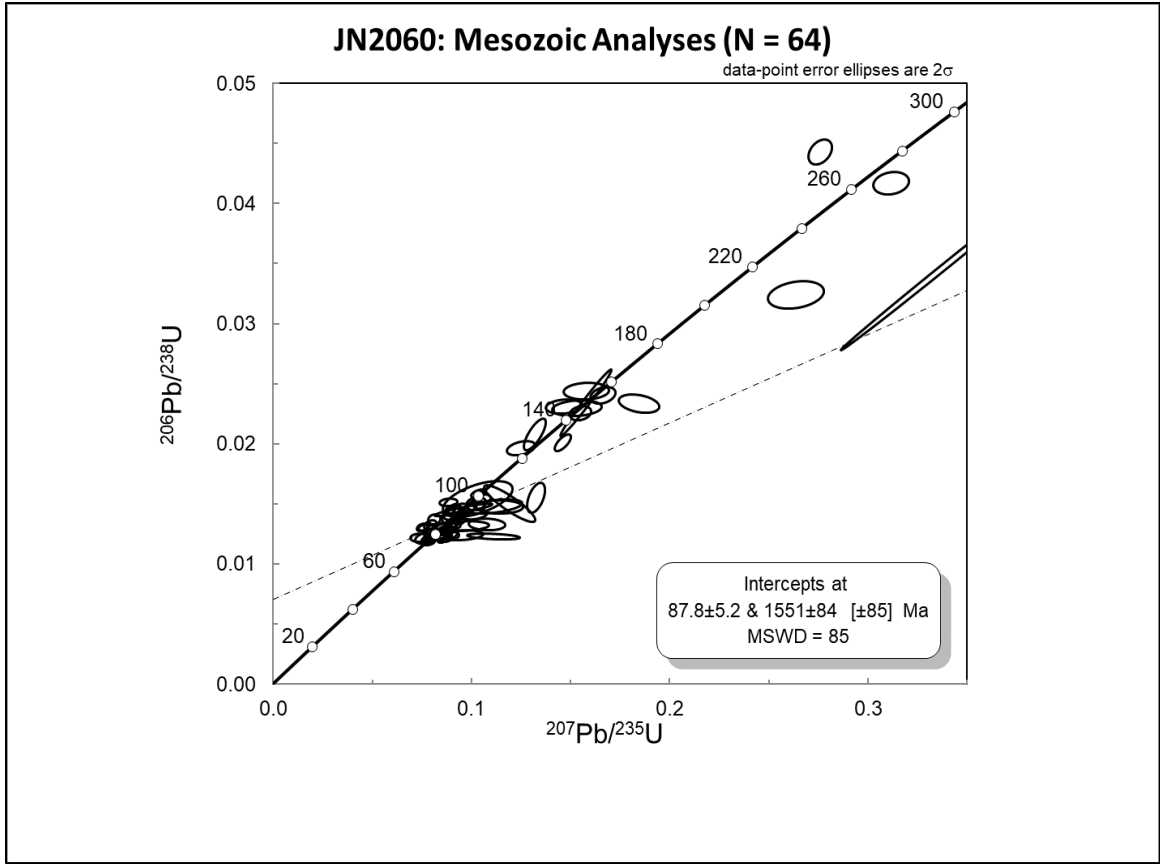


Figure 47. Concordia plot showing only Mesozoic analyses from JN2060 (Section 2).

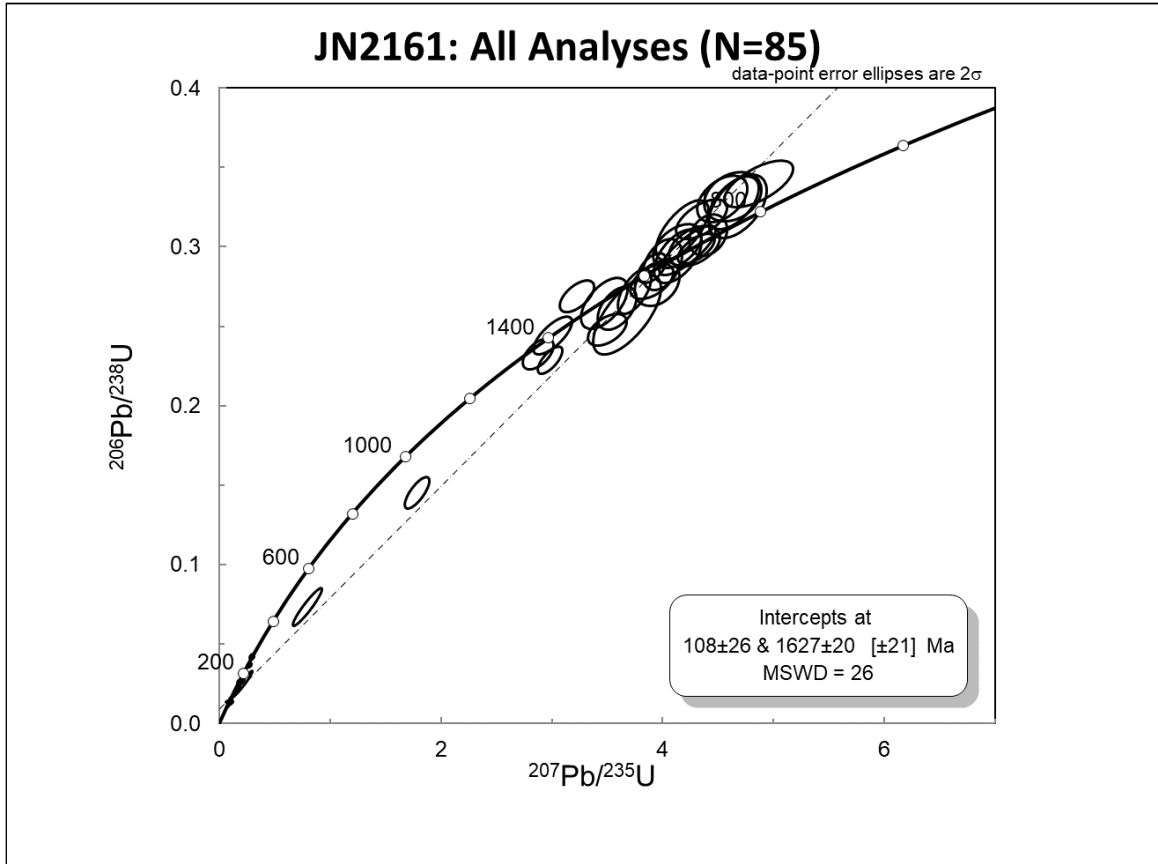


Figure 48. Concordia plot showing all analyses from JN2161 (East Fork block).

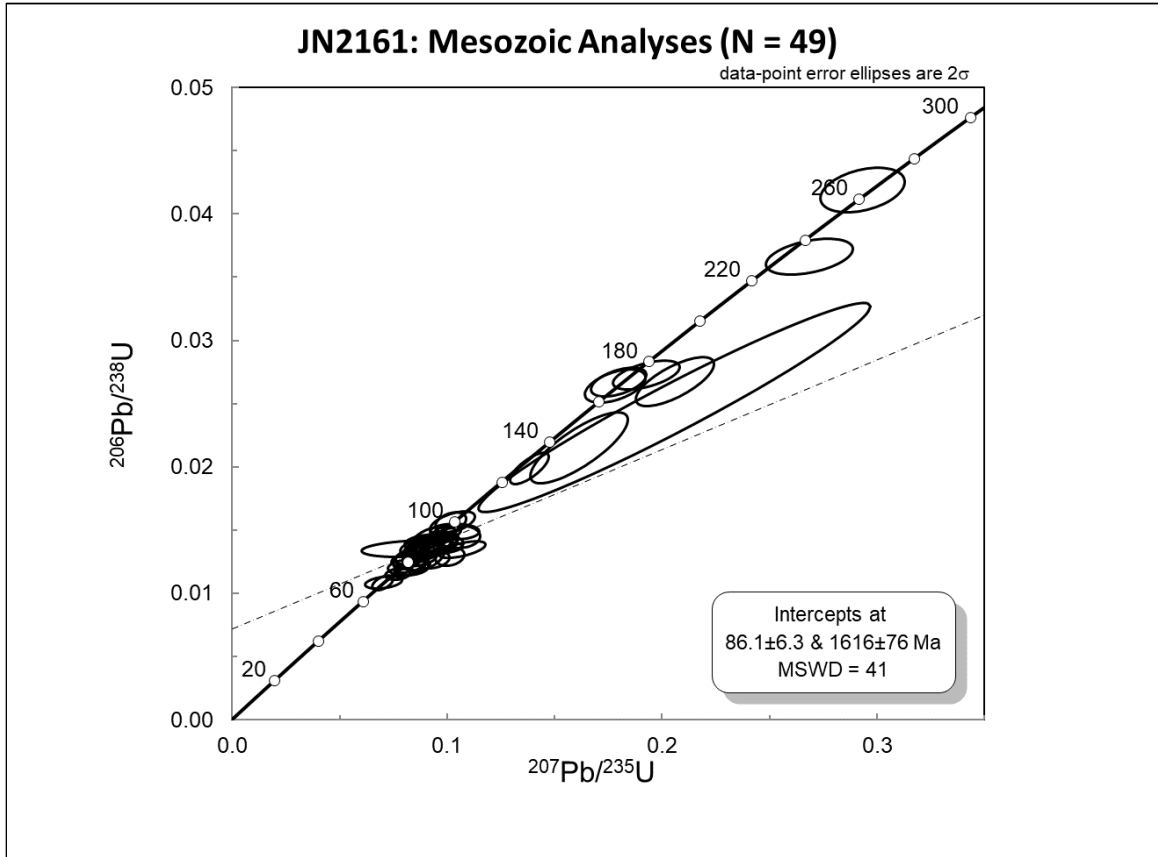


Figure 49. Plot showing only Mesozoic analyses from JN2161 (East Fork block).

Probability Density Plots

Probability density plots for each sample were created using Isoplot 4.5 (Ludwig, 2007). All plots are scaled to show only the Mesozoic analyses that dominate each sample. Color bars were overlaid using the color scheme of Jacobson et al. (2011) to define age bins of 55–70, 70–85, 85–100, 100–135, 135–300, and >300 Ma which correspond to igneous sources in southern California, southwestern Arizona, and northwestern Mexico (Figure 50; Grove et al., 2003; Jacobson et al., 2011). Included are the probability density plots for the two samples previously published for Blue Ridge, 98-240 and BR218 (Grove et al. 2003; Jacobson et al., 2011) for comparison with the

samples analyzed in this study (Figure 51). Finally, the age distribution for the Lupine Camp sample in the East Fork Block (JN2161) is shown on a separate plot (Figure 52).

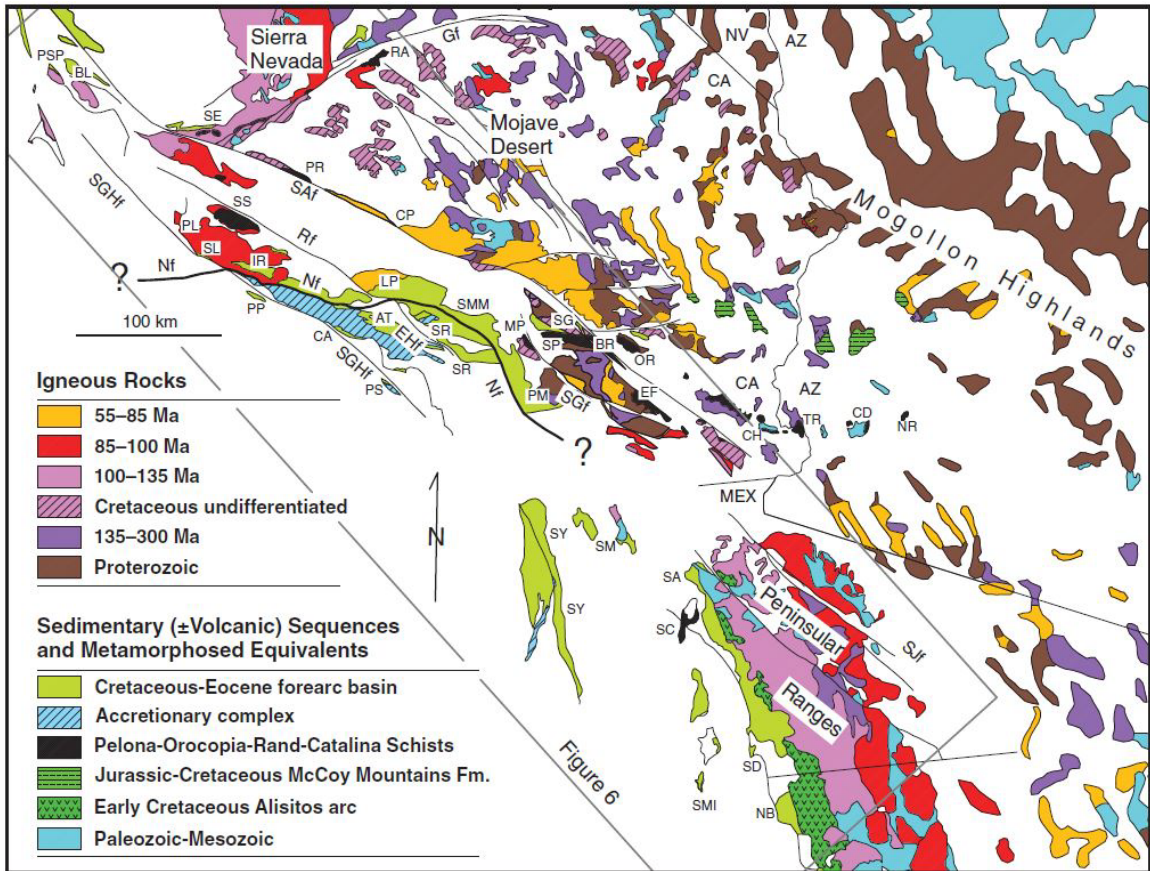


Figure 50. Index map showing igneous sources colored coded by age bins defined by Grove et al., (2003) and Jacobson et al., (2011). Source: Jacobson et al., (2011). This palinspastic map restores right-lateral displacements on various branches of the San Andreas fault system

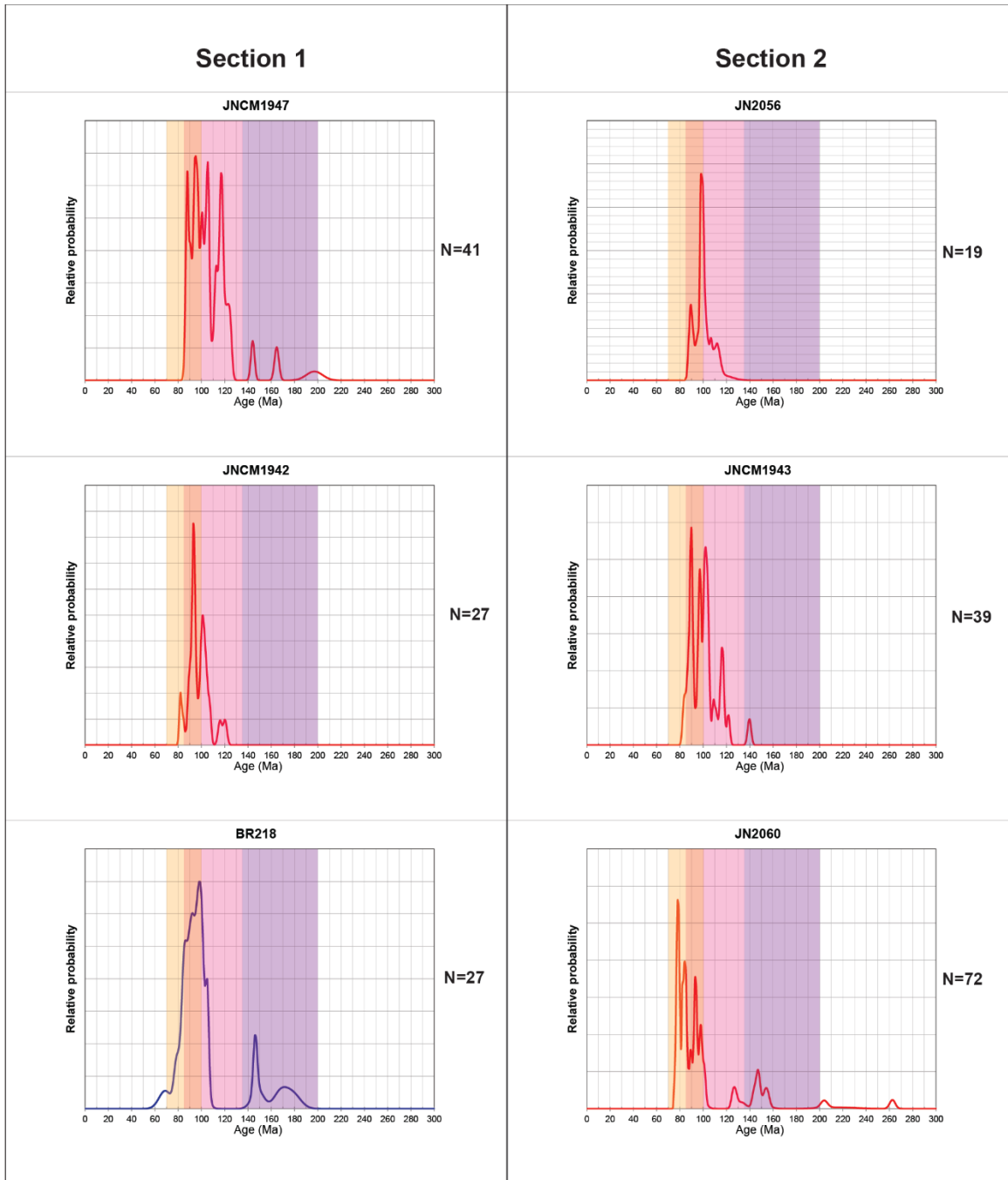


Figure 51. Probability density plots for Sections 1 and 2, Blue Ridge. Sample BR218 data are from Grove et al. (2003) and Jacobson et al. (2011). Only Mesozoic analyses are shown.

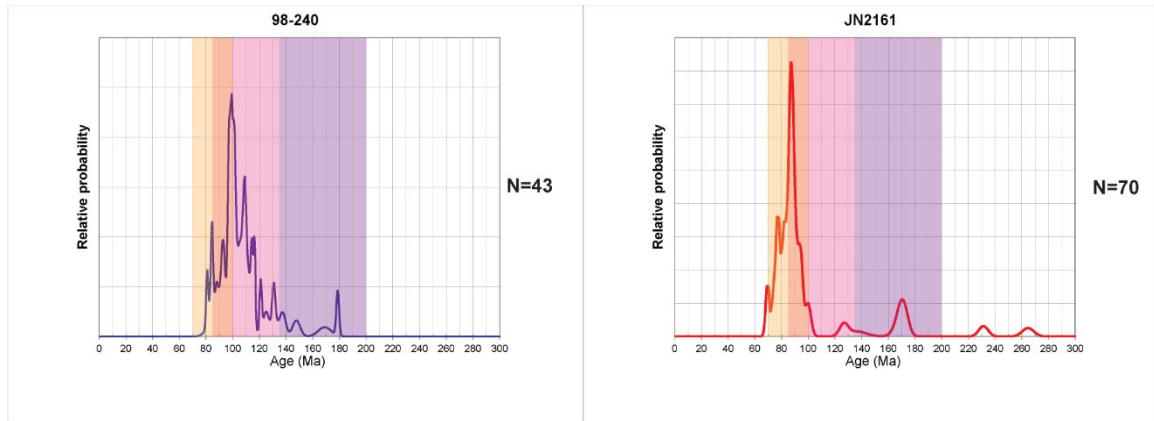


Figure 52. Probability density plots for Blue Ridge previous sample 98-240 (Grove et al., 2003; Jacobson et al., 2011) (left) and East Fork (right). Only Mesozoic analyses are shown.

Youngest Single Grain Analysis

Several methods exist for determining the maximum depositional age (MDA) of a sedimentary deposit. The youngest single grain or variations on the youngest discrete population of grains are commonly used because the sedimentary deposit is in principle, younger than its youngest grain or youngest grain population (Nelson, 2001; Fredo et al., 2003; Anderson, 2005). Grove et al (2003) and Jacobson et al. (2011) used pooled data from several samples per specific schist body to determine depositional age of the schist bodies and to analyze detrital zircon provenance. Crucially, the authors defined the depositional age of the schist protolith as being constrained by the youngest detrital zircon (YSG) and the oldest metamorphic age.

In true sedimentary deposits, Coutts et al., (2019) tested various methods to compare calculated maximum depositional ages with known depositional ages of several sedimentary deposits and found that that the youngest single grain (YSG), youngest detrital zircon (YSD) (which uses the program Isoplot to run the calculation), and weighted average of the youngest three grains (Y3Z) yielded the most accurate results.

Conversely, Vermeesch (2020) argued that all currently used methods are not statistically based and thus cannot accurately determine a correct MDA. Vermeesch instead proposed the maximum likely age (MLA) using the method of Galbraith and Laslett (1993) and Galbraith (2005) and uses a radial plot. It should be noted that the methods of Coutts et al., (2019) and Vermeesch (2020) use large data sets (>100 gains) in their analyses and are likely not directly applicable to the relatively low number of analyses per sample recovered in this study.

Here, I use the youngest single grain approach for simplicity because: (1) the data sets are relatively small so even one single grain is believed to be significant; (2) after the selection of acceptable analyses according to defined parameters, the analyses are considered to be reliable; and (3) each of the data sets have prominent early and middle Cretaceous age modes that stand out from the YSG. In addition, this data set will be compared with those of Grove et al. (2003) and Jacobson et al. (2011), and thus the youngest detrital zircon will be viewed as the upper limit of deposition. This approach is useful for comparing maximum depositional ages at different structural levels within the schist body.

As previously described, Section 1 contains samples JNCM1947, JNCM1942, and BR218 in stratigraphic succession from lowest to highest structural levels indicated by cross-sections B, C, and D (Figures 19, 20, 21). The youngest single grains for samples JNCM1947 and JNCM1942 yielded U-Pb ages of 87.2 ± 2.8 Ma and 81.8 ± 1.9 Ma respectively, younging up-section (Figure 53). Included in this section is sample BR218 (Grove et al. 2003; Jacobson et al., 2011) which yielded an age of 69 ± 10 Ma for the youngest single grain. Because this sample has a comparatively large uncertainty, the age

itself is close to the cutoff age of 68 Ma discussed previously for grains of metamorphic origin, and appears to be an outlier, the second youngest detrital zircon age of 79 ± 4 Ma, here labeled BR218b, may be more representative of the youngest single grain for the sample and is included for comparison with the data obtained in this study. Even if the youngest single grain for sample BR218 is discarded, the second youngest grain still shows a younging trend up-section, showing a normal proto-stratigraphic age succession.

Section 2 is represented by cross-section F-G'' (Figure 37) and shows the relative structural positions of samples JN2056, JNCM1943, and JN2060. The youngest single grains for samples JN2056, JNCM1943, and JN2060 yielded U-Pb ages of 88.3 ± 2.6 Ma, 81.7 ± 2.4 Ma, and 75.6 ± 1.2 Ma respectively (Figure 53). The results for Section 2 also show a younging trend up-section.

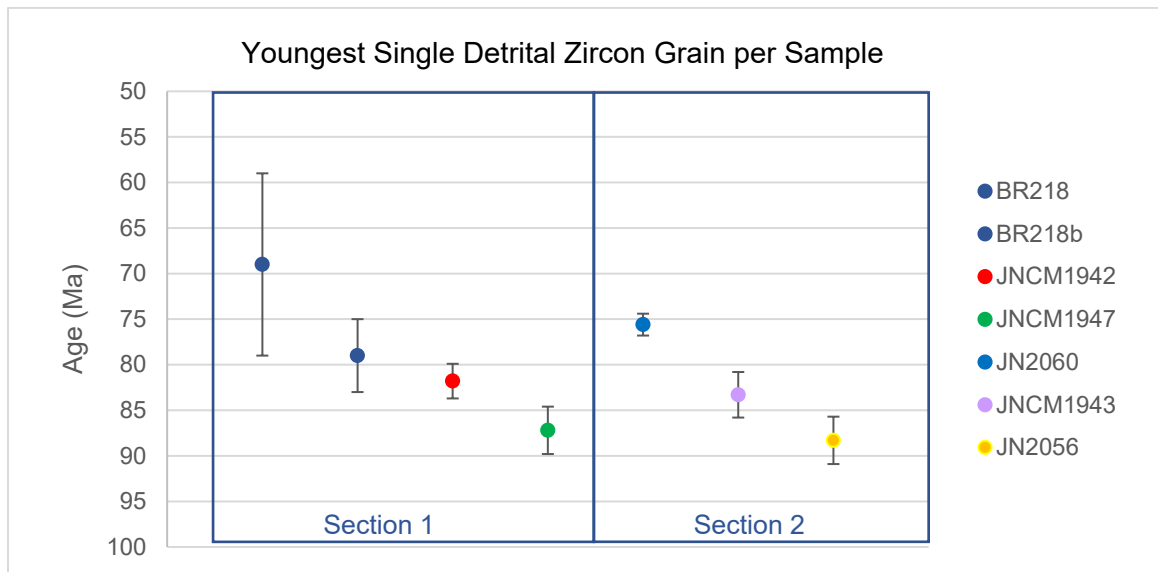


Figure 53. Plot showing the youngest single detrital zircon grain per sample for Sections 1 and 2. The samples are arranged in structurally descending order from left to right per section. Both sections show a younging trend up-section. Error bars are 2σ .

Determination of Structural Thickness Between Samples

Section 1

Geochronology samples JNCM1947, JNCM1942, and BR218 are located on three sub-parallel ridges correlative to cross-sections D, C, and B respectively (Figures 19, 20, 21). Due to the composite nature of Section 1, structural thickness between samples was determined by cross projecting the samples to adjacent ridges along strike and checking for agreement between the measurements for each cross-section. To determine the structural thickness between samples JNCM1947 and JNCM1942, sample JNCM1947, was projected onto the two nearest cross-section lines D and C, and sample JNCM1942, located on ridge D (cross-section D), was projected onto cross-section C. The measured structural thickness between samples JNCM1947 and JNCM1942 from cross-sections D and C yielded values of 1,962 ft and 1,901 ft respectively, with an average value of $1,931 \pm 30$ feet. To determine the structural thickness between sample JNCM1942 and the structurally highest sample BR218, located on ridge B (cross-section B), the previously projected position of JNCM1942 was projected along strike from cross-section C to cross-section B. The structural thickness between the two samples as measured by cross-section B yielded a value of 479 ft. The two relative thicknesses of 479 ft and 1931 ft between the samples in Section 1 are taken at face value since error propagation is complicated using map and scale measurements, handheld GPS accuracy (generally 3-5 m), and mathematical operations. The results are intended to provide a reference for the relative depth measurements and are assumed to incur some uncertainty. However, the uncertainties quantified by the U-Pb ages plotted at 2σ are used as the primary uncertainty in the following discussion and depth vs. age graphs.

Section 2

Relative depth measurements between samples in Section 2 were measured in two sections between sample JN2056 and JNCM1943 (Figure 37). The two measurements are identical, yielding a thickness of 2,375 ft between the samples. Measurements between JNCM1943 and JN2060 yielded a thickness of 2,132 ft between the samples using the same procedure. As in Section 1, the U-Pb age uncertainties are used as the primary uncertainty in the aforementioned discussion and graphs.

Relative Depth vs. YSG Age

To test whether Sections 1 and 2 are coherent sections, not disrupted by significant faulting or overturned folding, the youngest single grain ages were plotted against the depth profiles obtained for each section. If coherent, the mutually dependent variables of depth and age should plot along a linear regression line with an R^2 value near 1.0. Results for Section 1 show an R^2 value of 0.9765, indicating that the dated section is not significantly disrupted and preserves a normal proto-depositional sequence (Figure 54). This plot uses the second youngest grain of 79 Ma (BR218b) as per the argument stated previously regarding the youngest single grain of 69 Ma (BR218) being of metamorphic origin. To test whether this remains a valid supposition, the data for Section 1 was plotted again using the youngest single grain (BR218) and the results yielded an R^2 of 0.7129 (Figure 55). This shows that the degree of agreement between depth and age for Section 1 using the 69 Ma grain is relatively low and reinforces the interpretation that the 69 Ma date is an outlier or of metamorphic origin.

The results for Section 2 show an R^2 value of 0.9999, indicating that the dated section is not significantly disrupted and preserves a normal proto-depositional sequence (Figure 56).

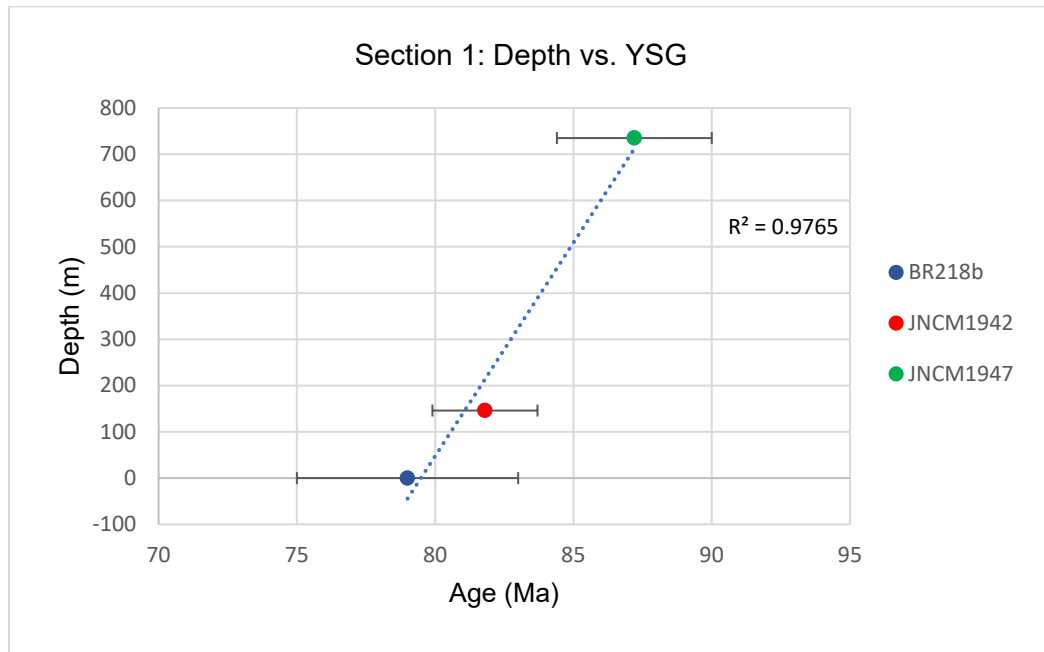


Figure 54. Relative depth vs. age plot showing the relationship between depth and age for Section 1. This plot uses the second youngest zircon grain (BR218b) with an age of 79 Ma. The R^2 value indicates a normal proto-depositional sequence.

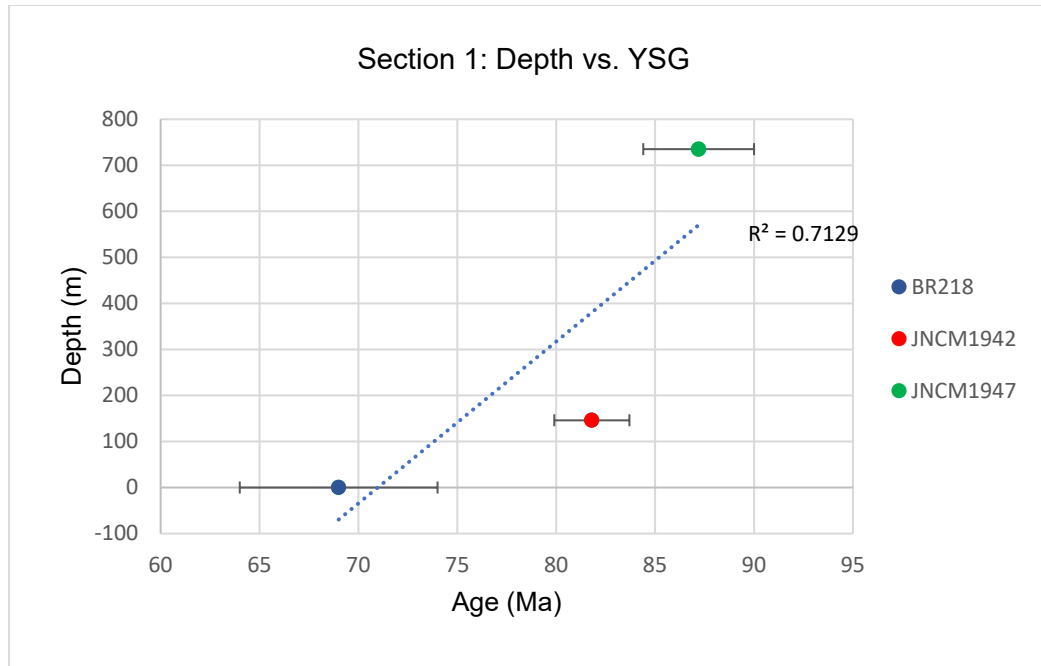


Figure 55. Relative depth vs. age plot showing the relationship between depth and age for Section 1 using the second youngest zircon grain (BR218) with an age of 69 Ma. The R^2 value indicates a low degree of agreement between depth and age. This reinforces the idea that the 69 Ma grain is of metamorphic origin.

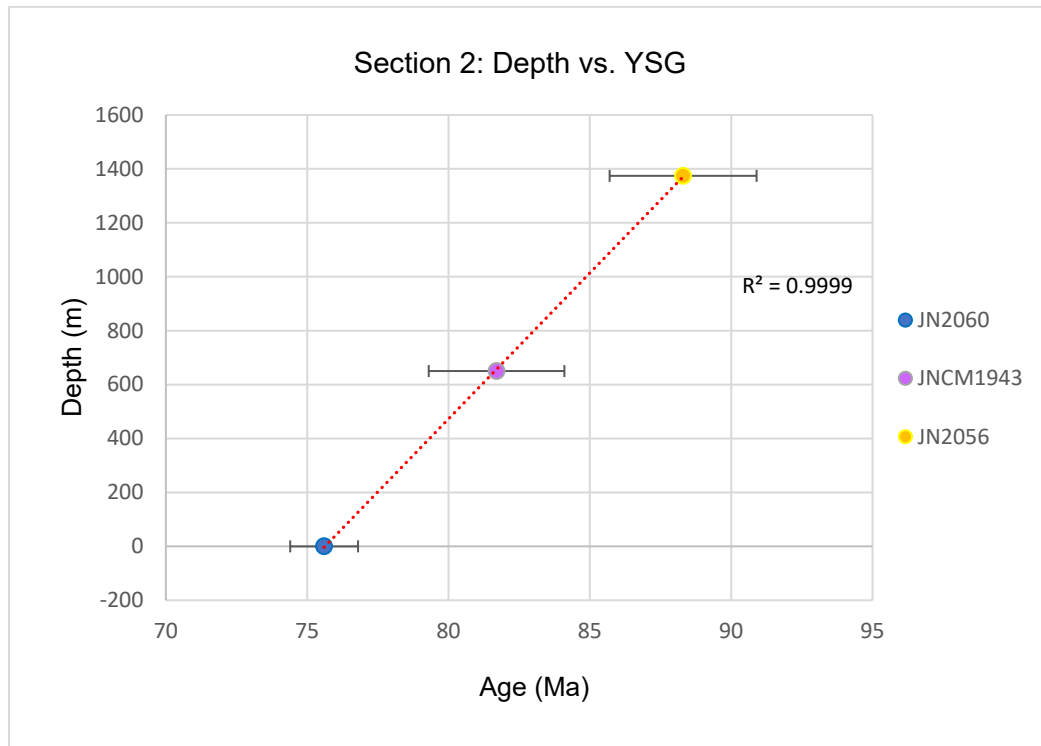


Figure 56. Relative depth vs. age plot showing the relationship between depth and age for Section 2. This section is apparently coherent. The R^2 value indicates a normal proto-depositional sequence.

DISCUSSION AND INTERPRETATION

Thin Section Petrography

A significant finding of this study is that metamorphic grade of the Blue Ridge schist units is quite uniform at all sampled structural levels. Although the metamorphic mineral assemblages vary with protolith type and bulk composition as expected, there does not appear to be any systematic change in metamorphic grade from deep to shallow structural position (Table 1). Approximately 1,815 m of total thickness (measured perpendicular to foliation in significantly strained and flattened metamorphic strata) is exposed in the study area, so it is interesting that metamorphic grade remains relatively constant throughout the 56 analyzed Blue Ridge samples.

Most of the Blue Ridge greyschist samples contain garnet and biotite (as opposed to chlorite), and several greenschists contain hornblende and garnet rather than actinolite and chlorite. Many samples display intergrowths of biotite with chlorite and/or hornblende with actinolite. In general, these observed mineral assemblages are comparable to the garnet-bearing albite-epidote-amphibolite zone documented by Graham and Powell (1984) in the central part of Sierra Pelona. That zone represents the uppermost greenschist-lower amphibolite facies boundary. The hornblende schists and spotted mafic schists (Table 1) contain abundant hornblende with no actinolite, suggesting a somewhat higher metamorphic grade (oligoclase zone of the amphibolite facies; see also Graham and Powell, 1984).

Thermobarometric studies of Sierra Pelona (Graham and Powell, 1984) and the Rand Mountains (Jacobson, 1995) provide important context for Blue Ridge. In both cases, inverted metamorphic zonation (up-section increase in metamorphic grade) is

documented in post metamorphic antiforms capped by major thrust faults (the Pelona fault and Rand thrust, respectively). A section of schist approximately 2 km thick is exposed in the Sierra Pelona antiform. Greenschist facies assemblages in the core transition upward to a 500 m thick zone of garnet-bearing albite-epidote-amphibolite facies rock; this in turn is overlain by a 100-200 m thick hornblende-bearing oligoclase zone (amphibolite facies) adjacent to the Pelona fault (labeled as “Vincent thrust” on Figure 5 of Graham and Powell, 1984). The exposed structural thickness in the Rand Mountains antiform is ~ 3 km (Jacobson, 1995). Here, a continuous spectrum of 4 metamorphic facies was identified, from deepest levels to shallow: epidote blueschist, greenschist, albite epidote-amphibolite, and lower amphibolite (oligoclase zone). In contrast, the blueschist and green schist zones are missing at Blue Ridge. Most of the Blue Ridge schist was metamorphosed at albite-epidote-amphibolite facies, above the garnet isograd. It is difficult to demonstrate an inverted metamorphic gradient, other than the observation that several hornblende schists and hornblende-bearing spotted mafic schists (representing the oligoclase zone of amphibolite facies) are present near Guffy Campground and along Prairie Fork Road (Table 1). These samples probably reside at high structural levels, but structural position is difficult to confirm due to complex folding and section duplication in this area. Unfortunately, there is no Vincent thrust exposed on Blue Ridge to use as a structural marker.

The tectonic reconstruction by Dillon and Ehlig (1993) suggests that Sierra Pelona and Mt. Pinos represent a western continuation of Blue Ridge (Figure 3). One noteworthy observation is that several map-scale fold axes shown on the various published maps of Sierra Pelona display gentle westward plunges (Muhlberger and Hill,

1958; Dibblee, 1961; Hernandez, 2012; Hernandez and Olson, 2012). This pattern suggests that Blue Ridge would represent deeper structural level if that schist body was originally connected to the eastern end of Sierra Pelona. Also, some of the large wavelength folds mapped on Blue Ridge plunge gently to the northwest (Plate 1), and there seem to be more of these folds, with more closely spaced hinges. Perhaps the more abundant map scale folds observed at Blue Ridge are the result of (1) a region of the schist that was originally more deeply buried, and (2) effects of greater shortening strain during the later folding event.

Another interesting observation is that the Blue Ridge samples record higher metamorphic grade compared to the predominantly greenschist facies assemblages reported from a broad region of the East Fork block (Jacobson, 1983a; Jacobson, 1995; also 5 thin sections from this study described earlier). In contrast to Sierra Pelona (Graham and Powell, 1984), the entire East Fork block was metamorphosed below the garnet isograd, and there is not a profound inverted metamorphic zonation when approaching the Vincent thrust, despite an exposed thickness of 4 km. This finding was reinforced by detailed electron microprobe studies of Jacobson (1983a; 1995). He observed only subtle up-section variations in muscovite composition and An content in plagioclase. Also, Na/Al ratios measured in amphiboles indicate that structurally high samples record lower pressures than those deep in the section. Currently the Blue Ridge schist body lies adjacent to the East Fork block, but it is important to note that these areas were widely separated prior to right-lateral displacements on the Punchbowl and San Jacinto fault zones.

Structure

Folding

Folds are ubiquitous on Blue Ridge and present opportunities to understand the complex tectonic history of Pelona schist that was presumably deformed and metamorphosed in a subduction zone. In the Research Questions posed earlier, the goal was to distinguish outcrop-scale folds from map-scale folds in terms of structural style (geometry), orientation, and overprinting relations. My interpretations are guided by viewing the distribution of two sets of fold data: 1) map patterns of foliation reversals that constrain the trends of fold hinges at the scale of Plate 1, and (2) stereonet plots of many subareas of outcropping folds that permit statistical solution of fold axis orientations and axial planes as well as asymmetries that pertain to fold vergence directions.

Upon assessment of all fold data, a significant observation is that two distinct compression directions emerge if one assumes that fold hinges are oriented perpendicular to the maximum principal stress direction. This is a reasonable assumption because little curvature of fold hinges was observed in the field, nor were sheath folds encountered. Also, most of the stereonet solutions display fairly well-constrained best-fit fold axes. Hence, it seems appropriate to subdivide the folds into two groups with different mean trends that record two distinctive compressional events. As discussed below, an early generation of folds characterized by northerly-trending hinges usually observed at outcrop scale is overprinted (refolded) by a younger generation of folds with northwesterly hinges and larger wavelengths delineated by dip reversals of foliation at map scale.

Syn-metamorphic Folds with Northerly Hinges

An early generation of tight folds with east-northeast to north-northwest trending hinges is interpreted to be syn-metamorphic in that folding of compositional layering occurred during development of prograde metamorphism. Away from the fold hinges, foliation in the host rock is sub-parallel to axial planes of the folds. These folds are observable at outcrop scale and generally characterized by short wavelengths on the order of a few cm to a few meters. In area F (described below) the wavelength is longer and varies from ~10 m to ~200 m.

The stereonet of Figure 31 shows a composite of foliation poles measured from limbs of tight folds that are distinguishable at map scale. This Pi diagram yields a best-fit mean fold axis of S18E/10 with a mean axial plane of N17E/87SE. This data set includes a group of symmetric tight folds measured northwest of Guffy Campground (Figure 30) that has north-northwest trending hinges and a mean axial plane of ~N10W/85NE. Smaller scale asymmetric S and Z folds measured at Area B (Northwest Ridge; Figure 33) and Area E (Figure 35) are also interpreted to be syn-metamorphic. When the younger folding event is removed, these areas preserve gently plunging fold hinges with trends between N30W and N10E. Altogether, the calculated mean hinge orientations associated with the tight folding event demonstrate that the compression direction (maximum principal stress direction) associated with syn-metamorphic folding varies from N78E-S78W to N73W-S73E. This easterly compression direction is significantly discordant to the N29E-S29W direction calculated below for the younger generation of open map scale folds.

The tightly folded banded schist unit of Area F (Plate 1) is a key place to demonstrate that small scale S and Z folds formed as flexural-slip parasitic folds on the limbs of map scale folds. The stereonet of (Figure 34) summarizes all the data measured along this ridge. A series of tight folds defined by foliation reversals preserve a best fit cylindrical fold axis of S20W/15 and a mean axial plane of S20W/84SE. Asymmetric S and Z folds measured within two adjacent fold limbs at Sites 774 and 762 and display shear sense consistent with flexural slip. Associated fold hinges plunge gently N60E and N15E, respectively. This syn-metamorphic fold system developed under a compression direction of N70W-S70E.

Post-Metamorphic Folds with West-Northwest Hinges

A younger generation of folds is recorded by open folding of metamorphic foliation with hinges delineated by map-scale dip reversals on Plate 1. Wavelengths typically vary from tens to hundreds of meters. Most of the folds identified in this study occur close to the crest of Blue Ridge where detailed mapping was focused. However, when structural data from Ehlig and Dibblee (1967) and Dibblee and Minch (2002) are incorporated, it appears that these open folds pervade the entire Blue Ridge schist body from the Punchbowl fault on the southwest to the San Andreas fault on the northeast. In all cases, the trend of mapped fold hinges is approximately parallel to the axis of Blue Ridge. As shown in the stereonet solution of Figure 32, a Pi diagram of foliation poles measured from limbs of the younger folds yields a best-fit cylindrical fold axis of S60E/14, with a mean axial plane of N61W/82 SW. The mean compression direction (maximum principal stress direction) associated with the formation of these open folds was N29E-S29W. This shortening direction contrasts markedly to the north-northwest compression associated

with similar open folds in Sierra Pelona that trend S85W to S60W (Muelberger and Hill (1958); Dibblee (1961), Hernandez (2013), Hernandez and Olson (2013).

Two outcrops of calcsilicate gneiss in Area E (Plate 1) convincingly demonstrate that an open synform with trend/plunge of N80W/5 is superimposed on a marker unit with unidirectional west-vergent S and Z folds. A fold test of this relationship is presented by the stereonet of Figure 35. A large population of S fold hinges contained in the north-northwest dipping fold limb is plotted along with two Z fold hinges contained in the south-dipping limb. When the openly folded foliation is rotated to horizontal, the S fold hinges restore to a mean orientation of N12W/5, while the Z fold hinges restore to S5W/17. Axial planes of these asymmetric folds display gentle east dips upon restoration. The following tectonic sequence is interpreted from this data set: A calcsilicate bed developed west vergent, small scale asymmetric folds during underthrusting and prograde metamorphism of the Pelona schist. A later (post-metamorphic) compressional event deformed the calcsilicate into a broad synform, one of many west-northwest trending folds that pervade the Blue Ridge schist.

The west-northwest trending fold hinges with highest confidence are constrained by foliation measurements taken during this study (Plate 1). Perhaps the most important fold is a synform that contours the south flank of Blue Ridge between Ridge B and Ridge E. This synform hinge marks an abrupt transition from south-southwest dipping foliations to north-northeast dipping foliations. Several other fold hinges mapped on Plate 1 away from focus areas of this study are loosely constrained by foliation data compiled from Ehlig and Dibblee (1967) and Dibblee and Minch (2002). The latter data source is somewhat questionable because many of the foliation symbols lack dip values, and those

showing dip are so regular that one wonders if they were estimated from a distance. Nevertheless, the compiled data sets permit delineation of a major southeast-plunging synform that roughly follows the trace of Cross Section G. This interpretation provides a viable explanation for the anomalous region of east and southeast-dipping foliations exposed along East Blue Ridge Road between Blue Ridge Campground and Microwave Camp (Plate 1).

The age of compression associated with large wavelength map scale folds in Blue Ridge, Sierra Pelona, Orocopia Mountains, and East Fork block remains a matter of debate.

Late Cenozoic Faulting

A minor aspect of this study has been assessment of post-metamorphic faulting. The original thought was that several north-northeast trending valleys that transect Blue Ridge between Northwest Ridge and Blue Ridge Campground might delineate traces of Late Cenozoic faults. As documented by Nourse (2002) and Morton and Miller (2003), the stratigraphy of the San Gabriel Mountains is disrupted by several left-lateral faults with northeast trends, e.g., the Stoddard Canyon, San Antonio Canyon, and San Dimas Canyon faults. These faults have appropriate orientations and shear sense to be rotated conjugates to the right-lateral San Andreas fault system. They were important in facilitating clockwise block rotations as the transform plate boundary evolved.

Apparent discontinuities in mapped schist stratigraphy occur across three of the aforementioned valleys (Plate 1). Unfortunately, outcrop is non-existent and colluvium or thick brush cover valley axes where faults are inferred. The best field evidence for a left-lateral fault system is a series of striated fault surfaces mapped along the fire road that contours the northwest side of Ridge D. These striated surfaces show oblique left-lateral

reverse motion along northeast-striking planes. Shear sense determinations are based on brittle fault indicators such as Reidel shears, stepping fiber bundles, and tool marks, following methods described in Petit (1987). Although these scattered outcrops do not represent a major fault zone, their occurrence may support the existence of a buried fault in the valley to the northwest of Ridge D.

Geochronology

Protolith Age

Some of the most exciting outcomes of this study are the geochronology results of Sections 1 and 2. Both sections show a younging trend up-section indicated by the youngest single grain from each sample. The relative structural depth measurements between each sample show a linear relationship between age and depth with a strong degree of agreement (i.e. R^2 values of 0.9765 and 0.9999 for Sections 1 and 2 respectively). In practicality, this means that when combining detailed structural mapping and cross-section construction with geochronologic sampling, it may be possible to treat the schist as an intact quasi-stratigraphic record suitable for detailed analysis of temporal changes in provenance. This differs from the pooled samples per schist body presented by Grove et al. (2003) and Jacobson et al. (2011) where the data show an upper limit for deposition and combined provenance signature of the schist bodies. In the aforementioned studies, these signatures are compared to other schist bodies to detect spatial and temporal changes between them.

Here, I argue that in treating the individual schist body as a quasi-stratigraphic record, temporal provenance changes may be detectable in greater detail which might provide new insights into the regional development of the subduction parallel margin.

Impediments to this procedure may be the uncertainties determined for the U-Pb ages themselves, and the hugely time-consuming mapping and cross-section construction needed to determine the true structural relationships between sample locations. Nevertheless, this might be a useful provenance supplement to forearc strata studies, especially in areas where the forearc is missing and the depocenter of the schist can be reasonably assumed. It is acknowledged here that the conclusions based on the Blue Ridge sections are limited by both the number of samples and the low number of analyses per sample, therefore, it is suggested that additional work be done to confirm or disprove this hypothesis.

Maximum Depositional Age (MDA) of the Schist Body

As discussed in the previous works section, the youngest previously reported ages for Blue Ridge show an age gap between 69 Ma and 79 Ma. Results of this study show that the youngest age reported for Blue Ridge (69 Ma) is either an outlier or a metamorphic age or both. The samples analyzed in this study indicate an upper limit of 75.6 Ma for deposition of the protolith on Blue Ridge. However, this is a mid-structural level age, determined by detailed mapping carried out during this study as well as previous mapping by Dibblee and Minch (2002).

Extrapolation of Youngest Single Grain for Exposed Structural Thickness

To estimate the maximum depositional age of the structurally shallowest portion of the exposed schist body, a linear regression model is used to extrapolate the expected age of the youngest single grain. To construct the model, I used the average foliation strike/dip value of 113.6/44 SW as determined by Stereonet 10.0 from cross-section C (Figure 18; Plate 1). Two parallel sections were selected to test for validity. Transect TC-1 is anchored at C'' on the geologic map and extends to the Blue Ridge fault of Coffey et

al. (2019) to the southwest. Transect TC-2 is anchored to geochronology sample site JNCM1947 and also extends southwest to the Blue Ridge fault.

Youngest detrital zircon ages and relative structural depth measurements between samples BR218b, JNCM1942, and JNCM1947 obtained from composite Geochronology Section 1 are projected along the transects of the ridge (Figures 57 and 58). The structural thickness of the transects are derived from extending the 44 degree average dip angle projected from sample site JNCM1947 to the right angle intersection of the most southwestern schist exposure. Measured structural thicknesses for transects TC1 and TC2 are 1,753 m and 1,815 m respectively.

The procedure for determining the expected age of the shallowest level of Blue Ridge is as follows: Using the total structural thickness values, age vs. depth data is recalculated for the geochronology samples while maintaining relative structural depth measurements between samples, and replotted (Figures 59 and 60). The resulting linear trendline equation is used to determine the y-intercept at depth 0.0 m, which is 68.8 Ma and 61.1 Ma for transects TC-1 and TC-2 respectively. These values represent the expected maximum depositional ages for the uppermost exposed section of the schist along the transects, assuming the section is not significantly folded or duplicated along this transect. Figures 61 and 62 show the linear models with extrapolated YSG ages of 68.8 and 68.1 Ma plotted and the resulting R^2 values.

The average expected YSG for Blue Ridge of approximately 68.5 Ma as determined by the linear model is consistent with that of the Sierra Pelona schist body which is characterized by a YSG age of 68.9 Ma.

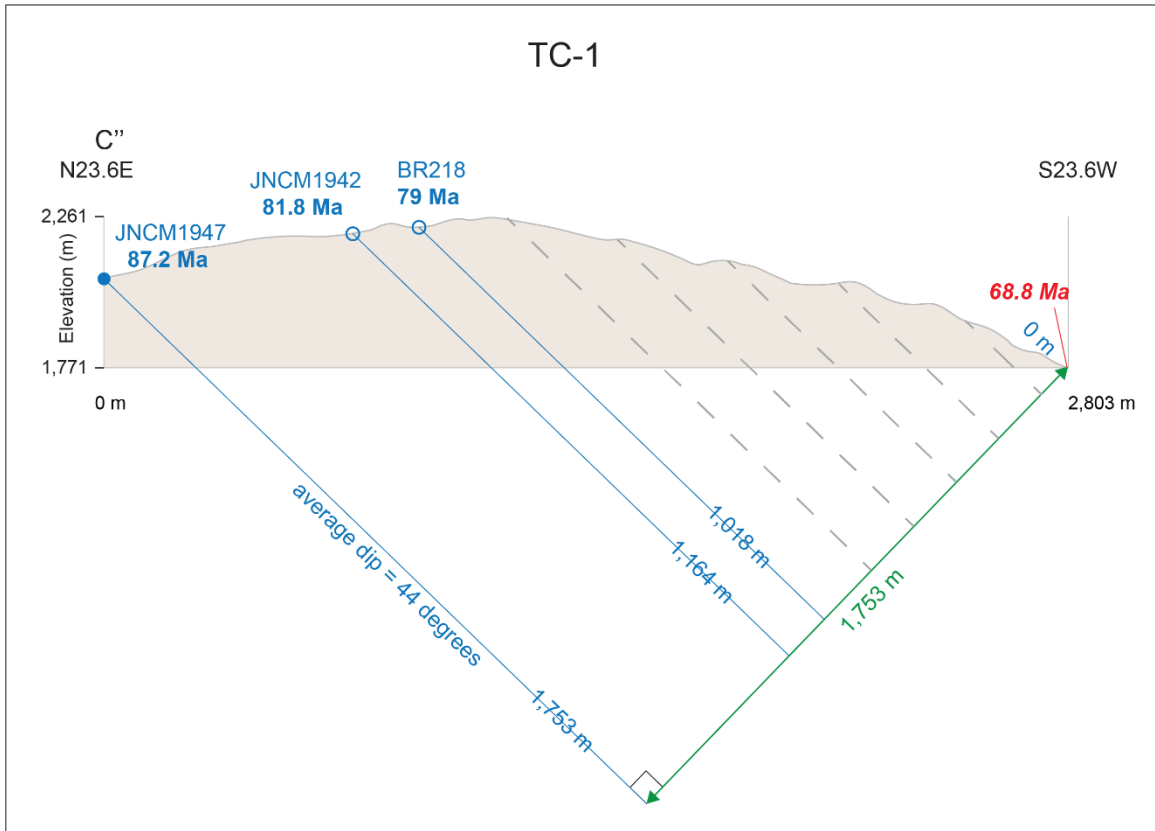


Figure 57. Transect 1 with projected age/depth model. Resultant YSG is labeled in red.

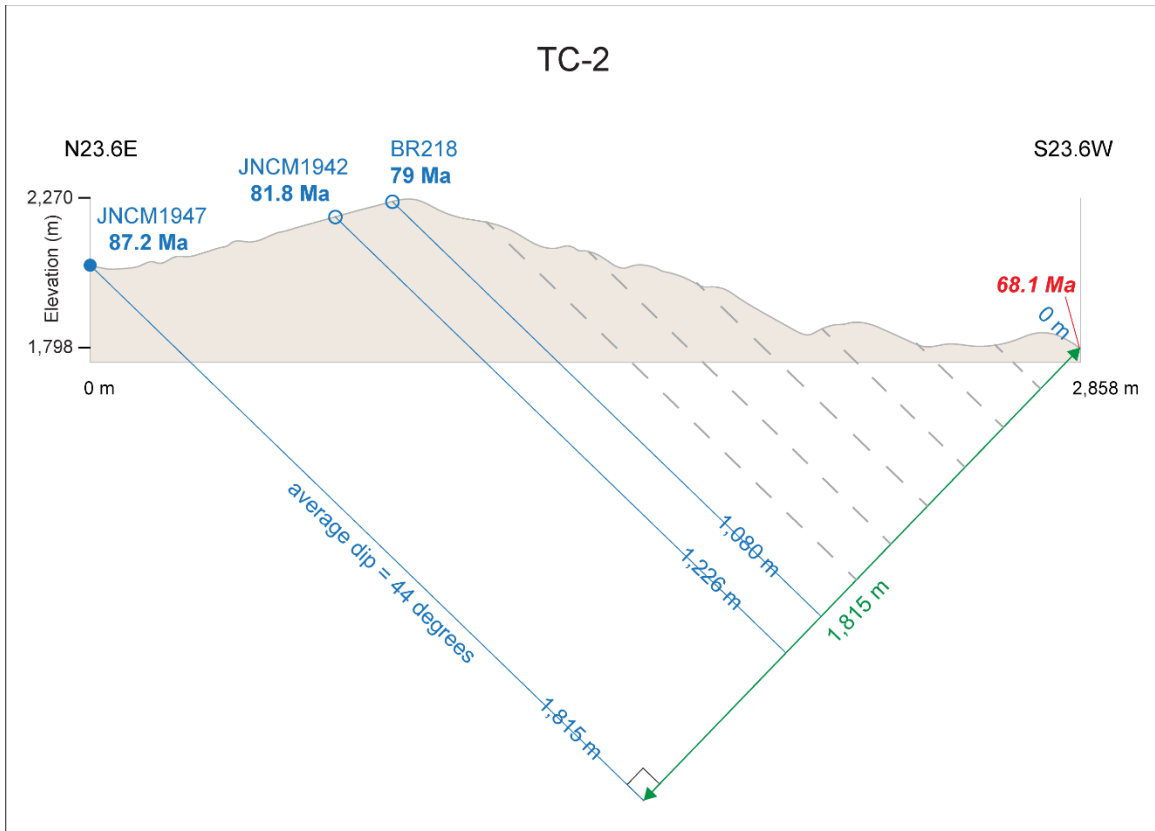


Figure 58. Transect 2 with projected age/depth model. Resultant YSG is labeled in red.

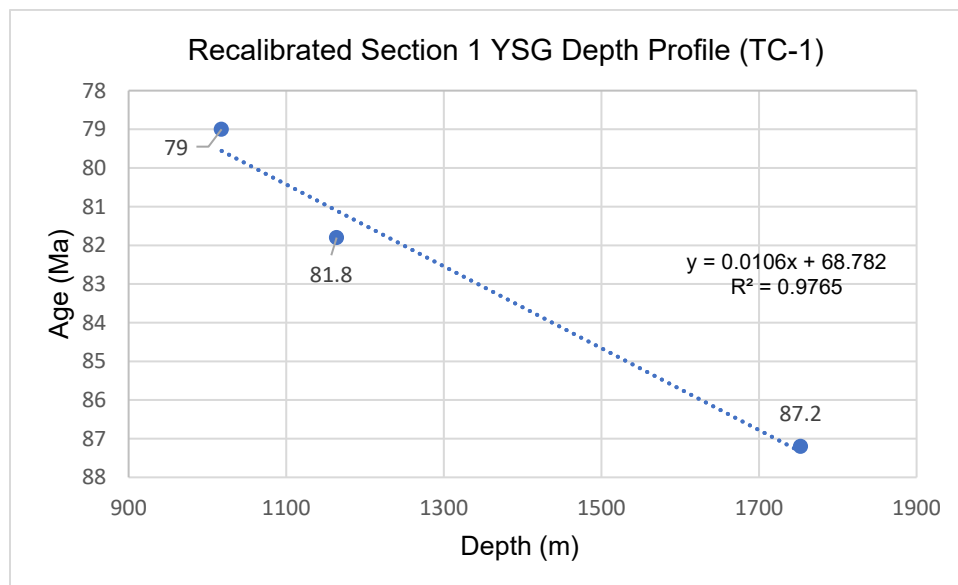


Figure 59. Section 1 relative depth profile re-calibrated to reflect the measured structural section.

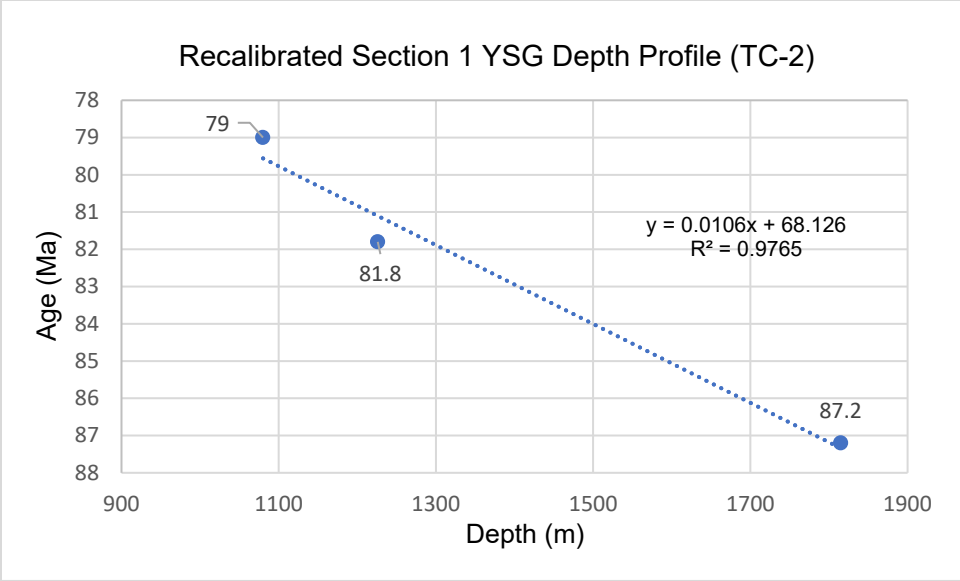


Figure 60. Section 1 relative depth profile re-calibrated to reflect the measured structural section.

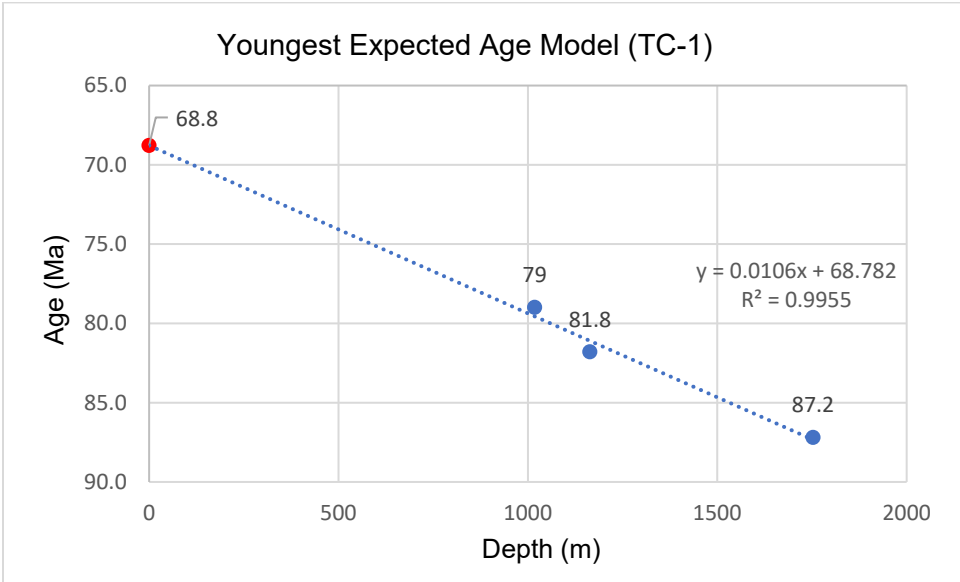


Figure 61. Linear model with expected YSG age for TC-1 plotted.

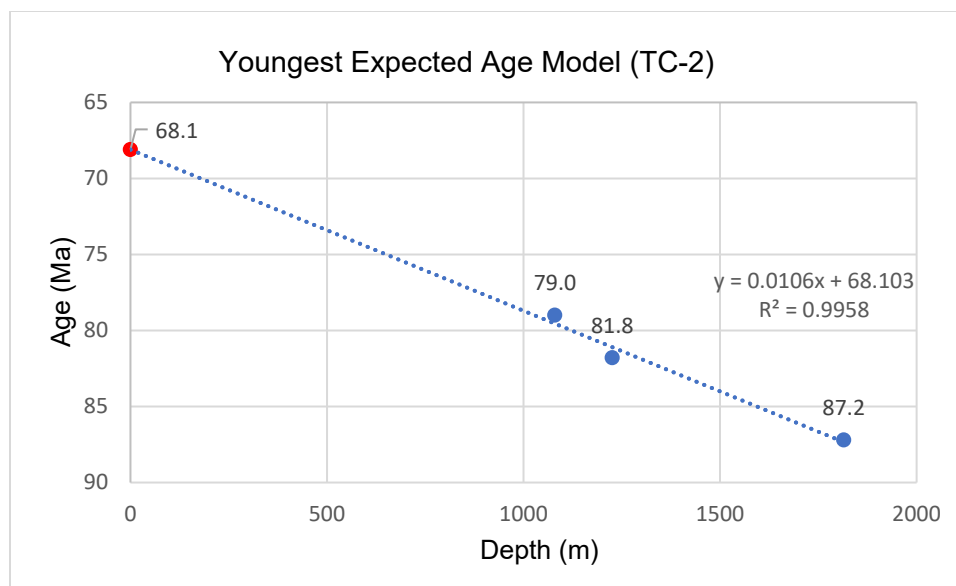


Figure 62. Linear model with expected YSG age for TC-2 plotted.

Detrital Zircon Provenance

Detrital zircon data for our five samples was grouped by similar age bins and color schemes utilized by Jacobson et al. (2011) for ease of comparison with previously published data for Mount Pinos, Blue Ridge, Sierra Pelona, and Orocopia schist bodies. These colors correspond to ages of basement in southern California and northwestern Mexico that pose feasible provenance sources (Figure 50). Following the procedure of Jacobson et al. (2011), percentage pie charts were created by assigning detrital zircon ages per sample to age bins of 55–70, 70–85, 85–100, 100–135, 135–300, and >300 Ma, and then were normalized to percentages. Also shown are bar graphs of the same data. Samples are arranged in the aforementioned Sections 1 and 2.

Detrital zircon provenance refers to the age populations and quantity of detrital zircons within each geochronology sample. The age populations (age bins) are representative of basement rock sources from which the zircons are derived, eroded, and

transported to the continental margin (Grove et al., 2003; Jacobson et al., 2011). Figure 50 of Jacobson et al. (2011) illustrates the pre-San Andreas regional distribution of basement rock per age bin which is used for inference of source area in this discussion. In the studies by Grove et al. (2003) and Jacobson et al. (2011), the authors identified sources for each of the detrital zircon age populations contained in schist samples and samples from sedimentary basins within their study area. Results showed that detrital zircon population signatures in the schists mirror those in the sedimentary basins, and that the zircon populations of the samples show a transition through time whereby outboard sources of detrital zircons nearer the continental margin gradually give way to more inboard sources of detrital zircons in schist exposures. “Outboard” versus “inboard” sources refers to the progression of arc magmatism continent-ward, as subduction of the Farallon slab transitioned to flat subduction (Figure 5). This resulted in the Sierran-Peninsular Ranges Arc, which is comprised from west to east, of the early Cretaceous batholith (100–135 Ma) and the late Cretaceous batholith (85–100 Ma), followed by latest Cretaceous plutons (70–85 Ma) within the largely Proterozoic pre-Cretaceous crust. In this model, the Sierran-Peninsular Ranges Arc formed a continuous barrier that blocked the transport of eroded material from the Mojave block and San Gabriel source rocks (70–85 Ma and >300 Ma) from reaching the continental margin until the Nacimiento fault offset the arc sinistrally ca. 68–75 Ma, allowing inboard source detritus to make it to the continental margin (Jacobson et al. 2011; Figure 63). Another interpretation is that thrusting related to flat subduction uplifted the Sierran-Peninsular Ranges Arc and erosion resulted in breachment of the arc barrier (Saleeby, 2003). Regardless of the mechanism, the resulting increase of inboard material to the margin is

not disputed. Sharman et al. (2015) also found evidence that the Sierran-Peninsular Arc formed a topographic high that blocked inboard sources from reaching the margin in their study of forearc strata. They also concluded that a significant amount of inboard detritus made its way to the continental margin approximately 75–72 Ma.

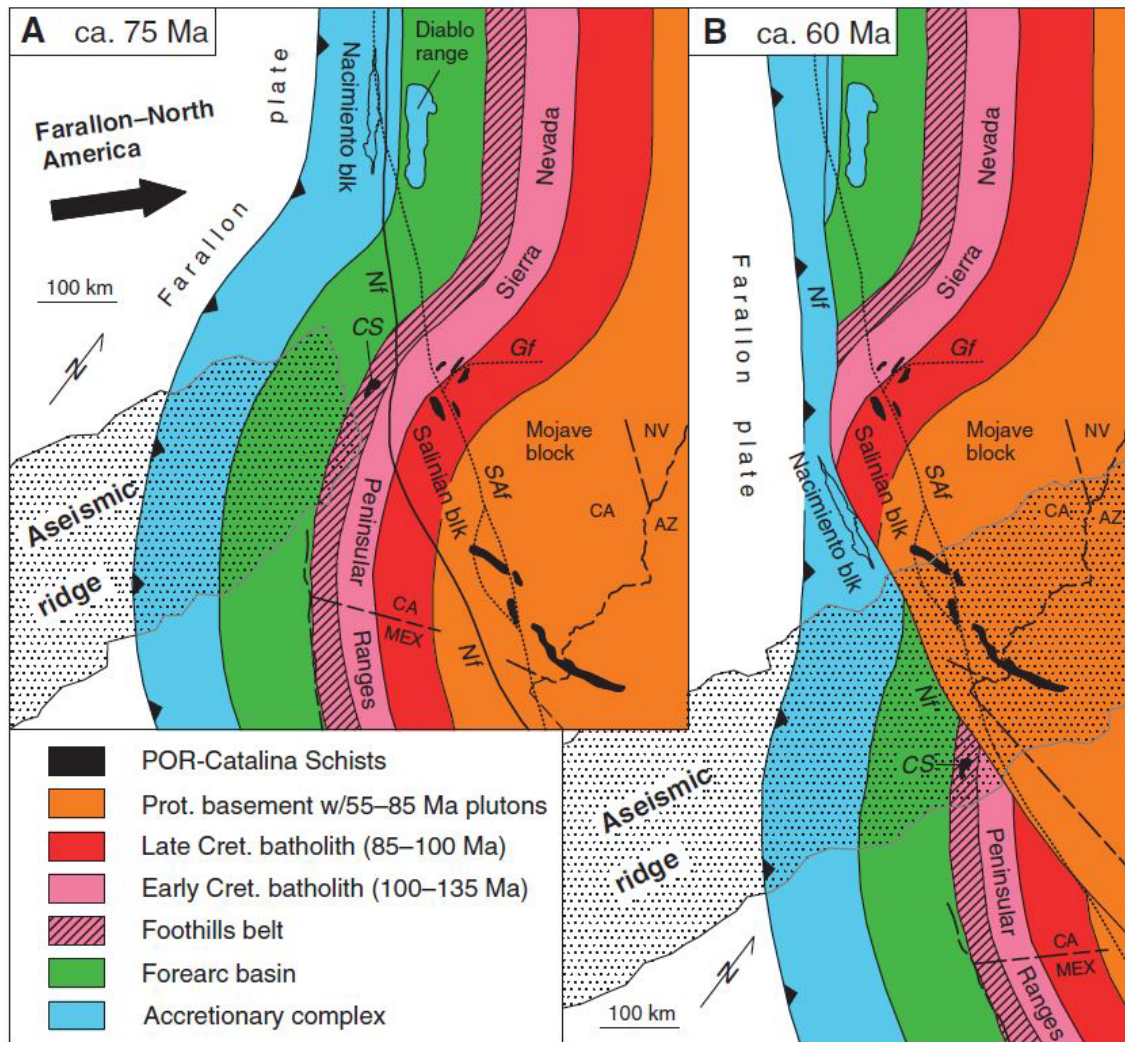


Figure 63. Diagram showing the Sierran-Peninsular Ranges Arc (left) as a topographic high and the offset of the arc barrier by the sinistral Nacimiento fault (right). Source: Jacobson et al. (2011).

The transition from outboard to inboard sources of detrital zircons spatially from NW to SE locations in Grove et al. (2003) and Jacobson et al. (2011), is striking. In

reviewing the data obtained in our study, one of the research questions I wish to answer is whether there is a change in detrital zircon provenance through time recorded up-section within the Blue Ridge schist.

When viewed from deep to shallow structural levels, several trends in detrital zircon provenance are observed in Sections 1 and 2. Detrital grains of latest Cretaceous age (70–85 Ma age bin) increase in both sections from deep to shallow structural levels (Figures 64 and 65) In Section 2, Proterozoic grains (>300 Ma age bin) also increase up-section. Note that grains in the >300 Ma age bin from Section 2 range in age from 873 to 2,483 Ma and are wholly Proterozoic in age. In Section 1, Proterozoic grains increase in abundance from the deepest sample (JNCM1947) to the middle sample (JNCM1942), but then decrease slightly in the structurally highest sample (BR218). Grains in the >300 Ma age bin from Section 1 range in age from 950 to 1,801 Ma and are also Proterozoic in age. Although there is an increasing trend in Proterozoic grains from deep to middle structural levels in Section 1 (samples from this study), the uppermost sample (BR218) does not support a continued increasing trend.

The most striking observation in the data is that the two basal samples (JNCM1947 and JN2056) from Sections 1 and 2, are dominated by late Cretaceous (85–100 Ma) and early Cretaceous (100–135 Ma) grains but are entirely devoid of latest Cretaceous (70–85 Ma) grains. The Proterozoic component is only 7% in JNCM1947 and 5% in JN2056, and there is also a small component of earliest Cretaceous to Jurassic grains (135–300 Ma age bin) in sample JNCM1947. This signature is interpreted to represent the erosion of the fore-arc crust, the Sierran-Peninsular Ranges Arc, and Proterozoic wall rock following the interpretation of Jacobson et al. (2011). Further, this

interpretation more simply reflects the erosion of the Sierran-Peninsular Ranges Arc and topographic high, prior to its dissection or “breachment” as termed by Saleeby (2003).

In contrast, the mid-section samples (JNCM1942 and JNCM1943) show the first appearance of latest Cretaceous grains (70-85 Ma) and an increase in Proterozoic grains (>300 Ma). Of important note is that these samples, although from different structural sections, are statistically identical in age (JNCM1942 = 81.8 Ma and JNCM1943 = 81.7 Ma) and therefore provide redundancy in interpretation of the grain percentages. Both samples show high percentages of Sierran-Peninsular Range age grains (85–100 Ma and 100–135 Ma) and low percentages of latest Cretaceous and Proterozoic age grains (70–85 Ma and >300 Ma). This is interpreted to reflect an early stage in the transition from outboard to inboard sources.

The next sample up-section structurally from the mid-structural samples is BR218. This sample is relatively close in section to sample JNCM1942 and is dated to 79.0 Ma; 2.8 Ma later than JNCM1942. The detrital grain distribution is somewhat similar to the mid-structural samples in that there is still a high proportion of 85–100 Ma grains, but a greatly reduced proportion of 100-135 Ma grains. As stated previously, there is a slight increase in 70–85 Ma grains and a strong increase of earliest Cretaceous to Jurassic grains. The Proterozoic component decreases slightly, but this may be an artifact of the low number of analyses or that the Proterozoic component fluctuates.

The structurally highest sample, JN2060 is dated to 75.6 Ma and is 3.4 Ma younger than BR218. This sample is perhaps the most robust in that the sample yielded 72 grains and shows a greatly reduced Sierran-Peninsular Ranges Arc signature (85–100 Ma and 100–135 Ma) and greatly increased latest Cretaceous pluton signature (70–85

Ma). There are also increases in earliest Cretaceous to latest Permian (135 Ma–300 Ma) grains and Proterozoic (>300 Ma) grains. This is interpreted to reflect the widening of the breach in the Sierran-Peninsular Ranges Arc and increased detrital outflow from the inboard Mojave block and San Gabriel terrane. The highest percentage of detrital zircon grains in the sample belongs to the latest Cretaceous pluton sources (70–85 Ma).

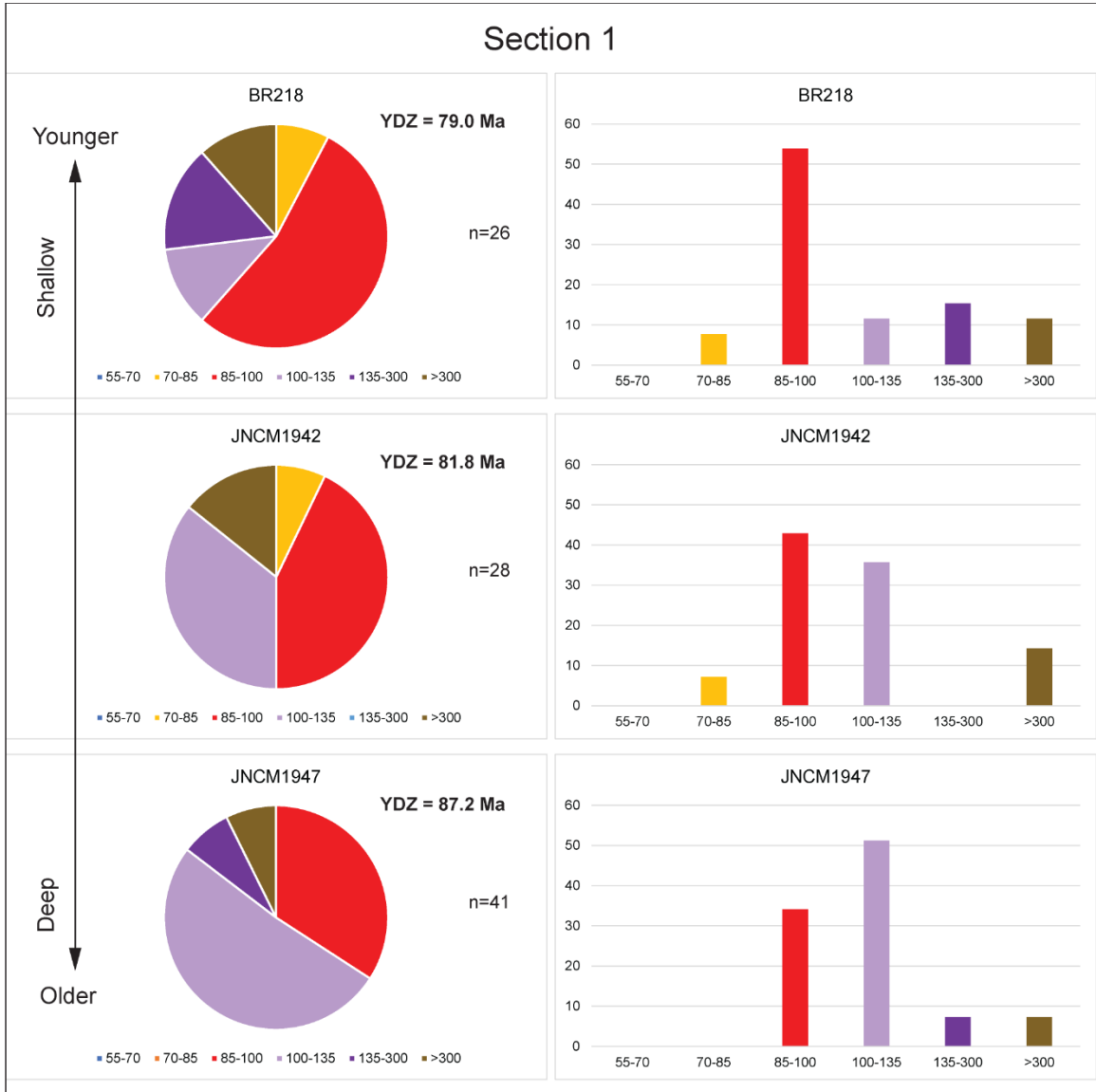


Figure 64. Section 1 detrital zircon grain populations as a function of YSG per structural level.

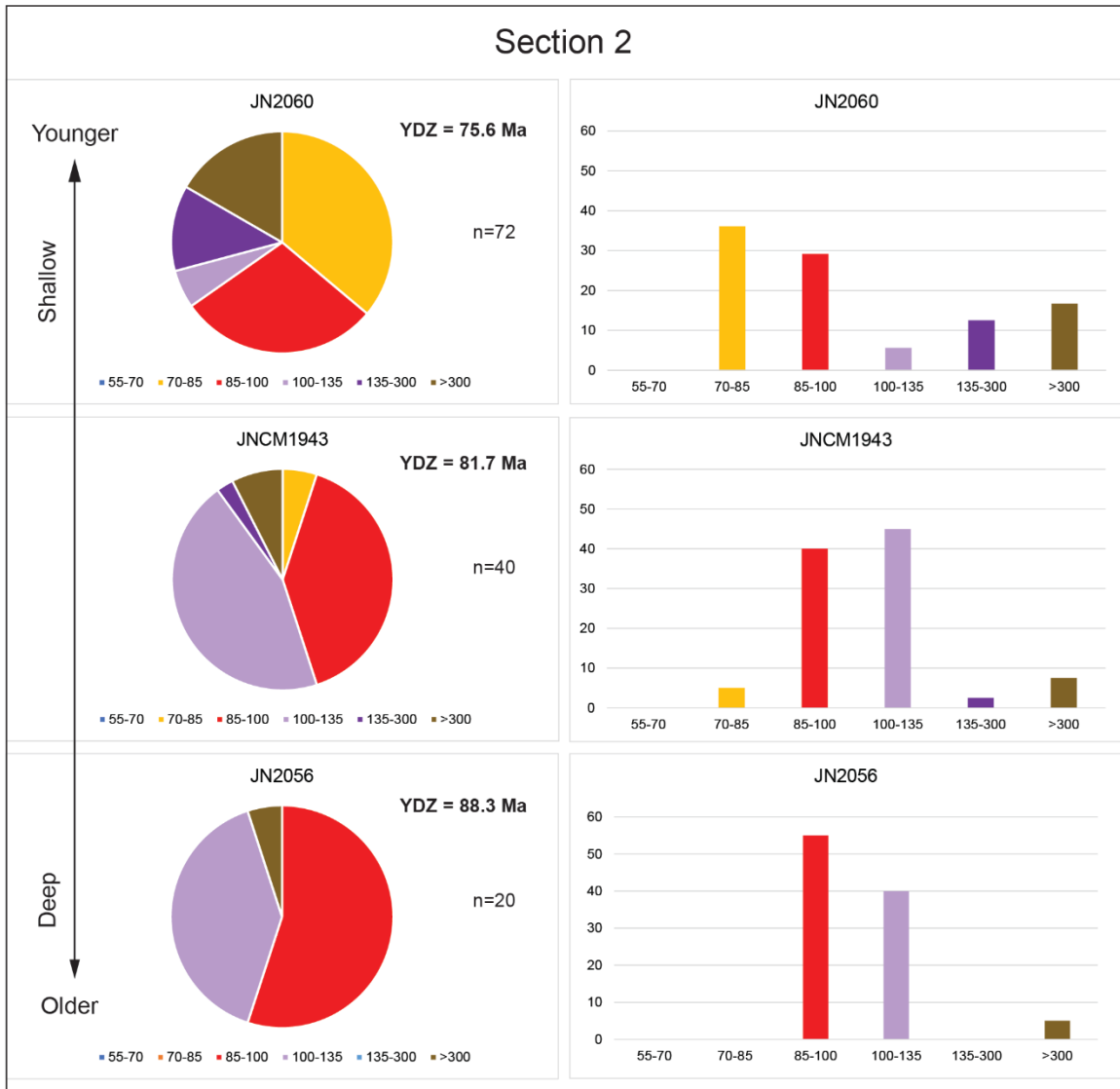
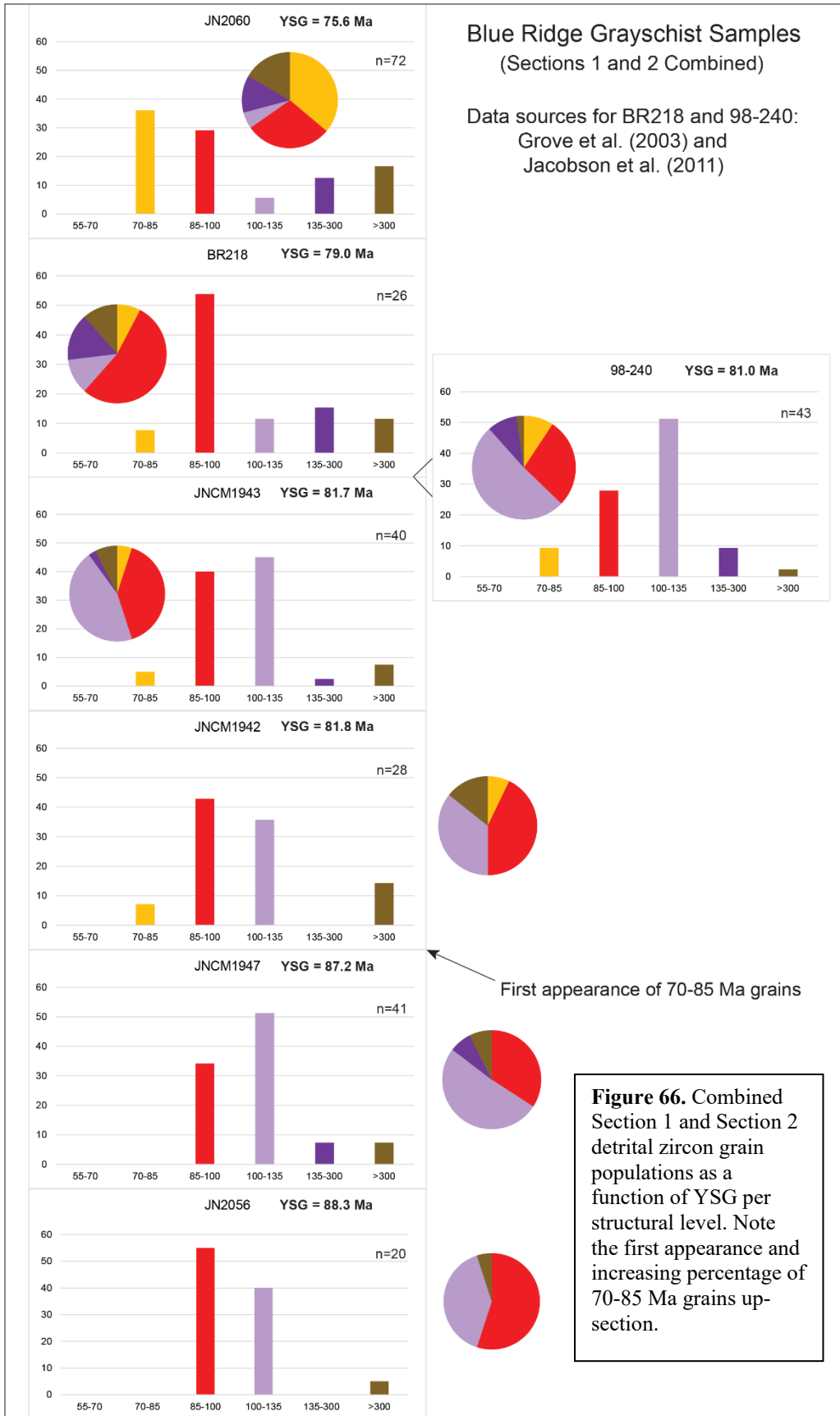


Figure 65. Section 2 detrital zircon grain populations as a function of YSG per structural level.

Because Sections 1 and 2 do appear to track the expected changes in provenance through time-up section, it is assumed here that the YSG age of each sample represents the relative stratigraphic position in section structurally. Therefore, Sections 1 and 2 were combined to show the overall sequential changes in zircon population distribution up section for the Blue Ridge schist body (Figure 66). Additionally, the second previously published sample 98-240 (Grove et al., 2003; Jacobson et al., 2011) from west Blue

Ridge is integrated into the section based on its YSG age of 81.0 Ma. The resulting section shows variable amounts of Proterozoic grains up section with the greatest concentration at 75.6 Ma. The 70–85 Ma grains generally increase up section with the greatest concentration also at 75.6 Ma.

The lack of more inboard sources of latest Cretaceous (70–85 Ma age bin) age grains in the basal samples and the first appearance of them in the mid-structural level/next youngest samples may bracket the initial stages of breachment of the Sierran-Peninsular Ranges Arc, and the opening of the corridor to source areas more inboard. The youngest single detrital grains (taken here to represent the upper limit of deposition for the structural level) for basal samples JN2056 (Sec 2) and JNCM1947 (Sec 1) are 88.3 Ma and 87.2 Ma respectively, and the YSG grains for samples JNCM1943 (Sec 2) and JNCM1942 (Sec 1) are 81.7 Ma and 81.8 Ma respectively. Based on the data obtained in this study, the initial transition from outboard to inboard sources would have occurred between 87.2 and 81.8 Ma, but as stated previously, the appearance of inboard source material in the mid-structural samples is interpreted to represent the early stages of the transition, so it is likely the transition occurred nearer 81.8 Ma than 87.2 Ma. Additionally, the transition is further constrained to 85 Ma by the 70–85 Ma age bin itself. The uppermost sample, JN2060 shows a marked increase of inboard source material at 75.6 Ma. This is consistent with the marked increases at 72–75 Ma reported by Grove et al. (2003) and Jacobson et al. (2011). However, the earlier first appearance of inboard source material near 82 Ma and the gradual increases up to 75.6 Ma is interpreted here to record the initial phase of breachment of the arc and the gradual increase of inboard source detritus as the breach widens.



Jacobson et al. (2011) reported the first appearance of material derived from sources east of the Sierran-Peninsular Arc (70–85 Ma and increases in >300 Ma) in several sedimentary basins in the central part of their study area by Campanian to early Maastrichtian time, but this is a broad age range (83.6–68 Ma). Given that the earliest age could be 83.6 Ma for the Campanian, the early transition to inboard source detritus in our samples at near 82 Ma is consistent with at least the inboard detritus making it into the trench and thus, the Blue Ridge protolith, much earlier than previously thought, at least for the central region of schist bodies represented by Blue Ridge.

Comparison with other Schist Bodies in the Pelona and Orocochia Mountains Groups

Figures 67–69 show grain population data per YSG per sample (i.e. temporal provenance changes through time) using published data (Jacobson et al., 2002, 2011; Grove et al., 2003; Sauer et al., 2019) for Mount Pinos, Sierra Pelona (Figure 67), Blue Ridge (Figure 68), East Fork, and Orocochia Mountains (Figure 69). Mount Pinos, Sierra Pelona, and Blue Ridge are old enough to preserve the first appearance of the 70–85 Ma population and associated increases. Also of note is the first appearance of Proterozoic grains in Mount Pinos and Sierra Pelona. This data may allow for the combined constraint on the first appearances of these grain populations (i.e. the initial breach of the arc). While not old enough to record the first appearance of inboard populations, East Fork and Orocochia Mountains do provide insight into temporal changes of the inboard populations and the relative similarity to Mount Pinos, Sierra Pelona, and Blue Ridge. Additionally, the Sierran-Peninsular Arc populations in all schist bodies show similar patterns that would be expected if erosion were progressing eastward.

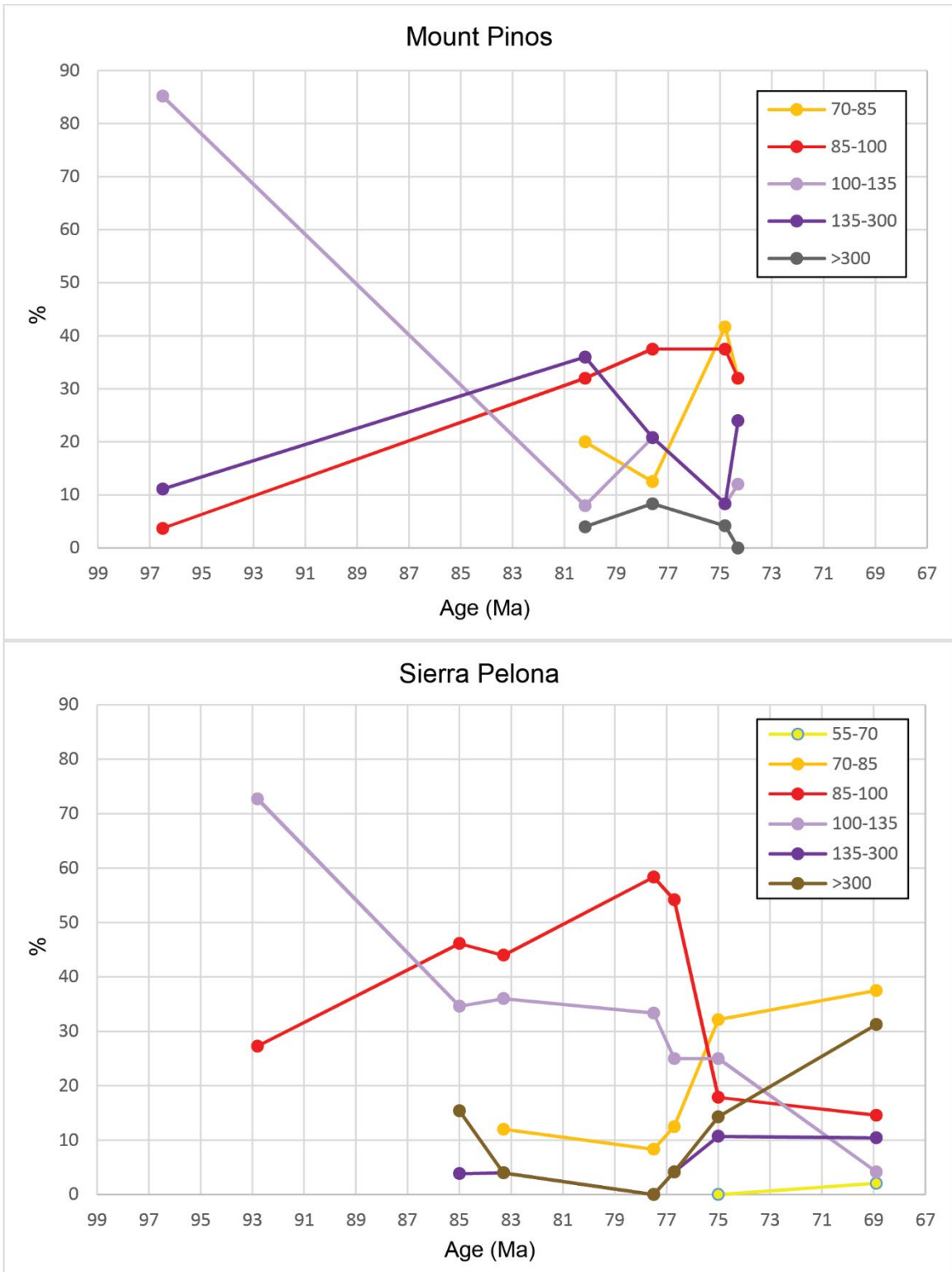


Figure 67. Plots showing grain population percentages plotted against YSG per sample for Mount Pinos and Sierra Pelona. The YSG ages are assumed to young up-section. Data sources: Jacobson et al. (2000, 2011) and Grove et al. (2003).

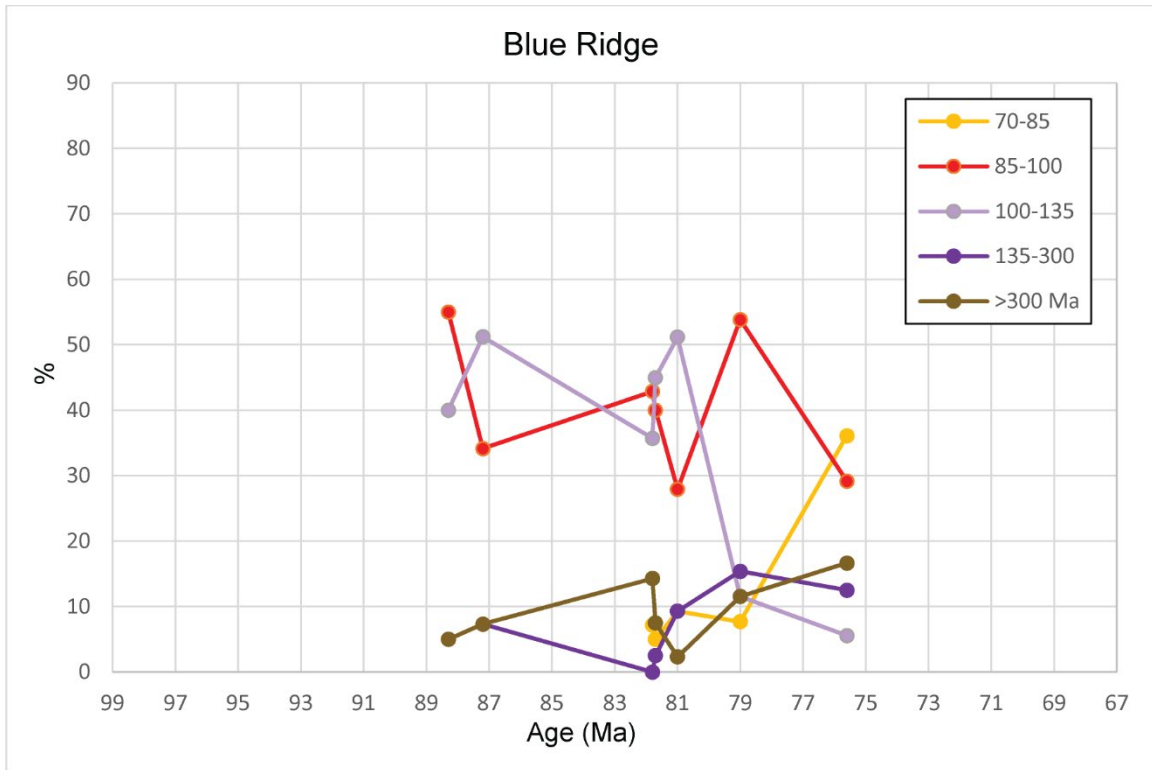


Figure 68. Plots showing grain population percentages plotted against YSG per sample for Blue Ridge. The YSG ages young up-section. Data sources for two samples (BR218 and 98-240): Grove et al., (2003) and Jacobson et al., (2011).

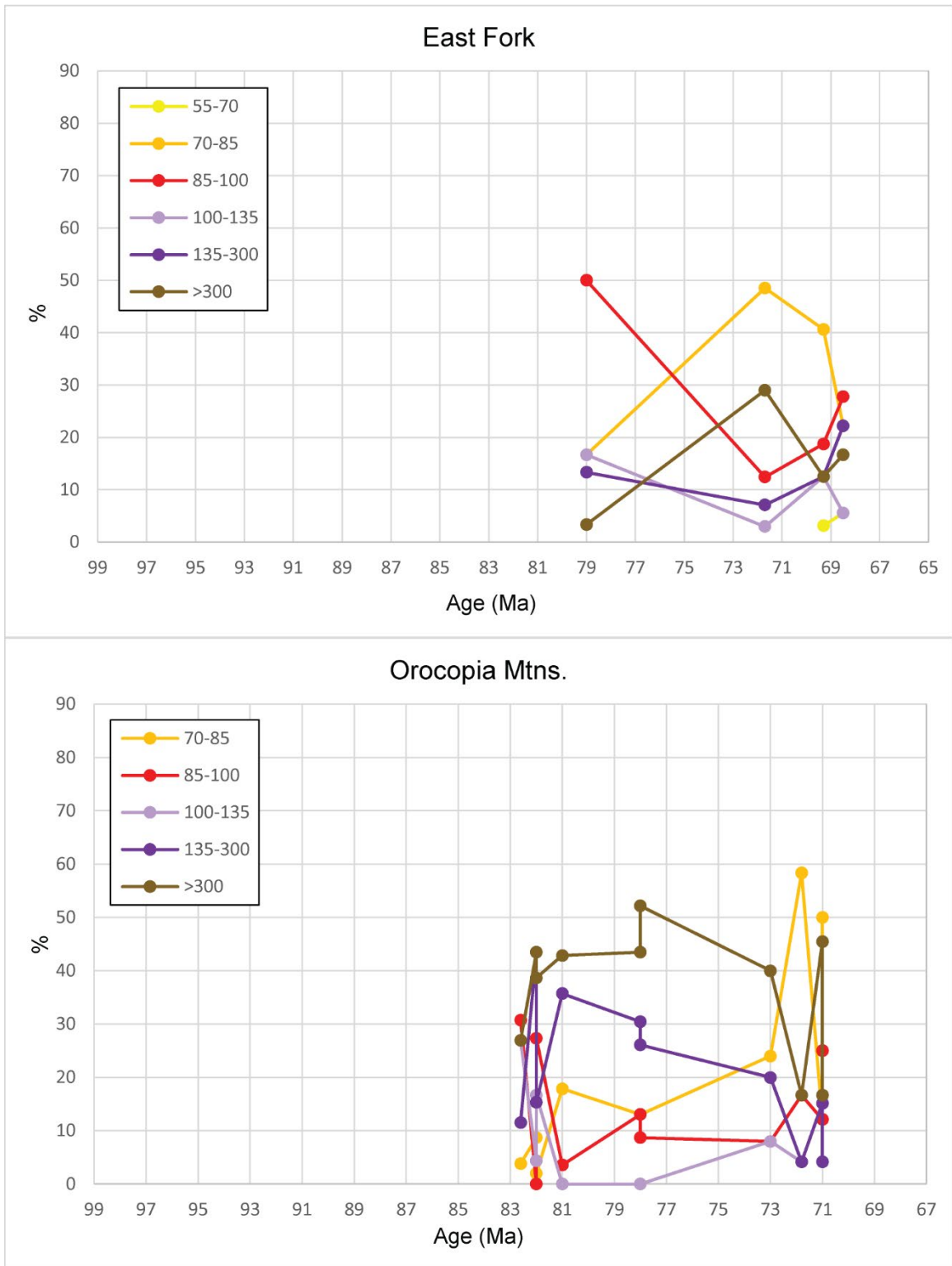


Figure 69. Grain population percentages plotted against YSG per sample for East Fork and Orocopia mountains. The YSG ages are assumed to young up-section. Data sources: Grove et al., (2003); Jacobson et al., (2011); Sauer et al., (2019).

Tracking Progressive Eastward Erosion from Outboard to Inboard Sources

Below are plots grouped by grain population percentage that reflects outboard to inboard source changes through time. The first plot, upper left, shows the temporal evolution of the outer Sierran-Peninsular Arc detritus (100-135 Ma) by schist body (Figure 70). From 97 Ma to 69 Ma the signature shows the progressive decrease in source material as the breach widens and erosion moves inboard. The next plot, bottom left of Figure 70 shows the inner Sierran-Peninsular Arc detritus (85-100 Ma) increasing as erosion moves inboard, then decreasing as the breach widens at 75 Ma. The next plot, Figure 70 (top right) shows the inner plutonic arc detritus (70-85 Ma) showing up at 83 Ma and increasing steadily to 71 Ma, reflecting the initial opening of the breach and progressive widening. The last plot, Figure 70 (bottom right), shows the Proterozoic component with a gradual increase, followed by a decrease, and then increase again for all schist bodies except Orocopia Mountains, which is quite different in signature.

Viewing the new Blue Ridge data and published data in this manner shows a compelling parallel to the known outboard to inboard transition of source detritus as the topographic barrier of the outer arcs is breached. This further strengthens the argument that the schist bodies may in fact preserve temporal transitions in provenance, if the YSG's per sample are interpreted to roughly reflect the age of deposition of the protolith.

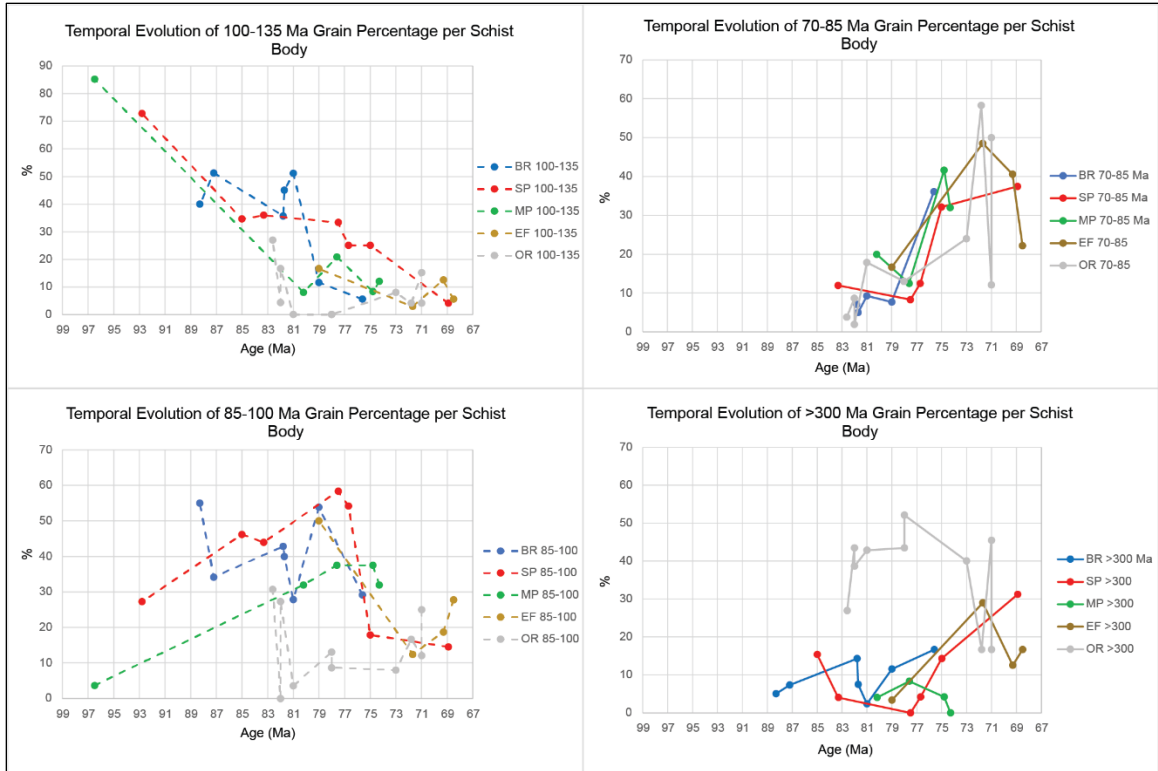


Figure 70. Plots of grain population percentage per schist body vs. YSG age per sample, showing the evolution of detritus population percentage per schist body over time. The pattern shows the eastward progression of outboard to inboard source detritus as erosion moves through the outer arcs to inner arc and inboard sources. Data sources: Jacobson et al. (2000, 2011); Grove et al. (2003); Sauer et al. (2019).

Constraining Initiation of the Breachment of the Sierran-Peninsular Ranges Arc

Figure 71 shows the YSG age per sample per schist body (i.e. the MDA of the structural level) for Mount Pinos, Sierra Pelona, Blue Ridge, and Orocopia Mountains on the left. To the right, the first appearance and last known absence of the grain populations (70–85 and >300 Ma) are plotted for each schist body. The gray bars denote the constrained area of uncertainty for the first appearance of the respective populations.

According to the data, initial breachment of the Sierran-Peninsular Ranges Arc occurred between 85 Ma and 83.3 Ma as indicated by the 70–85 Ma population. The first appearance of the > 300 ma population is less indicative since the source is probably sparse wall rock associated with the erosion of the arc itself.

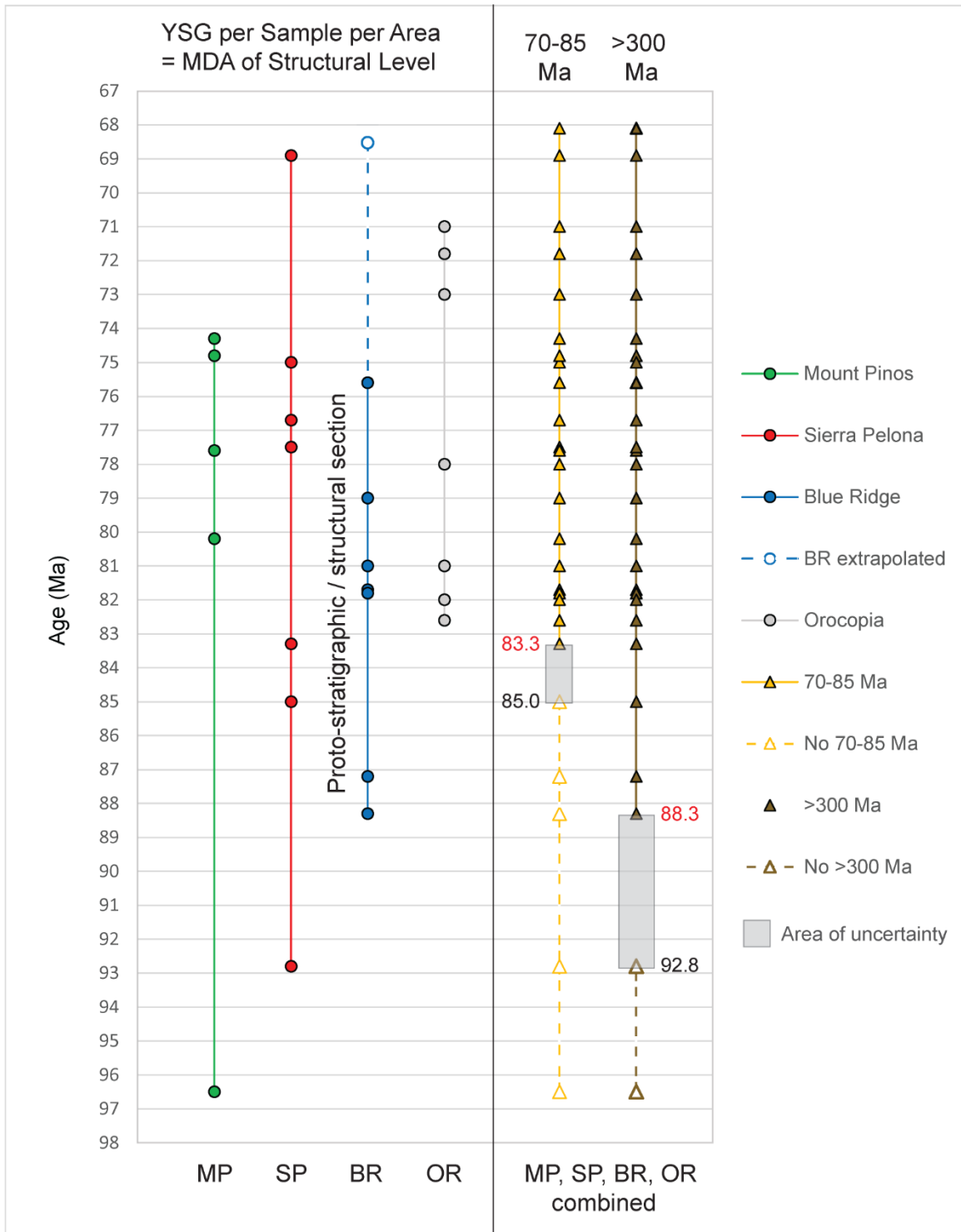


Figure 71. Composite plot showing all schist bodies mentioned in text as proto-stratigraphic/structural sections defined by YSG ages per sample (left). Note modeled upper section YSG for Blue Ridge. The right panel shows the first appearance ages for the 70-85 Ma and >300 Ma grain populations for all schist bodies. Collectively, the data constrain the area of uncertainty between the last age without the grain population and the first age with the stated population.

Tectonic Significance

The Pelona schist of Blue Ridge is strategically located to shed light on tectonic models related to evolution of the late Cenozoic transform boundary in southern California. Blue Ridge also preserves syn-metamorphic folds that inform on the mechanics of underthrusting of this ocean trench assemblage during the Late Cretaceous-early Paleogene Laramide orogeny. Below I address three relevant aspects of tectonic significance, all of which bear on intricate details of tectonic reconstruction:

Comparison to Schist Bodies West and East of the San Andreas Fault

As shown by Jacobson et al. (2011), probability density plots of detrital zircon analyses in conjunction with simple pie diagrams provide a convenient way to compare and contrast the detrital zircon provenances between separate bodies of Pelona-Orocopia-Rand schist. One theme of this current study is that Blue Ridge represented an extension of the Mt. Pinos and Sierra Pelona schist bodies prior to disruptions by the San Andreas fault system. Dr. Carl Jacobson graciously provided two unpublished plots that give context for the new Blue Ridge detrital zircon data. Figure 72 shows a provenance comparison between Blue Ridge and Sierra Pelona. This plot includes data from the 5 new Blue Ridge samples collected in this study, plus 2 samples from Angeles Crest Highway (BR 218 and 98-240; described earlier) and 7 samples from Sierra Pelona reported by Grove et al. (2003) and Jacobson et al. (2011). The cumulative probability density plots in particular show strong correlation between Blue Ridge and Sierra Pelona, with the exception of one Sierra Pelona sample (98-241) that contains a large proportion of 70-85 Ma and Proterozoic grains. Sample 98-241 has a YSG age of 69 Ma, which is significantly younger than the YSG from Blue Ridge (75.6 Ma) that was collected at a

mid-structural level. The data from sample 98-241 shows the significant increase of inboard detritus that would be expected up section at Sierra Pelona and Blue Ridge.

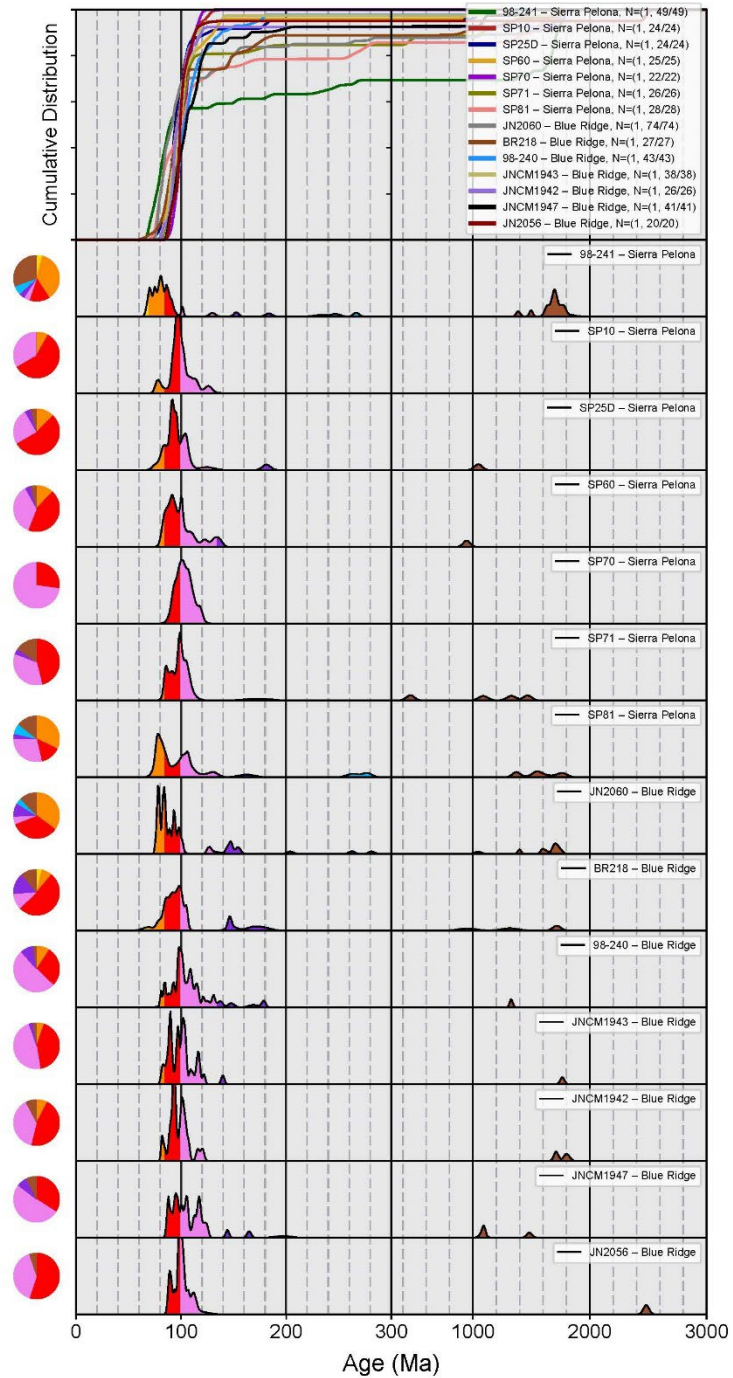


Figure 72. Comparison of detrital zircon results from individual samples collected in the Sierra Pelona and Blue Ridge schist bodies. Plot includes Blue Ridge data from the 5 new samples described in this study, and 2 samples collected previously from Angeles Crest Highway (Grove et al., 2003; Jacobson et al., 2011). Figure generated and kindly provided by Dr. Carl Jacobson using Detrital Py (Sharman et al., 2018).

A second Detrital Py plot provided by Carl Jacobson (Figure 73) shows a more regional comparison of the various Pelona-Orocopia schist bodies in southern California and southwestern Arizona. These areas include Mt. Pinos, Sierra Pelona, Blue Ridge, East Fork, Orocopia Mountains, Picacho Area, Castle Dome Mountains, Neversweat Ridge, and Cemetery Ridge. This plot illustrates the strong correlation between Mt. Pinos, Sierra Pelona, and Blue Ridge. Another feature accentuated by Figure 73 is the greater proportion of Proterozoic detritus in the east Fork block and all of the subareas east of the San Andreas fault. Most of these areas also display a significant Jurassic age mode. This pattern was detailed previously in the Provenance discussion section and appears to be driven by exhumation of a basement terrane east of the Sierra Nevada-Peninsular Ranges arc.

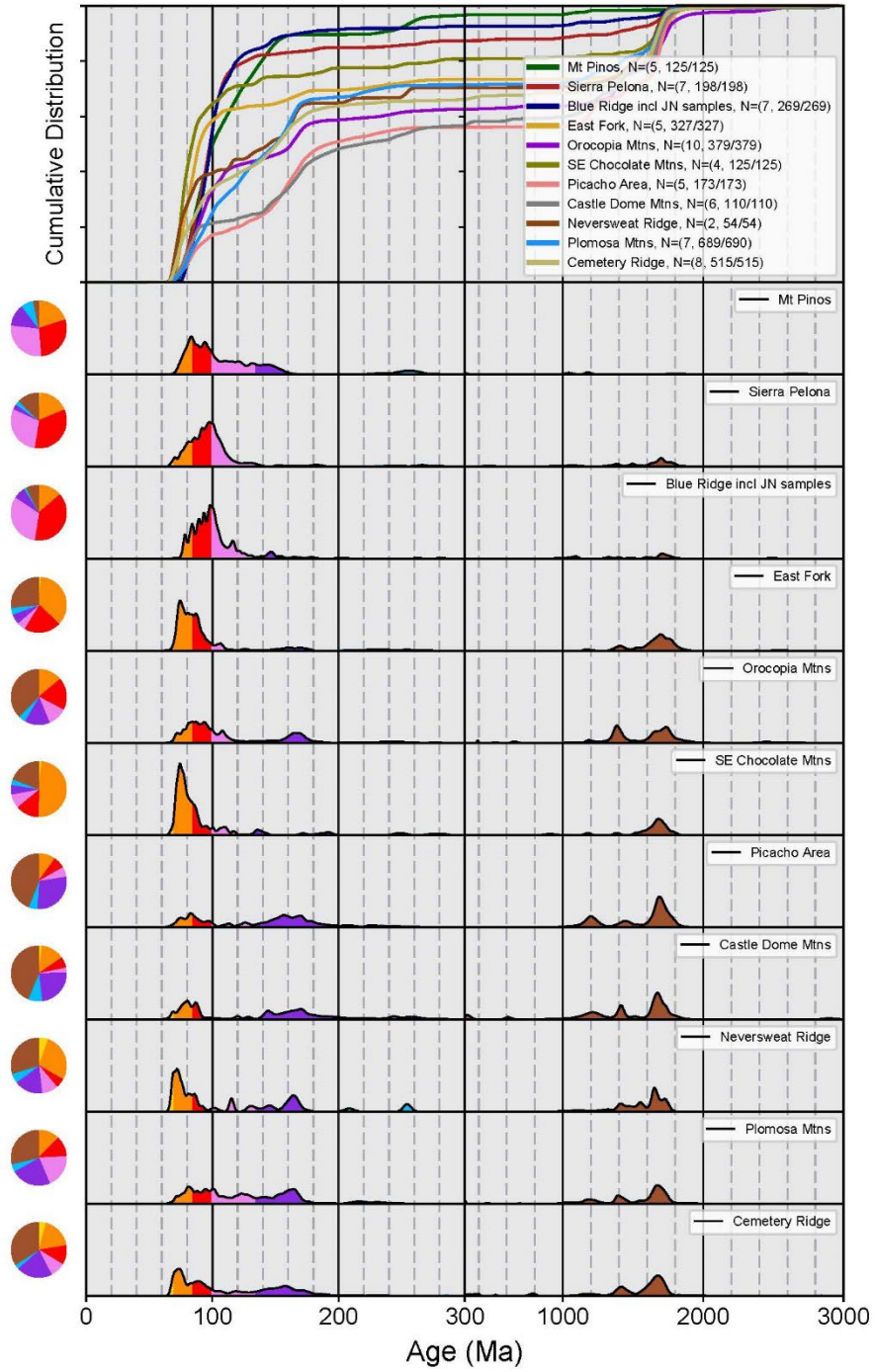


Figure 73. Comparison of detrital zircon results from distinct geographic subareas of Pelona-Orocopia schist in southern California and southwestern Arizona. Plot shows a compilation of all analyses from multiple samples studied from each subarea. Figure generated and kindly provided by Dr. Carl Jacobson using Detrital Py (Sharman et al., 2018).

Block Rotation During Late Cenozoic Transform Faulting

Multiple tectonic reconstructions involving various strands of the right-lateral San Andreas fault system have been proposed to explain the present-day distribution of schist bodies at Mt. Pinos, Sierra Pelona, Blue Ridge, and the Orocopia Mountains (Ehlig, 1975; Ehlig, 1982; Powell, 1993; Morton and Matti, 1993; Dillon and Ehlig, 1993; Nourse (2002). All of these reconstructions bring schists of the Orocopia Mountains and Chocolate Mountains in close proximity to the Sierra Pelona and East Fork block, respectively when approximately 240 km of San Andreas fault displacement is restored. Ehlig's models also use the San Gabriel fault to restore Mt. Pinos ~ 60 km to the west end of Sierra Pelona. Figure 74, clipped from Figure 5 of Ehlig (1982), shows these correlations.

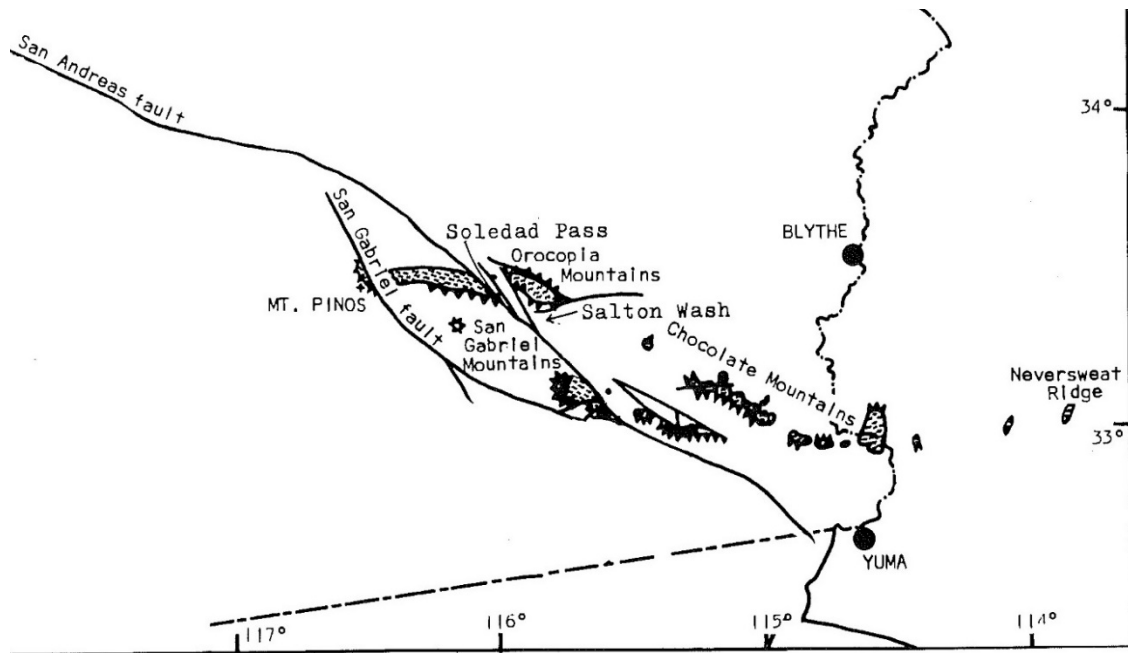


Figure 74. Palinspastic reconstruction of the Pelona and Orocopia schist bodies along the San Gabriel and San Andreas faults. This drawing is cropped from Figure 5 of Ehlig (1982). The present-day base map for this reconstruction is equivalent to Ehlig's Figure 2, presented earlier in the Introduction. The Blue Ridge block is not explicitly shown on this reconstruction, but it is on Figure 2.

A significant problem with most of the aforementioned reconstructions (with the exception of Powell, 1993) is they are entirely based on translations in which distinct marker units are restored along various right-lateral strike slip faults. These models do not account for block rotations that accompanied development of the transform plate boundary (Dokka and Travis, 1990; Luyendyk, 1991; Nicholson et al., 1994; Langenheim and Powell (2009), Darrin and Dorsey, 2013). There is an opportunity to use post–metamorphic map-scale folds present in most of the schist bodies as strain markers to track these rotations. A full treatment of related issues is presented in Coffee (2019). Below I take a simplified approach, using Dillon and Ehlig’s reconstruction of Figure 3 as a starting point.

Figure 75 shows the present-day orientations of post metamorphic folds mapped in various Pelona-Orocopia schist bodies on a palinspastic base in which displacements on the San Gabriel and San Andreas faults are restored. Mean trends of multiple folds measured in Blue Ridge, Sierra Pelona, Mt. Pinos, and the East Fork block are shown with a series of parallel red lines. A highly relevant area of focus is the proposed correlation between Mt Pinos, Sierra Pelona, and Blue Ridge (supported earlier by detrital zircon data). One preliminary observation is that Mt. Pinos has been rotated the wrong sense in Ehlig’s rendition of this map. Geological mapping by Kellogg (2013) shows that the Mt. Pinos schist body forms a south-dipping homocline, bounded on the south by an east-trending thrust fault. An east-trending antiform occurs in the northwest end of this exposure. When Mt. Pinos is restored 60km along the curved trace of the San Gabriel fault, these structures should rotate counterclockwise, achieving a west-southwest

orientation. This creates an alignment of the Mt. Pinos thrust and anticline with the Pelona fault and related folds in the Sierra Pelona.

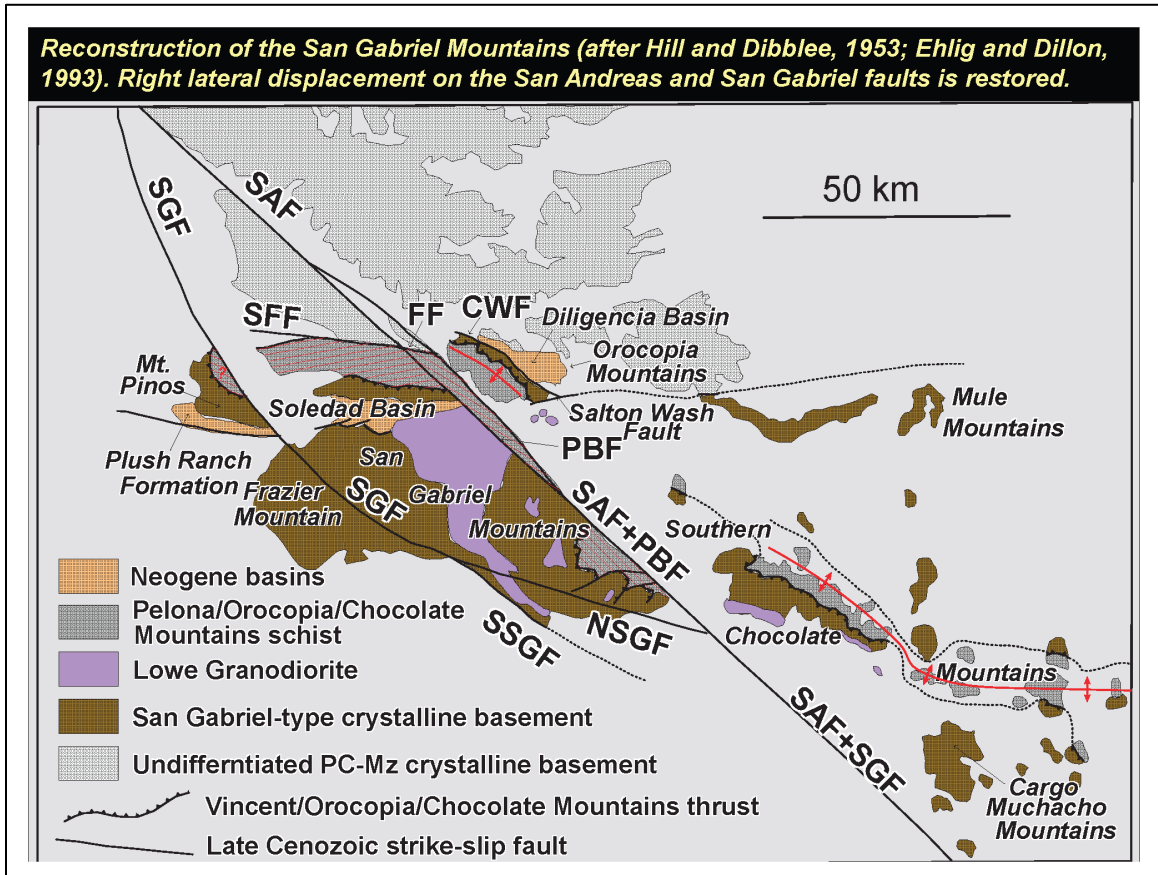


Figure 75. Widely cited reconstruction of Pelona-Orocopia schist bodies restored along the San Gabriel and San Andreas faults (Ehlig, 1982; Dillon and Ehlig, 1993). The Chocolate Mountains anticlinorium and Orocopia Mountains antiform are shown with bold red lines. Mean trends of multiple post-metamorphic map-scale folds from Mt. Pinos, Sierra Pelona, Blue Ridge, and East Fork block are shown with thin ruled red lines.

The reconstruction of Figure 75 accentuates misalignment of map scale post-metamorphic folds between Sierra Pelona and Blue Ridge. Sierra Pelona records a mean fold trend of ~S80W, whereas the average trend of a similar set of folds measured at Blue Ridge of N60W. This relationship implies that the Blue Ridge Block rotated 40 degrees

clockwise after formation of these folds. A convenient mechanism to accomplish this is block rotation between the right-lateral Punchbowl-San Jacinto and San Andreas faults that bound Blue Ridge on the southwest and northeast, respectively. This seems plausible, but when visualizing this process in map view a significant amount of NE-SW shortening must have accompanied the rotation of such a long, narrow fault block to accommodate the space problems. One solution to this dilemma is that the inferred shortening strain may be related to transpression of the San Gabriel block as it moved northwestward through the “Big Bend” in the San Andreas fault. A full treatment of this problem is however, beyond the scope of this study.

Another implication of the Blue Ridge rotation model proposed above is the timing of the post-metamorphic map-scale folding event. These folds are known to post-date metamorphism of the Pelona schist, dated in various places at 55-63 Ma (Jacobson et al., 2011) and are probably an extension of the Chocolate Mountains anticlinorium. Formation of the anticlinorium is thought to be associated with middle to late Cenozoic extension and is constrained to less than 24 Ma (Jacobson et al., 2002, 2007). The evidence presented above suggests that a west-southwest fold system developed across Mount Pinos, Sierra Pelona, and Blue Ridge prior to dextral disruption by the Punchbowl-San Jacinto and San Andreas faults. Hence, these folds would have developed no later than early Pliocene time.

Original Orientation of Laramide Compression at Blue Ridge

A clockwise rotation model for Blue Ridge is also helpful for reconciling the shortening direction deduced from fold hinges of syn-metamorphic folds with the inferred Laramide convergence direction between the Farallon and North American

plates. Removal of 40 degrees clockwise rotation brings the present-day orientations of the early-stage folds in much better alignment to regional tectonic driving forces.

As documented earlier, a subset of asymmetric tight folds with northerly hinges developed during Latest Cretaceous-early Paleogene metamorphism of the Blue Ridge schist. These folds are interpreted to be the result of subduction related shearing, with corresponding hinges indicating the direction of plate convergence and possibly channelized extrusion along the same path (Chapman, 2016). The key question is how to restore the E-W convergence direction recorded by present-day fold hinge orientations back to an orientation consistent with the direction of subduction. Arguments for clockwise rotation of post-metamorphic map scale folds were presented above.

Complicating the restoration is a need to account for 17 degrees of counterclockwise rotation that resulted from movement of the San Gabriel block through the Big Bend of the San Andreas fault during the past 5 Ma (Terres and Luyendyk, 1985; Liu, 1990; Ingersoll and Coffey, 2017; Coffey et al., 2019).

Structural observations from Ridge B show mixed Top-to-SW and Top-to-NE sense of shear with an average shortening direction of N78.5E/S78.5W. Ridge E shows uniform Top-to-SW sense of shear with compression direction S77.4W. However, considering that the Blue Ridge block now resides within the double restraining bend of the San Andreas fault (aka the Big Bend), a 17 counterclockwise deflection from the mean orientation of the SAF has been introduced that must be removed. This results in restored compression directions for Ridge B of S84.5E/N84.5W and N85.6W for Ridge E.

The convergence vector of the Farallon plate relative to North America has been reconstructed using fixed hot spot, global plate circuits, and mantle convection modeling to approximate the average N41E–N52E convergence vector between 67 Ma and 84 Ma (Dobrovine and Tarduno, 2008; Liu et al., 2008). Given the roughly W-E shear orientation of the syn-metamorphic folds on Blue Ridge (just mentioned), a clockwise block rotation of approximately 40-45 degrees is needed subsequent to Late Cretaceous-early Tertiary subduction to reconcile the outcrop-scale fold measurements. This requirement is achieved if one applies the 40 degrees clockwise rotation model presented in the previous section.

Summary

Results from Blue Ridge presented and discussed above show the importance of this isolated fault block for constraining the mechanics of Laramide convergent tectonics and Late Cenozoic transform plate boundary tectonic models in southern California. This study shows that marine trench protoliths of the Blue Ridge schist were deposited between 88.3 Ma and ~70 Ma, then deformed in a northeast-dipping subduction zone. Two generations of folds record syn-metamorphic Laramide subduction-related deformation likely followed by a clockwise block rotation of 40 degrees. Later, a period of open folding that predated development of the San Gabriel-San Andreas transform fault system occurred.

CONCLUSIONS

General Geology

- Subunits on Blue Ridge appear to be complexly interleaved or interbedded. Grayschist (quartzofeldspathic schist), greenschist (mafic schist), calc-silicates, and metacherts are randomly distributed throughout the structural sections that were mapped in detail. This contrasts with suppositions by some workers that metabasites should exist in the basal portions, followed by metacherts, calc-silicates, and grayschists in the upper portions (i.e. an intact sequence of oceanic plate, calcareous and siliceous muds, followed by sandstones and turbidites). It should be noted that detailed mapping was only conducted in basal to mid structural levels, but grayschist (sandstone and turbidite) is ubiquitous and interleaved or interbedded with all other subunits, even at these structural levels.
- Total measured structural thickness at TC-2 is 1,815 m, although this may not be the maximum exposed thickness of the Blue Ridge schist.

Thin Section Analysis

- Despite extensive analysis, there does not appear to be evidence qualitatively, for a systematic up-section variation in metamorphic grade. According to analyses of 56 thin sections, the majority of central Blue Ridge schist subunits were metamorphosed at lowermost amphibolite facies, or at the boundary between greenschist and amphibolite facies. This is consistent with previous analyses of mineralogical descriptions and ion microprobe analyses from Blue Ridge which

display albite-epidote-amphibolite facies (Jacobson, 1980; Grove et al., 2003; Jacobson et al., 2011).

Structure

- A subset of syn-metamorphic asymmetric folds in two locations appears to record shearing concomitant with subduction and extrusion of the schist body. One locality (Ridge B) records top-to-SW and top-to-NE sense of shear, and a second locality (Ridge E) records only top-to SW sense of shear after vertical axis rotations are performed. The resulting orientation restores to that of the convergence vector of the Farallon plate during the late Cretaceous if the Blue Ridge block is back rotated approximately 40–45 degrees.
- A subset of asymmetric folds exist as parasitic flexural slip folds in one studied location (Banded Fold Area) where they enclose larger map-scale folds with orientations of NNE.
- Two sets of map scale folds exist in the study area. 1) A syn-metamorphic tight folding event with northerly trending fold hinges demonstrates that the compression direction (maximum principal stress direction) associated with syn-metamorphic folding varies from N78E–S78W to N73W–S73E before vertical-axis rotation. Back rotation restores the compression directions to those of Laramide subduction related folding. 2) A younger post-metamorphic open group of folds with WNW trending fold axes demonstrates that the mean compression direction (maximum principal stress direction) associated with the formation of these folds was N29E–S29W before vertical-axis rotation. These folds are interpreted to be a continuation of the Chocolate Mountains anticlinorium which

is also expressed in schist bodies of Mt. Pinos and Sierra Pelona. Back rotation of the Blue Ridge block restores the trend of the anticlinorium with that of Sierra Pelona.

U-Pb Geochronology

- U-Pb geochronology results indicate that the Blue Ridge schist may be treated as a quasi-intact sedimentary sequence. Two independent structural sections (Sections 1 and 2) at near basal to mid structural levels, show that the schist body appears to preserve an intact proto-stratigraphy that displays a younging trend up-section. Combined maximum depositional ages, indicated by youngest single grain (YSG) analysis, range from 88.3 ± 2.6 Ma to 75.6 ± 1.2 Ma (2σ uncertainty) up-section.
- Age vs. depth relations for the structural sections show remarkable congruence between the YSG's per sample and relative depth measurements, possibly due to extreme flattening of the schist. These results potentially allow for the projection of age vs. depth models to portions of the schist which remain unsampled, as well as for the analysis of provenance changes through time.
- Although the youngest detrital zircon obtained and validated by this study yielded an age of 75.6 Ma, the structurally shallowest portion of the exposed schist of Blue Ridge was not directly sampled. Two linear regression models based on the projection of the composite sequence of Geochronology Section 1 onto two transects shows that the expected YSG for the shallowest portion of Blue Ridge should yield an average age of 68.5 Ma. However, this age may be too young if

additional unmapped folds exist within the transect which result in an upward stepping of the section.

- The resultant maximum depositional age for the Blue Ridge schist body (68.5 Ma) is consistent with that of the Sierra Pelona schist body which is characterized by a YSG age of 68.9 Ma.

Detrital Zircon Provenance

- Detrital zircon analysis shows that the Blue Ridge schist body is most similar in provenance signature to the Sierra Pelona schist body, followed closely by the Mount Pinos schist body, lending further support for the proposed connection of the three schist bodies in the past. In contrast, the Orocochia Mountains schist body is sufficiently different in provenance signature from the Blue Ridge, Sierra Pelona, and Mount Pinos schist bodies, to call into question a contiguous origin or similar depocenter between them.
- Blue Ridge detrital zircon samples also appear to record shifts in provenance occurring up-section through time that reflect the progressive evolution from outboard to inboard source detritus (i.e. the breaching of the Sierran-Peninsular Ranges Arc and allowance of detritus from the Mojave block and San Gabriel terrane to reach the continental margin) seen in forearc strata and pooled zircon data from the POR schists. In general, the sections show the progression of erosional detritus from dominantly the Sierran-Peninsular Ranges Arc at basal structural levels (88.3 Ma), followed by the first appearance of inboard detritus in the mid structural levels (81.8 Ma), and culminating with the marked increase of inboard detritus at the uppermost structural level (75.6 Ma). Assuming that the

other schist bodies also preserve relatively intact quasi-stratigraphic sections, evaluation of published data sets from Mount Pinos and Sierra Pelona schist bodies show similar provenance development through time (if the samples are defined by the youngest single grain and are assumed to roughly represent the maximum depositional age of the structural level). It is acknowledged however, that this interpretation of the data relies on several assumptions that are based on the Blue Ridge sections, and that the data from Blue Ridge is limited in terms of the number of samples (7) as well as the low number of analyses per sample (24–72 grains). Further work is needed to test this hypothesis.

Tectonic Significance

- This study shows that marine trench protoliths of the Blue Ridge schist were deposited between 88.3 Ma and approximately 75.6 Ma (minimum), then deformed in a northeast-dipping subduction zone. Two generations of folds record syn-metamorphic Laramide subduction-related deformation, followed by a period of open folding that predated development of the San Gabriel-San Andreas transform fault system. The present-day orientation of fold hinges on Blue Ridge reflects counterclockwise block rotation of ~17 degrees during development of the restraining double bend in the San Andreas fault, and clockwise block rotation of ~40–45 degrees that may be the result of transrotation between the Punchbowl and San Andreas faults.

REFERENCES

- Allmendinger, R.W., Cardozo, N., and Fisher, D., 2012, Structural geology algorithms: Vectors and tensors in structural geology: Cambridge, Cambridge University Press, 289 p.
- Barth, A.P., Wooden, J.L., Grove, M.G., Jacobson, C.E., and Pedrick, J.N., 2003, U-Pb zircon geochronology of rocks in the Salinas Valley region of California: A reevaluation of the crustal structure and origin of the Salinian block: *Geology*, v. 31, p. 517-520, doi: 10.1130/0091-7613(2003)031<0517:UZGORI>2.0.CO;2.
- Best, Myron G., 1982, Igneous and Metamorphic Petrology, W.H. Freeman & Company, New York, NY.
- Burchfiel, B.C., and Davis, G.A., 1981, Mojave Desert and environs, *in* Ernst, W.G., ed., *The Geotectonic Development of California (Rubey Volume I)*: Englewood Cliffs, New Jersey, Prentice-Hall, p. 217-252.
- Coffey, K. T., 2019, Tectonic Reconstruction of the Southern San Andreas Fault System Using Segments of the Chocolate Mountains Anticlinorium in the San Gabriel Mountains, Southern California, U.S.A. [Ph.D. thesis]: Los Angeles, University of California, 262 p.

- Coffey, K.T., Ingersoll, R.V., and Schmitt, A.K., 2019, Stratigraphy, provenance, and tectonic significance of the Punchbowl block, San Gabriel Mountains, California, USA: *Geosphere*, v. 15, no. 2, p. 479-501, <https://doi.org/10.1130/GES02025.1>.
- Crouch, J.K., and Suppe, J., 1993, Late Cenozoic tectonic evolution of the Los Angeles basin and inner California borderland: A model for core complex-like crustal extension: *Geological Society of America Bulletin*, v. 105, p. 1415-1434, doi: 10.1130/0016-7606(1993)105<1415:LCTEOT>2.3.CO;2.
- Crowell, J.C., 1962, Displacement along the San Andreas fault, California: Boulder, Colorado, Geological Society of America Special Paper 71, 61 p.
- Crowell, J.C., 1968, Movement histories of faults in the Transverse Ranges and speculations on the tectonic history of California, *in* Dickinson, W.R., and Grantz, A., eds., *Proceedings of Conference on Geologic Problems of San Andreas Fault System*: Stanford, California, Stanford University Publications in the Geological Sciences, v. 11, p. 323-341.
- Crowell, J.C., 1981, An outline of the tectonic history of southeastern California, *in* Ernst, W.G., ed., *The Geotectonic Development of California (Rubey Volume I)*: Englewood Cliffs, New Jersey, Prentice-Hall, p. 583-600.

Dawson, M.R., and Jacobson, C.E., 1989, Geochemistry and origin of mafic rocks from the Pelona, Orocoxia, and Rand Schists, southern California: *Earth and Planetary Science Letters*, v. 92, p. 371-385.

Dibblee, T.W., Jr., 1967, Areal geology of the western Mojave Desert, California: U.S. Geological Survey Professional Paper 522, 153 p.

Dibblee, T.W., Jr., 1968, Displacements on the San Andreas fault system in the San Gabriel, San Bernardino, and San Jacinto Mountains, southern California, *in* Dickinson, W.R., and Grantz, A., eds., *Proceedings of Conference on Geologic Problems of San Andreas Fault System*: Stanford, California, Stanford University Publications in the Geological Sciences, v. 11, p. 260-278.

Dibblee, T.W., Jr., 2002, Geologic Map of the Mount San Antonio Quadrangle, Los Angeles and San Bernardino Counties, California: Dibblee Geological Foundation Map DF-88, scale 1:24,000.

Dickinson, W.R., 1981, Plate tectonics and the continental margin of California, *in* Ernst, W.G., ed., *The Geotectonic Development of California (Rubey Volume I)*: Englewood Cliffs, New Jersey, Prentice-Hall, p. 1-28.

Dickinson, W.R., 1996, Kinematics of Transrotational Tectonism in the California

Transverse Ranges and its Contribution to Cumulative Slip along the San Andreas Transform Fault System: Geological Society of America Special Paper 305, 46 p

Dillon, J.T., and Ehlig, P.L., 1993, Displacement on the southern San Andreas fault, in Powell, R.E., et al., eds., The San Andreas fault system: Displacement, palinspastic reconstruction, and geologic evolution: Boulder, Colorado, Geological Society of America Memoir 178, p. 199-216.

Dillon, J.T., Haxel, G.B., and Tosdal, R.M., 1990, Structural evidence for northeastward movement on the Chocolate Mountains thrust, southeasternmost California: Journal of Geophysical Research, v. 95, p. 19953-19971.

Dobrovine, P.V., and Tarduno, J.A., 2008, A revised kinematic model for the relative motion between Pacific oceanic plates and North America since the Late Cretaceous: Journal of Geophysical Research, v. 113, B12101, <https://doi.org/10.1029/2008JB005585>

Ehlig, P.L., 1958, The geology of the Mount Baldy region of the San Gabriel Mountains, California, California [Ph.D. thesis]: Los Angeles, University of California, 195 p.

- Ehlig, P.L., 1968, Causes of distribution of Pelona, Rand, and Orocochia Schists along the San Andreas and Garlock faults, *in* Dickinson, W.R., and Grantz, A., eds., Proceedings of Conference on Geologic Problems of San Andreas Fault System: Stanford University Publications in the Geological Sciences, v. 11, p. 294-306.
- Ehlig, P.L., 1975, Basement rocks of the San Gabriel Mountains south of the San Andreas fault, southern California, in Crowell, J.C., ed., San Andreas fault in southern California: Sacramento, California, California Division of Mines and Geology Special Report 118, p.177-186.
- Ehlig, P.L., 1981, Origin and tectonic history of the basement terrane of the San Gabriel Mountains, central Transverse Ranges, *in* Ernst, W.G., ed., The geotectonic development of California (Rubey Volume I): Englewood Cliffs, New Jersey, Prentice Hall, p. 253- 283.
- Ehlig, P.L., 1982, The Vincent Thrust: Its Nature, Paleogeographic Reconstruction Across the San Andreas Fault, and Bearing on Evolution of the Transverse Ranges, in "Geology and Mineral Wealth of the Transverse Ranges," South Coast Geological Society, p. 370-379.
- Fritsche, A.E., Weigand, P.W., Colburn, I.P., and Harma, R.L., 2001, Transverse/Peninsular Ranges connections—Evidence for the incredible

Miocene rotation, *in* Dunne, G., and Cooper, J., compilers, *Geologic Excursions in Southwestern California: Los Angeles, Pacific Section, SEPM (Society for Sedimentary Geology)*, Book 89, p. 101-146.

Frost, E.G., Martin, D.L., and Krummenacher, D., 1982, Mid-Tertiary detachment faulting in southwestern Arizona and California and its overprint on the Vincent thrust system: *Geological Society of America Abstracts with Programs*, v. 14, no. 4, p. 164.

Graham, C. M., and England, P. C., 1976, Thermal regimes and metamorphism in the vicinity of overthrust faults: an example of shear heating and inverted metamorphic zonation from southern California, *Earth and Planetary Science Letters*, v. 31, p. 142-152.

Graham, C. M., and Powell, R., 1984, A garnet-hornblende geothermometer: calibration, testing, and application to the Pelona Schist, southern California, *Journal of Metamorphic Geology*, v. 2, p. 13-31.

Grove, M., Jacobson, C.E., Barth, A.P., and Vucic, A., 2003, Temporal and spatial trends of Late Cretaceous-early Tertiary underplating of Pelona and related schist beneath southern California and southwestern Arizona, *in* Johnson, S.E., Patterson, S.R., Fletcher, J.M., Girty, G.H., Kimbrough, D.L., and Martin-Barajas, A., eds., *Tectonic Evolution of Northwestern Mexico and the*

Southwestern USA: Geological Society of America Special Paper 374, p. 381-406.

Grove, M., Bebout, G.E., Jacobson, C.E., Barth, A.P., Kimbrough, D.L., King, R.L., Zou, H., Lovera, O.M., Mahoney, B.J., and Gehrels, G.G., 2008, The Catalina Schist: Evidence for middle Cretaceous subduction erosion of southwestern North America, in Draut, A.E., Clift, P.D., and Scholl, D.W., eds., Formation and Applications of the Sedimentary Record in Arc Collision Zones: Geological Society of America Special Paper 436, p.335-362.

Hamilton, W., 1988, Tectonic setting and variations with depth of some Cretaceous and Cenozoic structural and magmatic systems of the western United States, Economic Paleontologists and Mineralogists Pacific Section Pacific Coast Paleogeography Symposium 2, p. 453-469.

Haxel, G.B., and Dillon, J.T., 1978, The Pelona-Orocopia Schist and Vincent-Chocolate Mountain thrust system, southern California, in Howell, D.G., and McDougall, K.A., eds., Mesozoic paleogeography of the western United States: Los Angeles, Society of Economic Paleontologists and Mineralogists Pacific Section Pacific Coast Paleogeography Symposium 2, p. 453-469.

Haxel, G.B., Budahn, J.R., Fries, T.L., King, B.W., White, L.D., and Aruscavage, P.J., 1987, Geochemistry of the Orocopia Schist, southeastern California:

Summary, *in* Dickinson, W.R., and Klute, M.A., eds., Mesozoic rocks of southern Arizona and adjacent areas: Arizona Geological Society Digest, v. 18, p. 49-64.

Haxel, G.B, Jacobson, C.E., Richard, S.M., Tosdal, R.M., and Grubensky, M.J., 2002, The Orocochia Schist in southwest Arizona: Early Tertiary oceanic rocks trapped or transported far inland, *in* Barth, A.P., ed., Contributions to crustal evolution of the southwestern United States: Boulder, Colorado, Geological Society of America SpecialPaper 365, p. 99-128.

Hernandez, J. L., 2013, Preliminary geologic map of the Ritter Ridge 7.5 minute quadrangle, Los Angeles County, California: A digital data base, California Geological Survey.

Hernandez, J. L., and Olson, B. P. E., 2013, Preliminary geologic map of the Sleepy Valley 7.5 minute quadrangle, Los Angeles County, California: A digital data base, California Geological Survey.

Hill, M.L., and Dibblee, T.W., Jr., 1953, San Andreas, Garlock, and Big Pine faults, California: A study of the character, history, and tectonic significance of their displacements: Geological Society of America Bulletin, v. 64, p. 443-458, [https:// doi .org /10 .1130/0016 -7606](https://doi.org/10.1130/0016-7606)

Ingersoll, R.V., and Coffey, K.T., 2017, Transrotation induced by crustal blocks moving through restraining double bends, with southern California examples: *The Journal of Geology*, v. 125, p. 551-559, <https://doi.org/10.1086/692654>

Jacobson, C. E., 1980, Deformation and metamorphism of the Pelona Schist beneath the Vincent thrust, San Gabriel Mountains, California [Ph.D. thesis]: Los Angeles, University of California, 231 p.

Jacobson, C. E., 1983a, Relationship of deformation and metamorphism of the Pelona schist to movement of the Vincent thrust, San Gabriel Mountains, California, *American Journal of Science*, v. 283, p. 587-604.

Jacobson, C. E., 1983b, Complex refolding history of the Pelona, Orocochia, and Rand Schists, southern California, *Geology*, v. 11, p. 583-586

Jacobson, C. E., 1983c, Structural Geology of the Pelona Schist and Vincent thrust, San Gabriel Mountains, California, *Geological Society of America Bulletin*, v. 94, p. 753-767.

Jacobson, C. E., 1990, the $^{40}\text{Ar}/^{39}\text{Ar}$ geochronology of the Pelona schist and related rocks, southern California, *Journal of Geophysical Research*, v. 95, p. 509-528.

Jacobson, C. E., 1995, Qualitative thermobarometry of inverted metamorphism in the

Pelona and Rand schists, southern California, using calciferous amphibole in mafic schist, *Journal of Metamorphic Geology*, v. 13, p. 79-92.

Jacobson, C.E., and Sorensen, S.S., 1986, Amphibole compositions and metamorphic history of the Rand Schist and the greenschist unit of the Catalina Schist, southern California: *Contributions to Mineralogy and Petrology*, v. 92, p. 308-315, doi: 10.1007/BF00572159.

Jacobson, C.E., Oyarzabal, F.R., and Haxel, G.B., 1996, Subduction and exhumation of the Pelona-Orocopia-Rand schists, southern California: *Geology*, v. 24, p. 547-550, doi:10.1130/0091-7613(1996)024<0547:SAEOTP>2.3.CO;2.

Jacobson, C.E., Barth, A.P., and Grove, Marty, 2000, Late Cretaceous protolith age and provenance of the Pelona and Orocopia Schists, southern California: Implications for the evolution of the Cordilleran margin: *Geology*, v. 28, no. 3, p. 219-222.

Jacobson, C.E., Grove, M., Stamp, M.M., Vucic, A., Oyarzabal, F.R., Haxel, G.B., Tosdal, R.M., and Sherrod, D.R., 2002, Exhumation history of the Orocopia Schist and related rocks in the Gavilan Hills area of southeasternmost California, *in* Barth, A., ed., *Contributions to Crustal Evolution of the Southwestern United States: Geological Society of America Special Paper 365*, p. 129-154.

Jacobson, C.E., Grove, M., Vucic, A., Pedrick, J.N., and Ebert, K.A., 2007, Exhumation of the Orocochia Schist and associated rocks of southeastern California: Relative roles of erosion, synsubduction tectonic denudation, and middle Cenozoic extension, *in* Cloos, M., Carlson, W.D., Gilbert, M.C., Liou, J.G., and Sorensen, S.S., eds., *Convergent Margin Terranes and Associated Regions: A Tribute to W.G. Ernst: Geological Society of America Special Paper 419*, p. 1-37.

Jacobson, C.E., Grove, M., Pedrick, J.N., Barth, A.P., Marsaglia, K.M., Gehrels, G.E., and Nourse, J.A., 2011, Late Cretaceous-early Cenozoic tectonic evolution of the southern California margin inferred from provenance of trench and forearc sediments: *GSA Bulletin*; v. 123; no. 3/4; p. 485-506; doi: 10.1130/B30238.1

Jacobson, C. E., Hourigan, J. K., Haxel, G. B., & Grove, M., 2017. Extreme latest Cretaceous–Paleogene low-angle subduction: Zircon ages from Orocochia Schist at Cemetery Ridge, southwestern Arizona, USA. *Geology*, v. 45, no. 10, p. 951-954.

James, E.W., and Mattinson, J.M., 1988, Metamorphic history of the Salinian block: An isotopic reconnaissance, *in* Ernst, W.G., ed., *Metamorphism and crustal evolution of the western United States (Rubey Vol. VII)*: Englewood Cliffs, New Jersey, Prentice Hall, p. 938- 952.

Kidder, S., and Ducea, M.N., 2006, High temperatures and inverted metamorphism in

the schist of Sierra de Salinas, California: *Earth and Planetary Science Letters*, v. 241, p. 422-437, doi: 10.1016/j.epsl.2005.11.037.

Liu, W., 1990, Paleomagnetism of Miocene sedimentary rocks in the Transverse Ranges: the implications for tectonic history [Ph.D. thesis]: Pasadena, California Institute of Technology, 233 p.

Ludwig KR. 2012. User's Manual for Isoplot 4.5: A Geochronological Toolkit for Microsoft Excel. Berkeley Geochronological Center Special Publication, 4: 25-32.

Luyendyk, B.P., Kamerling, M.J., Terres, R.R., and Hornafius, J.S., 1985, Simple shear of southern California during Neogene time suggested by paleomagnetic declinations: *Journal of Geophysical Research*, v. 90, p. 12,454-12,466, doi: 10.1029/JB090iB14p12454.

Malin, P.E., Goodman, E.D., Henyey, T.L., Li, Y.G., Okaya, D.A., and Saleeby, J.B., 1995, Significance of seismic reflections beneath a tilted exposure of deep continental crust, Tehachapi Mountains, California: *Journal of Geophysical Research*, v. 100, p. 2069- 2087, doi: 10.1029/94JB02127.

May, D.J., 1989, Late Cretaceous intraarc thrusting in southern California: *Tectonics*, v. 8, p.1159-1173, doi: 10.1029/ TC008i006p01159.

Morton, D.M. and Miller, F.K., 2003. Preliminary geologic map of the San Bernardino 30'x 60'quadrangle, California (includes preliminary GIS database) (No. 2003-293). US Geological Survey.

Muehlberger, W. M., and Hill, H. S., 1958, Geology of the central Sierra Pelona, Los Angeles County, California, *American Journal of Science*, v. 256, p. 630-643.

Nicholson, C., Sorlien, C.C., Atwater, T., Crowell, J.C., and Luyendyk, B.P., 1994, Microplatecapture, rotation of the western Transverse Ranges, and initiation of the San Andreas transform system as a low-angle fault system: *Geology*, v. 22, p. 491-495, doi: 10.1130/0091-7613(1994)022<0491:MCROTW> 2.3.CO;2.

Nourse, J.A., 2002, Middle Miocene reconstruction of the central and eastern San Gabriel Mountains, southern California, with implications for evolution of the San Gabriel fault and Los Angeles basin, in Barth, A., ed., *Contributions to Crustal Evolution of the Southwestern United States*: Boulder, Colorado, Geological Society of America Special Paper 365, p. 161-185.

Petit, J.P., 1987, Criteria for the sense of movement on fault surfaces in brittle rocks; *Journal of Structural Geology*, Vol. 9, No. 5/6, pp. 597 to 608.

Platt, J.P., 1976, *The Petrology, Structure, and Geologic History of the Catalina Schist Terrain, Southern California*: University of California Publications in

Geological Sciences, v. 112, 111 p.

Powell, R.E., 1993, Balanced palinspastic reconstruction of pre-late Cenozoic paleogeology, southern California, *in* Powell, R.E., Weldon, R.J., and Matti, J.C., eds., *The San Andreas Fault System: Displacement, Palinspastic Reconstruction, and Geologic Evolution*: Geological Society of America Memoir 178, p. 1-106.

Saleeby, J., 2003, Segmentation of the Laramide slab—Evidence from the southern Sierra Nevada region: *Geological Society of America Bulletin*, v. 115, p. 655-668, doi: 10.1130/0016-7606(2003)115<0655:SOTLSF>2.0.CO;2

Saleeby, J., Farley, K.A., Kistler, R.W., and Fleck, R., 2007, Thermal evolution and exhumation of deep-level batholithic exposures, southernmost Sierra Nevada, California, *in* Cloos, M., Carlson, W.D., Gilbert, M.C., Liou, J.G., and Sorensen, S.S., eds., *Convergent Margin Terranes and Associated Regions: A Tribute to W.G. Ernst*: Geological Society of America Special Paper 419, p. 39-66, doi: 10.1130/2006.2419(01).

Sauer, K.B., et al., 2019, Deep-crustal metasedimentary rocks support Late Cretaceous “Mojave-BC” translation: *Geology*, v. 47, p. 99–102, <https://doi.org/10.1130/G45554.1>.

- Seymour, N.M., Strickland, E.D., Singleton, J.S., Stockli, D.F., and Wong, M.S., 2018, Laramide subduction and metamorphism of the Orocopia Schist, northern Plomosa Mountains, west-central Arizona: Insights from zircon U-Pb geochronology: *Geology*, v. 46, p. 847–850, <https://doi.org/10.1130/G45059.1>
- Sharman, G.R., Graham, S.A., Grove, M., Kimbrough, D.L. and Wright, J.E., 2015. Detrital zircon provenance of the Late Cretaceous–Eocene California forearc: Influence of Laramide low-angle subduction on sediment dispersal and paleogeography. *Bulletin*, 127(1-2), pp.38-60.
- Sharman, G.R., Sharman, J.P. and Sylvester, Z., 2018. detritalPy: A Python-based toolset for visualizing and analysing detrital geo-thermochronologic data. *The Depositional Record*, 4(2), pp.202-215.
- Terres, R.R., and Luyendyk, B.P., 1985, Neogene tectonic rotation of the San Gabriel region, California, suggested by paleomagnetic vectors: *Journal of Geophysical Research*, v. 90, p. 12467-12484, <https://doi.org/10.1029/JB090iB14p12467>
- Williams, H., Turner, F., and Gilbert, C., 1972, Petrography: An Introduction to Study of Rocks in Thin Section, 2nd edition, W.H. Freeman & Company, New York, NY.
- Wood, D.J., and Saleeby, J.B., 1997, Late Cretaceous- Paleocene extensional collapse and disaggregation of the southernmost Sierra Nevada batholith:

International Geology Review, v. 39, p. 973-1009, doi:
10.1080/00206819709465314.

Woodford, A.O., 1960, Bedrock patterns and strike-slip faulting in southwestern
California: American Journal of Science, v. 258-A, p. 400-417.

Yin, A., 2002, Passive-roof thrust model for the emplacement of the Pelona-Orocopia
Schist in southern California, United States: Geology, v. 30, p. 183-186, doi:
10.1130/0091-7613(2002)030<0183:PRTMFT>2.0.CO;2.

APPENDIX A

Plate 1: Geologic Map of Central Blue Ridge

APPENDIX B

Plate 2: Cross-Sections of Central Blue Ridge

JN2060 31	407.1	2.2	0.099328	0.003158	0.014601	0.000331	68.77	1.63	0.04911	0.00139	0.49	95.3	1.2	93.1	1.1	152	33	93	1.1	39	1.1	39	1.1	-13299900	2	
JN2060 69	519.0	1.6	0.091279	0.002941	0.014594	0.000289	0.215868747	68.74	1.44	0.04533	0.00158	0.22	88.3	1.5	93.1	1	0.0	30	93.3	1	39	1	-133142757	-5		
JN2060 65	693.8	2.4	0.090809	0.002143	0.014619	0.000332	0.695313272	68.67	1.55	0.04493	0.00082	0.70	87.7	0.7	93.2	1.1	0.0	20	93.5	1.1	39	93.5	1.1	-133142757	-6	
JN2060 20	440.1	2.2	0.094075	0.003161	0.014551	0.000323	0.337088838	68.52	1.67	0.04698	0.00154	0.44	91.7	1.4	93.4	1.1	47	39	93.4	1.1	47	39	93.4	1.1	-99	-2
JN2060 11	49.8	2.6	0.116648	0.011156	0.014859	0.000437	0.33827298	67.75	2.04	0.05611	0.000504	0.34	109.7	4.4	94.5	1.4	456	100	93.8	1.4	456	100	93.8	1.4	79	14
JN2060 39	73.7	0.8	0.112852	0.009633	0.014876	0.000466	0.183657088	67.73	2.16	0.05447	0.000528	-0.18	106.7	5.4	94.5	1.5	389	109	93.9	1.5	389	109	93.9	1.5	76	11
JN2060 38	418.4	1.6	0.096884	0.006637	0.014881	0.000466	0.279997827	67.52	2.18	0.04944	0.000528	0.67	106.7	5.4	94.5	1.5	389	109	93.9	1.5	389	109	93.9	1.5	76	11
JN2060 13	922.9	1.9	0.1438	0.052965	0.014966	0.001303	0.96909512	66.58	5.46	0.05764	0.000955	0.97	114.4	4.8	96.1	3.9	515	182	95.2	3.8	81	81	95.2	3.8	81	16
JN2060 3	494.7	1.7	0.103768	0.004402	0.015113	0.000454	0.496618402	66.63	2.07	0.04946	0.000220	0.50	98.9	1.9	96.1	3.9	515	182	95.2	3.8	81	81	95.2	3.8	81	16
JN2060 19	945.2	7.6	0.523022	0.023347	0.023146	0.004709	0.463518643	64.45	8.07	0.132709	0.004489	0.86	356	34	104.4	7.5	2067	240	96.5	6.5	95	95	96.5	6.5	95	59
JN2060 55	255.0	1.5	0.087469	0.003791	0.015118	0.000262	0.224286008	66.02	1.13	0.04236	0.00184	0.22	86	1.8	96.9	3.2	672	60	97.4	0.8	40	40	97.4	0.8	-138428471	-13
JN2060 33	1523.8	8.5	0.139286	0.019074	0.016135	0.001793	0.897185329	64.43	4.20	0.06196	0.00348	0.90	126.4	1.7	99.3	3.2	672	60	97.4	0.8	40	40	97.4	0.8	-138428471	-13
JN2060 7	548.2	2.0	0.108225	0.003703	0.015438	0.000297	0.345668471	64.96	1.29	0.04976	0.00164	0.35	101.9	1.6	98.5	1	183	38	98.3	1	46	46	98.3	1	46	3
JN2060 23	735.0	12.2	0.110932	0.029764	0.01598	0.001658	0.008319706	64.90	5.14	0.04864	0.000558	0.01	99.8	6.6	98.6	3.9	129	135	98.5	3.9	24	24	98.5	3.9	24	1
JN2060 5	3605.0	31.9	0.10693	0.00308	0.015602	0.000467	0.795344687	64.50	1.82	0.04859	0.00091	0.80	100.3	0.8	99.2	1.4	127	22	99.1	1.4	22	22	99.1	1.4	22	1
JN2060 30	1934.6	3.7	0.103907	0.003588	0.015652	0.000568	0.764274986	64.51	2.23	0.04828	0.00121	0.76	99.7	1.1	99.2	1.7	112	30	99.1	1.7	11	11	99.1	1.7	11	1
JN2060 42	92.8	0.1	0.1661269	0.0244124	0.025223	0.002384	0.461565702	40.85	2.12	0.04229	0.000644	0.86	92.78	6.5	155.9	5.9	4060	52	99.9	2.4	96	96	99.9	2.4	96	82
JN2060 73	1070.2	3.4	0.103898	0.002194	0.015894	0.000302	0.152684986	65.09	1.21	0.04741	0.000123	0.15	100.1	1.4	101.4	1	69	31	101.4	1	47	47	101.4	1	47	-1
JN2060 47	235.1	2.4	0.122243	0.005079	0.019722	0.00049	0.177240247	50.95	1.29	0.04617	0.000200	0.18	119.5	2.6	125.3	1.6	5.2	52.2	125.6	1.6	5.2	52.2	125.6	1.6	-2310	-5
JN2060 86	769.7	1.4	0.148867	0.003843	0.020216	0.00054	0.568413052	49.74	1.37	0.05268	0.00105	0.57	138.4	1.5	128.3	1.7	314	23	127.8	1.7	59	59	127.8	1.7	59	7
JN2060 29	261.3	3.2	0.133807	0.006691	0.021158	0.001014	0.755026022	48.14	2.47	0.04613	0.00155	0.76	125.9	2	132.5	3.4	3.2	40.4	132.8	3.4	40.4	132.8	3.4	-4041	-5	
JN2060 44	2117.6	2.6	0.236604	0.006947	0.021754	0.000602	0.744206466	46.25	1.21	0.04463	0.00157	0.74	102.4	1.7	137.9	1.9	1041	21	144.7	1.6	87	87	144.7	1.6	87	22
JN2060 75	505.6	0.6	0.155715	0.005564	0.022617	0.000506	0.462059829	44.38	0.97	0.04982	0.00161	0.46	146.1	2	143.7	1.6	186	38	143.5	1.6	33	33	143.5	1.6	33	2
JN2060 25	82.1	2.0	0.152551	0.009901	0.023047	0.000526	0.163619188	43.57	1.01	0.04883	0.00322	0.16	144.7	4.5	146.3	1.7	119	78	146.4	1.7	78	78	146.4	1.7	78	-1
JN2060 78	169.9	0.6	0.187581	0.014698	0.023458	0.000659	0.702144074	42.87	1.16	0.05739	0.00346	0.70	171.9	3.6	148.6	2	506	66	147.5	2	71	71	147.5	2	71	14
JN2060 57	172.7	0.3	0.145833	0.007422	0.023034	0.000408	0.215516476	43.29	0.88	0.04610	0.00235	0.22	139	3.3	147.2	1.5	1.6	61.4	147.6	1.5	9100	9100	147.6	1.5	9100	-6
JN2060 45	325.0	1.7	0.165191	0.015368	0.024946	0.002133	0.939508876	42.69	4.15	0.04883	0.00161	0.94	148.6	4.6	149.3	7.2	139	39	149.3	7.2	7	7	149.3	7.2	7	0
JN2060 15	351.6	2.9	0.167039	0.005774	0.024142	0.000569	0.008526455	41.60	0.97	0.05017	0.00166	0.41	156.1	2.3	153.1	1.8	202	38	153	1.8	24	24	153	1.8	24	0
JN2060 37	103.0	0.4	0.161319	0.010099	0.024465	0.000547	0.28167904	41.03	0.94	0.04697	0.00289	0.28	148.7	4.1	155.2	1.8	46	73	155.5	1.8	46	73	155.5	1.8	46	-4
JN2060 17	136.1	2.0	0.162343	0.012523	0.0232519	0.000946	0.38497135	30.86	0.90	0.05900	0.00269	0.38	237.5	4.6	205.6	3	566	50	203.9	2.9	64	64	203.9	2.9	64	13
JN2060 80	396.5	1.8	0.134703	0.010172	0.041785	0.000763	0.387648013	28.98	4.61	0.07076	0.00264	0.99	295	16	219	17	950	38	215	16	77	77	215	16	77	26
JN2060 62	497.0	1.3	0.277556	0.007259	0.044166	0.000761	0.523038785	22.58	0.44	0.04520	0.00094	0.62	247.4	1.9	279.4	2.6	0.0	20	281.1	2.4	31	31	281.1	2.4	31	4
JN2060 68	9.7	48.2	0.418668	0.166206	0.232925	0.012172	0.744607025	20.7	0.12	0.75309	0.01856	0.75	360.5	4.3	481.8	20	483.5	48	716.7	4.6	62	62	716.7	4.6	62	59
JN2060 14	44.1	5.4	0.492469	0.249281	0.49413	0.0108409	0.895511026	6.86	0.43	0.07409	0.00200	0.90	92.6	12	87.7	26	1043	27	87.3	26	16	16	87.3	26	16	5
JN2060 59	1532.9	29.5	3.315022	0.058345	0.270613	0.004769	0.992461668	1.82	0.45	0.29561	0.01222	1.60	447.4	11.6	281.4	282	491.3	42	1045	28	43	43	1045	28	43	22
JN2060 50	1402.1	4.9	0.060238	0.005918	0.319153	0.005883	0.58165034	3.14	0.06	0.08875	0.00115	0.66	481.6	5.2	154.1	12	1398	12	1398	12	1398	12	1398	12	1398	-4
JN2060 57	75.0	0.1	0.401824	0.29944	0.725614	0.288245	0.999099518	2.82	0.66	0.09562	0.00667	0.99	168.2	5.8	178.2	14	1528	14	1528	14	1528	14	1528	14	1528	-7
JN2060 32	78.7	0.9	0.154118	0.095473	0.317363	0.00647	0.631408716	3.16	0.07	0.09657	0.00185	0.63	167.3	7.1	177.2	16	1566	18	1566	18	1566	18	1566	18	1566	-13
JN2060 77	813.0	29.7	4.814633	1.011025	0.33646	0.061513	0.961409666	3.32	0.45	0.09757	0.00279	0.96	164.4	4.4	169.7	10.1	1577	27	1577	27	1577	27	1577	27	1577	-3
JN2060 67	639.5	3.1	0.159366	0.07544	0.310604	0.005872	0.48481762	3.28	0.06	0.09838	0.00170	0.55	166.1	4.4	171.7	14	1593	16	1593	16	1593	16	1593	16	1593	-8
JN2060 1	925.7	11.5	3.70687	0.095423	0.247007	0.005555	0.605518587	4.06	0.09	0.10011	0.00223	0.61	1593.3	7.7	141.8	14	1625	21	1625	21	1625	21	1625	21	1625	6
JN2060 87	2054.3	5.8	0.43583	0.132316	0.280603	0.008228	0.88095344	3.55	0.09	0.10356	0.00174	0.88	1637.5	5.4	159.8	18	1688	16	1688	16	1688	16	1688	16	1688	2
JN2060 18	759.7	5.4	3.956987	0.108547	0.27795	0.007031	0.744629384	3.62	0.09	0.10403	0.00192	0.74	1627	7	157.4	18	1696	17	1696	17	1696	17	1696	17	1696	3

JN2060	70	316.2	2.2	4.321566	0.085134	0.297655	0.005383	0.646408283	3.37	0.06	0.10516	0.00165	0.65	1694	5.9	1676	13	1716	14	1716	14	1716	14	2	2	1	
JN2060	24	232.1	3.5	3.145036	0.20155	0.217331	0.012709	0.950134757	4.75	0.33	0.10557	0.00218	0.95	1423	19	1231	39	1724	19	1724	19	1724	19	29	29	13	
JN2060	9	394.0	2.5	3.654669	0.266748	0.241479	0.014955	0.962220857	4.28	0.30	0.10720	0.00229	0.96	1517	19	1354	43	1752	20	1752	20	1752	20	23	23	11	
JNCM1943: Metagraywacke from East Blue Ridge Road, analyzed July 2020																											
JNCM1943-4	646	244.0425	44.445	4.96644	1.840443	0.840443	0.00443	0.840443652	0.423	0.46	0.5472	0.1494	-0.05	9566	288	48003	4823	4246	244	0.54	4823	244	0.54	4823	-149	-84	
JNCM1943-40	458.1	0.9	0.133517	0.01136	0.013175	0.00037	0.024989373	76.38	2.22	0.0724	0.00652	0.28	0.28	124.67	4.83	83.85	1.21	996.3	87	64.7	91.7	64.7	91.7	92	92	33	
JNCM1943-44	236.8	2.0	0.098832	0.009201	0.013185	0.000392	0.005836798	76.36	2.26	0.0545	0.0052	0.25	0.25	95.27	4.21	83.87	1.23	391	107	83.3	123	83.3	123	79	79	33	
JNCM1943-16	603.1	2.0	0.089697	0.003598	0.013413	0.000457	0.540493329	75.21	1.80	0.0485	0.0017	0.36	0.36	86.45	2.68	85.15	1.41	122.7	41.3	85.1	1.41	85.1	1.41	31	31	2	
JNCM1943-14	305.7	2.1	0.087049	0.005677	0.013633	0.000345	0.412252287	73.71	1.59	0.0461	0.0028	-0.03	-0.03	83.95	2.68	86.87	1.11	177	73.18	87	1.11	87	1.11	4808	-3		
JNCM1943-3	545.6	1.7	0.086255	0.005485	0.013758	0.000421	0.343245505	72.23	2.28	0.0457	0.0027	0.15	0.15	83.78	2.51	87.43	1.35	0.000665	54	87.6	1.35	87.6	1.35	-134507592	-4		
JNCM1943-55	557.6	1.9	0.093478	0.003826	0.014057	0.000392	0.283659515	71.56	2.03	0.0480	0.0021	0.37	0.37	89.78	1.82	89.46	1.26	98.2	51.8	89.4	1.26	98.2	51.8	9	9	0	
JNCM1943-6	2159.5	2.7	0.091926	0.003876	0.014068	0.000311	0.490526887	71.46	1.59	0.0475	0.0018	0.07	0.07	89	1.81	89.58	0.99	73.4	45	89.6	0.99	89.6	0.99	-22	-22	-1	
JNCM1943-72	751.2	1.9	0.094088	0.004475	0.014068	0.000354	0.265784884	71.42	1.77	0.0486	0.0023	0.24	0.24	91.02	2.08	89.63	1.1	127.5	55.7	89.6	1.1	55.7	89.6	1.1	30	2	
JNCM1943-13	428.1	1.8	0.099198	0.005068	0.014158	0.000458	0.19703341	71.15	2.14	0.0511	0.0031	0.58	0.58	95.84	2.27	89.97	1.34	244.3	69.9	89.7	1.34	69.9	89.7	1.34	63	6	
JNCM1943-39	260.1	1.9	0.099051	0.006882	0.014095	0.000274	0.403500972	71.16	1.43	0.0501	0.0032	-0.13	-0.13	94.03	3.12	89.96	0.9	198.6	74.2	89.7	0.9	74.2	89.7	0.9	55	4	
JNCM1943-23	518.5	2.0	0.093378	0.003177	0.014295	0.000397	0.219343896	70.37	1.98	0.0478	0.0019	0.52	0.52	90.87	1.51	90.96	1.27	88.3	47.1	91	1.27	88.3	47.1	91	1.27	-3	0
JNCM1943-1	2261.3	1.8	0.100331	0.003941	0.014461	0.000459	0.728779865	69.68	2.17	0.0506	0.0014	0.08	0.08	96.85	1.85	91.86	1.42	221.6	32	91.6	1.42	32	91.6	1.42	59	5	
JNCM1943-48	314.5	1.7	0.100757	0.004866	0.014997	0.000446	0.311501868	67.13	1.97	0.0475	0.0018	0.26	0.26	94.48	1.87	95.32	1.39	73.4	45	95.4	1.39	45	95.4	1.39	-30	-1	
JNCM1943-50	857.1	2.7	0.100396	0.003328	0.014937	0.000405	0.20707797	66.75	1.57	0.0484	0.0019	0.53	0.53	96.71	1.54	95.86	1.12	117.8	46.3	95.8	1.12	46.3	95.8	1.12	19	1	
JNCM1943-2	575.3	2.4	0.101995	0.003986	0.015193	0.000341	0.302491528	66.08	1.48	0.0489	0.0019	0.27	0.27	98.61	1.84	96.82	1.08	142	45.6	96.7	1.08	32	96.7	1.08	32	2	
JNCM1943-60	1179.1	2.6	0.101773	0.004169	0.015163	0.000443	0.454285607	65.80	1.64	0.0486	0.0019	0.26	0.26	98.43	1.9	97.23	1.2	127.5	46	97.2	1.2	46	97.2	1.2	24	1	
JNCM1943-57	497.3	3.2	0.153223	0.019276	0.015603	0.000393	0.287051041	63.95	1.46	0.0706	0.0082	-0.09	-0.09	143.81	8.07	100.02	1.13	94.5	119	97.7	1.13	97.7	1.13	89	30	1	
JNCM1943-61	249.2	2.0	0.102753	0.00289	0.015307	0.000251	0.524144081	65.47	1.07	0.0486	0.0012	0.06	0.06	98.9	1.36	97.72	0.79	127.5	29.1	97.7	0.79	29.1	97.7	0.79	23	1	
JNCM1943-29	861.7	2.3	0.102408	0.004695	0.015373	0.000365	0.390372822	63.83	1.46	0.0479	0.0021	0.17	0.17	99.93	2.18	100.21	1.14	93.3	51.9	100.2	1.14	51.9	100.2	1.14	-7	0	
JNCM1943-51	617.0	4.2	0.121192	0.008285	0.016086	0.00076	0.799086888	63.26	3.02	0.0539	0.0021	-0.21	-0.21	112.74	3.61	101.11	2.39	365.9	43.9	100.5	2.39	43.9	100.5	2.39	72	10	
JNCM1943-70	333.1	2.9	0.112904	0.007205	0.016033	0.000592	0.356125276	63.02	2.31	0.0512	0.0031	0.28	0.28	107.76	3.14	101.49	1.85	248.8	69.7	101.2	1.85	69.7	101.2	1.85	59	6	
JNCM1943-43	736.0	1.8	0.106997	0.004136	0.015883	0.000286	0.190531781	63.12	1.18	0.0482	0.0019	0.28	0.28	101.6	1.87	101.33	0.94	108	46.6	101.3	0.94	46.6	101.3	0.94	6	0	
JNCM1943-42	237.5	2.9	0.106004	0.006477	0.015961	0.000446	0.052338545	63.03	1.76	0.0477	0.0032	0.39	0.39	100.74	2.96	101.47	1.41	83.3	79.6	101.5	1.41	79.6	101.5	1.41	-22	-1	
JNCM1943-27	485.5	3.0	0.102228	0.00347	0.015941	0.000383	0.363565982	63.00	1.46	0.0471	0.0016	0.33	0.33	99.57	1.62	101.52	1.17	53.2	40.5	101.6	1.17	40.5	101.6	1.17	-91	-2	
JNCM1943-49	75.4	2.2	0.11996	0.012702	0.016191	0.000356	0.466221678	61.99	1.37	0.0553	0.0057	0.20	0.20	115.71	5.84	103.16	1.13	94.1	121	103	1.13	121	103	1.13	70	9	
JNCM1943-15	232.2	4.7	0.136138	0.010072	0.016597	0.000384	0.57995158	61.84	2.17	0.0592	0.0095	-0.12	-0.12	127.78	4.36	105.1	1.86	574.5	64.3	103.9	1.86	64.3	103.9	1.86	82	18	
JNCM1943-33	1443.3	2.0	0.134764	0.013133	0.016594	0.000391	0.159943831	60.53	1.45	0.0598	0.0056	0.03	0.03	129.61	5.84	105.63	1.25	595	101	104	1.25	101	104	1.25	82	19	
JNCM1943-37	143.7	1.7	0.128713	0.010583	0.016474	0.000376	0.381451916	60.95	1.38	0.0553	0.0042	0.06	0.06	119.63	4.44	104.91	1.18	423.4	84.7	104	1.18	84.7	104	1.18	75	12	
JNCM1943-38	322.5	1.6	0.110888	0.008943	0.016413	0.000472	0.408159342	61.32	1.84	0.0486	0.0035	0.31	0.31	105.26	3.44	104.28	1.55	127.5	84.7	104.2	1.55	84.7	104.2	1.55	18	1	
JNCM1943-41	184.9	2.7	0.114495	0.007124	0.017024	0.00033	0.009659382	58.91	1.14	0.0469	0.0032	0.28	0.28	105.71	3.29	104.51	1.04	43.1	81.6	108.7	1.04	81.6	108.7	1.04	-152	-3	
JNCM1943-54	582.9	2.3	0.11874	0.005712	0.017465	0.000391	0.50824412	57.48	1.31	0.0489	0.0020	0.00	0.00	112.57	2.49	111.19	1.26	142	48	111.1	1.26	48	111.1	1.26	22	1	
JNCM1943-36	152.4	2.0	0.123844	0.010963	0.018101	0.000446	0.041303736	55.52	1.45	0.0506	0.0047	0.24	0.24	120.14	5.11	115.08	1.49	222	107	115	1.49	107	115	1.49	48	4	
JNCM1943-11	585.3	1.9	0.124372	0.002743	0.018184	0.00042	0.370530521	55.23	1.32	0.0491	0.0015	0.43	0.43	117.36	1.64	115.68	1.37	151.6	35.8	115.6	1.37	35.8	115.6	1.37	24	1	
JNCM1943-9	633.9	2.0	0.127004	0.005419	0.01837	0.00035	0.250066398	54.59	1.05	0.0501	0.0021	0.18	0.18	120.93	2.44	117.02	1.12	198.6	48.7	116.8	1.12	48.7	116.8	1.12	41	3	
JNCM1943-25	275.2	2.4	0.116329	0.005277	0.018373	0.00041	0.408159307	54.63	1.24	0.0464	0.0020	0.08	0.08	112.4	2.5	116.93	1.32	17.4	51.8	117.2	1.32	51.8	117.2	1.32	-572	-4	
JNCM1943-56	123.9	2.6	0.122968	0.009692	0.019069	0.000434	0.271158859	52.64	1.13	0.0465	0.0036	0.02	0.02	116.65	4.4	121.31	1.29	22.5	92.9	121.6	1.29	92.9	121.6	1.29	-439	-4	
JNCM1943-7	938.0	3.4	0.151438	0.006352	0.020616	0.000491	0.470583192	45.59	1.00	0.0498	0.0018	0.06	0.06	103.39	2.73	139.87	1.37	184.6	42.1	139.7	1.37	42.1	139.7	1.37	24	2	
JNCM1943-19	1294.4	14.2	1.736309	0.10628	0.126273	0.008078	0.939136179	8.19	0.54	0.1001	0.0021	0.45	0.45	1002.7	19.1	742.6	23.1	1625.1	19.5	1625.1	19.5	1625.1	19.5	54	26	2	
JNCM1943-22	416.9	3.5	3.286628	0.110153	0.221273	0.00707	0.8404899517	4.54	0.15	0.1080	0.0020	0.03	0.03	1476	14.5	1283.3	19.2	1765.1	16.9	1765.1	16.9	1765.1	16.9	27	13	1	
JNCM1943-8	836.7	4.3	2.828358	0.066264	0.187327	0.004304	0.739072224	5.36	0.13	0.1094	0.0023	0.25	0.25	1359	10.4	1102.8	12.3	1788.6	19.2	1788.6	19.2	1788.6	19.2	38	19	1	

JNCM1942-27	708.3	2.5	0.109553	0.005119	0.016216	0.000617	62.36	2.40	0.0500	0.0023	0.10	106.42	2.88	102.55	1.96	193.9	53.5	102.35	1.95	47	4
JNCM1942-4	650.2	1.9	0.157119	0.015427	0.016753	0.000575	60.23	2.03	0.0882	0.0060	-0.20	147.24	6.87	106.15	1.77	873.7	91.1	103.96	1.7	88	28
JNCM1942-38	6085.5	2.0	0.108665	0.002819	0.016133	0.000377	61.12	1.65	0.0481	0.0013	0.53	104.56	1.3	104.62	1.4	103.1	31.9	104.62	1.4	-1	0
JNCM1942-19	760.4	2.8	0.10473	0.004261	0.016681	0.000327	59.76	1.36	0.0453	0.0015	0.06	100.89	1.87	105.98	1.21	0.000065	30	107.3	1.21	164584515	-6
JNCM1942-10	1138.8	0.9	0.127644	0.003743	0.018505	0.000099	54.95	1.58	0.0508	0.0014	0.49	121.77	1.63	116.26	1.66	230.7	31.8	115.97	1.65	50	5
JNCM1942-37	874.9	2.2	0.133124	0.008779	0.018891	0.000569	52.83	1.43	0.0526	0.0041	0.24	130.56	4.66	120.88	1.62	310.6	88.7	120.37	1.61	61	7
JNCM1942-38	829.3	5.2	0.175118	0.027895	0.008428	0.000376	44.97	0.50	0.0150	0.0053	0.33	102.25	14.4	517.2	14.0	235.4	30	467.92	8.49	78	49
JNCM1942-41	1184.7	4.4	1.509485	0.166421	0.111817	0.011436	9.84	1.21	0.0976	0.0027	-0.39	874.9	39.9	623.9	36.6	1377.9	25.9	1377.9	25.9	60	29
JNCM1942-25	403.4	5.0	3.879048	0.109922	0.216815	0.007442	3.75	0.11	0.1049	0.0022	0.31	1604.4	12.2	1523.9	19.9	1711.7	19.3	1711.7	19.3	11	5
JNCM1942-16	459.4	3.8	2.29401	0.162111	0.154359	0.011742	6.79	0.56	0.1086	0.0031	0.19	1182.4	28.6	885.7	34.1	1775.2	26	1775.2	26	50	25
JNCM1942-28	216.6	2.4	4.874781	0.14416	0.325957	0.01109	3.10	0.10	0.1105	0.0039	0.38	1804.4	15.9	1802.3	25.4	1808.8	32.1	1801.8	25.3	0	0
JNCM1947: Meterswacke from north-west area; analyzed August 2020																					
JNCM1947-26	248.2	3.0	0.084566	0.004826	0.013686	0.000427	73.61	2.33	0.04547	0.00235	0.44	82.9	1.9	87.6	1.4	0.00007	50	87.2	1.4	-124285614	-5
JNCM1947-32	539.0	1.8	0.093414	0.002841	0.01364	0.000377	73.12	2.11	0.04947	0.00130	0.72	90.5	0.9	87.6	1.3	169	31	87.4	1.2	48	3
JNCM1947-37	922.9	3.1	0.088599	0.004291	0.013842	0.000378	72.66	1.98	0.05169	0.00198	0.71	95	1.2	88.1	1.2	271	44	88.3	1.2	67	7
JNCM1947-33	286.4	3.7	0.106665	0.011695	0.01398	0.000398	72.03	1.52	0.05498	0.00566	0.29	101.6	4.8	88.9	0.9	411	115	88.3	0.9	78	13
JNCM1947-39	1100.9	2.0	0.096314	0.003905	0.014151	0.00026	70.86	1.35	0.04850	0.00165	0.52	91.5	1.3	90.3	0.9	123	40	90.3	0.9	27	1
JNCM1947-3	246.0	2.2	0.089431	0.004549	0.014389	0.000411	69.93	2.04	0.04640	0.00233	0.23	88.9	2.2	91.5	1.3	17	60	91.7	1.3	-438	-3
JNCM1947-43	450.0	2.5	0.141298	0.019886	0.014845	0.0006	68.20	2.79	0.06716	0.00768	0.61	129.2	5.8	93.8	1.3	841	119	92.2	1.8	89	27
JNCM1947-19	74.5	2.1	0.092307	0.006758	0.014676	0.000451	67.99	1.75	0.04716	0.00330	0.25	92.7	3	94.1	1.2	56	84	94.2	1.2	-68	-2
JNCM1947-27	130.2	1.9	0.104422	0.005802	0.014889	0.000389	67.50	1.71	0.05152	0.00297	0.13	101.6	2.9	94.8	1.2	263	66	94.5	1.2	64	7
JNCM1947-15	267.8	1.2	0.093702	0.004091	0.014933	0.000467	67.46	2.05	0.04743	0.00186	0.48	93.9	1.6	94.9	1.4	70	47	94.9	1.4	-36	-1
JNCM1947-28	341.8	3.6	0.096685	0.004767	0.015042	0.000562	67.20	2.49	0.04713	0.00213	0.49	93.7	1.9	95.2	1.8	55	54	95.3	1.8	-73	-2
JNCM1947-29	487.2	2.9	0.043464	0.007446	0.015448	0.000493	56.57	0.49	0.04846	0.00276	0.99	94.7	0.9	96.6	1.5	180	37	96.4	1.5	46	3
JNCM1947-42	2494.2	2.0	0.106226	0.005631	0.015219	0.000517	66.24	2.12	0.04970	0.00160	0.81	99.9	0.9	96.6	1.5	180	37	96.4	1.5	46	3
JNCM1947-7	390.4	2.3	0.094468	0.003547	0.015158	0.000302	66.17	1.34	0.04694	0.00182	0.18	94.7	1.8	96.7	1.1	45	46	96.8	1.1	-115	-2
JNCM1947-31	771.2	4.3	0.104393	0.004281	0.015382	0.000398	65.33	1.67	0.04910	0.00195	0.40	100.1	1.8	97.9	1.2	151	46	97.8	1.2	35	2
JNCM1947-6	391.7	3.3	0.098386	0.001898	0.015703	0.000308	65.86	1.23	0.04616	0.00134	0.20	96.4	1.4	100.2	1.4	5.1	34.8	100.3	1.4	-1865	-4
JNCM1947-4	490.2	10.0	0.108668	0.004936	0.016026	0.000546	63.82	1.79	0.04706	0.00174	0.43	98.3	1.7	100.2	1.4	51	44	100.3	1.4	96	-2
JNCM1947-11	2428.1	1.8	0.139616	0.020292	0.016441	0.000664	61.66	2.07	0.04986	0.00191	0.58	105.2	1.7	101.6	1.7	187	45	101.4	1.7	46	3
JNCM1947-22	1638.1	2.3	0.100701	0.002424	0.016225	0.000366	61.88	1.43	0.04617	0.00113	0.43	99.4	1.2	103.3	1.2	5.5	29.4	103.5	1.2	-1778	-4
JNCM1947-5	323.8	3.6	0.104704	0.006166	0.016477	0.000449	61.03	1.65	0.04759	0.00254	0.39	103.6	2.4	104.8	1.4	78	63	104.8	1.4	-34	-1
JNCM1947-14	1451.2	5.5	0.118516	0.003987	0.016651	0.00044	60.37	1.55	0.05076	0.00126	0.65	111.3	1.1	105.9	1.3	229	29	105.7	1.3	54	5
JNCM1947-14	721.3	3.1	0.103923	0.003243	0.016502	0.000417	60.45	1.30	0.04762	0.00137	0.47	104.7	1.3	105.8	1.1	105.8	1.1	105.8	1.1	-32	-1
JNCM1947-1	2052.0	3.8	0.108529	0.002851	0.016673	0.000408	60.26	1.47	0.04809	0.00105	0.62	106	1	106.1	1.3	103	26	106.1	1.3	0	0
JNCM1947-24	532.9	15.0	0.139208	0.016501	0.018708	0.001751	56.88	4.83	0.05411	0.00215	0.96	125.1	2.8	112.4	4.7	375	45	111.8	4.7	70	10
JNCM1947-9	535.2	3.8	0.114171	0.003394	0.017669	0.000374	56.78	1.78	0.04879	0.00135	0.50	113.6	1.3	112.5	1.2	137	33	112.5	1.2	18	1
JNCM1947-18	538.7	4.1	0.152918	0.028067	0.01824	0.000995	55.95	2.78	0.06045	0.00780	0.88	141	5.8	114.2	2.8	619	139	112.9	2.8	82	19
JNCM1947-41	2434.7	3.4	0.126736	0.008591	0.017518	0.000971	56.39	3.90	0.05264	0.00225	0.87	122.9	1.7	113.3	3.9	312	49	112.9	3.9	64	8
JNCM1947-23	781.5	2.8	0.133058	0.008586	0.018369	0.000435	54.69	1.31	0.05356	0.00298	0.54	128.6	2.8	116.8	1.4	351	63	116.3	1.4	67	9
JNCM1947-44	982.3	3.0	0.136701	0.01526	0.018768	0.001287	54.59	2.65	0.05165	0.00272	0.95	124	1	117	2.8	260	61	116.7	2.8	55	6
JNCM1947-29	205.9	2.3	0.12385	0.005134	0.018428	0.000669	54.53	1.40	0.04908	0.00218	0.26	118.7	2.5	117.1	1.5	151	52	117.1	1.5	22	1
JNCM1947-13	122.4	2.9	0.115364	0.006172	0.018487	0.000488	54.39	1.49	0.04777	0.00184	0.43	116	2	117.5	1.6	87	46	117.5	1.6	-35	-1
JNCM1947-12	654.2	2.8	0.116457	0.003688	0.018499	0.000415	54.27	1.22	0.04760	0.00132	0.48	115.9	1.4	117.7	1.3	78	33	117.8	1.3	-51	-2

JN2161-14	154.5239	1.50499	0.094224	0.010337	0.000691	0.5144927791	72.53345	3.582761	0.047457	0.004469	0.051216427	88	5	88	2	72	112	88	2	-0.7	-22.6	
JN2161-15	154.3.239	1.473581	0.10056	0.004866	0.013854	0.000596	0.432777991	72.28443	2.673516	0.049674	0.003131	0.265878333	91.9	3.2	88.6	1.6	179	73	88.4	1.6	3.6	50.5
JN2161-19	810.3555	1.976658	0.092775	0.005639	0.013974	0.000307	0.230647099	72.04556	2.628735	0.051906	0.002382	0.38891395	96	2	89	2	280	53	88	2	7.5	68.3
JN2161-5	172.6558	1.489398	0.093569	0.010745	0.014141	0.000709	0.116899951	71.85955	3.163655	0.048902	0.006121	0.296619052	91	5	89	2	142	147	89	2	2.1	37.3
JN2161-70	1071.494	1.587101	0.094979	0.004826	0.014311	0.000639	0.500991687	70.9128	3.279238	0.048297	0.002313	0.359274228	91	2	90	2	113	57	90	2	0.9	20.3
JN2161-37	371.3859	2.850202	0.106955	0.007993	0.01473	0.000757	0.067960759	69.70156	3.760585	0.052933	0.004825	0.51544416	102	4	93	2	325	103	92	2	9.1	71.5
JN2161-16	1393.908	5.178797	0.101402	0.004859	0.014622	0.000356	0.687103162	69.12558	2.770999	0.049226	0.001759	0.199567907	95	2	93	2	158	42	92	2	2.6	41.4
JN2161-53	704.8808	2.619671	0.091705	0.005853	0.014698	0.000597	0.520000556	68.83775	2.770864	0.045512	0.002288	-0.010934671	89	3	93	2	0	58	93	2	-5.1	-46.899900.0
JN2161-67	374.0883	1.506019	0.104553	0.009616	0.014992	0.000307	0.002980223	67.26501	2.312099	0.050562	0.004917	0.348409771	100	4	95	2	270	113	95	2	5.0	56.8
JN2161-18	623.4168	1.272094	0.100841	0.005128	0.014944	0.000459	0.243051173	67.3641	2.010758	0.048871	0.002527	0.310602526	97	2	95	1	141	61	95	1	1.9	32.6
JN2161-9	492.0523	2.59307	0.105108	0.00928	0.015887	0.000382	0.531215253	64.06863	3.04078	0.047605	0.003328	0.032317939	99	4	100	2	79	83	100	2	-0.8	-26.3
JN2161-44	337.1888	3.143551	0.105111	0.006959	0.015812	0.000679	0.289047598	64.06076	2.64993	0.047293	0.002744	0.361653847	98	3	100	2	63	69	100	2	-1.5	-58.6
JN2161-23	1063.143	1.748209	0.140173	0.006641	0.019963	0.000899	0.786044686	50.7043	2.535552	0.050411	0.001854	0.31026932	131	3	127	3	213	43	127	3	3.3	40.4
JN2161-52	525.5025	7.812568	0.176006	0.002909	0.023316	0.002417	0.733082358	46.46247	4.936505	0.054369	0.003881	0.209670746	152	8	137	7	385	80	136	7	9.6	64.3
JN2161-11x	534.9942	2.221163	0.461563	0.172809	0.046867	0.013266	0.982977392	40.53628	1.105463	0.060351	0.007262	0.635077739	190	26	157	21	615	130	155	21	17.4	74.5
JN2161-46	534.1554	1.253203	0.180426	0.011201	0.026331	0.000892	0.504421278	37.86888	1.56482	0.048907	0.002766	0.3157631325	166	5	168	3	142	66	168	3	-1.0	-18.3
JN2161-36	1270.42	11.80322	0.212794	0.015667	0.027426	0.00167	0.668164548	37.39207	2.22107	0.055814	0.002841	0.151602254	190	6	170	5	444	57	169	5	10.5	61.7
JN2161-41	607.8137	1.091499	0.183049	0.010683	0.026675	0.000792	0.550048383	37.43287	1.268651	0.048863	0.002481	0.084072544	168	5	170	3	140	60	170	3	-1.2	-21.4
JN2161-11	771.3247	0.861769	0.195531	0.012823	0.027254	0.001042	0.600766958	36.67441	1.215524	0.051234	0.002802	0.652201263	179	5	173	3	251	63	173	3	3.1	30.9
JN2161-32	268.6502	0.992151	0.273517	0.016733	0.036908	0.001182	0.442093654	27.98947	0.874262	0.05315	0.002951	0.104313063	241	7	232	4	334	63	231	4	3.9	30.5
JN2161-27	282.1236	1.174361	0.298707	0.016341	0.042759	0.001336	0.380973681	23.87828	0.818051	0.05062	0.00268	0.272884069	261	6	265	4	232	61	265	4	-1.3	-14.0
JN2161-31	190.6551	3.716105	0.930464	0.152846	0.08526	0.013252	0.950338469	13.6398	1.775138	0.078383	0.003569	0.145124947	592	30	456	29	1156	45	1156	45	23.0	60.6
JN2161-65	376.5723	3.184049	1.876889	0.093905	0.148502	0.008187	0.754431709	6.884582	0.382407	0.088901	0.003343	0.432085983	1038	17	874	23	1401	36	1401	36	15.8	37.6
JN2161-2x	425.598	20.66462	2.920804	0.092672	0.230262	0.007693	0.733185667	4.375604	0.135944	0.094652	0.002249	0.401657787	1403	15	1327	19	1520	22	1520	22	5.4	12.7
JN2161-18	636.1731	2.457775	3.309959	0.125645	0.270655	0.007963	0.5111319803	3.718287	0.114988	0.086946	0.002793	0.24102793	1463	15	1535	21	1358	31	1358	31	-4.9	-13.0
JN2161-15	121.5713	1.599127	3.108951	0.142792	0.247104	0.009927	0.729519831	4.094206	0.163538	0.089317	0.002903	0.182860647	1409	18	1409	25	1410	31	1410	31	0.0	0.1
JN2161-28	263.5546	0.944093	2.93611	0.127659	0.232481	0.008707	0.509134237	4.298156	0.148325	0.089744	0.003164	0.351891412	1376	15	1348	21	1419	34	1419	34	2.0	5.0
JN2161-20	295.595	4.21262	3.573807	0.175619	0.258625	0.012404	0.533317147	3.762148	0.186607	0.095315	0.004378	0.467289665	1521	19	1512	33	1533	43	1533	43	0.6	1.4
JN2161-7x	144.7605	1.299375	3.826534	0.157687	0.280356	0.009317	0.51250583	3.594928	0.117056	0.003832	0.314598821	1614	20	1582	23	1656	35	1656	35	2.0	4.5	
JN2161-42	267.2648	2.685123	4.3178	0.207145	0.316007	0.01546	0.557617748	3.220237	0.158462	0.097605	0.003839	0.46427718	1670	19	1743	38	1578	37	1578	37	-4.4	-10.5
JN2161-48	399.2748	1.820237	4.28189	0.174694	0.319175	0.009981	0.540520051	3.149669	0.102201	0.098409	0.003584	0.197876884	1703	18	1777	25	1612	34	1612	34	-4.3	-10.2
JN2161-34	270.8329	3.827055	3.653482	0.143984	0.264897	0.011263	0.446343854	3.82519	0.164054	0.099532	0.00424	0.566036606	1546	16	1497	29	1615	40	1615	40	3.2	7.3
JN2161-22	205.0265	2.397874	4.639449	0.194927	0.333201	0.01205	0.462841347	3.029855	0.109894	0.096683	0.004095	0.439282627	1737	17	1839	29	1617	38	1617	38	-5.9	-13.7
JN2161-51	228.7932	4.784585	4.062124	0.187247	0.300322	0.012351	0.5337585001	3.326628	0.125331	0.099677	0.004242	0.41841737	1660	18	1694	28	1617	40	1617	40	-2.0	-4.8
JN2161-5x	908.1196	19.20114	8.161261	0.104583	0.285736	0.006744	0.51581507	3.466949	0.094778	0.098802	0.002606	0.486461999	1615	15	1625	20	1601	25	1601	25	-0.6	-1.5
JN2161-6	993.1268	112.0513	4.007701	0.142855	0.293055	0.013368	0.382427412	3.4636	0.156914	0.100452	0.004576	0.667810999	1634	15	1635	33	1632	42	1632	42	-0.1	-0.2
JN2161-21	372.5968	2.666913	4.735288	0.215985	0.334981	0.012741	0.278844537	3.016473	0.114441	0.101353	0.005108	0.496221529	1755	19	1846	30	1648	47	1648	47	-5.2	-12.0
JN2161-29	251.1998	7.982823	4.221327	0.178626	0.298875	0.014138	0.546048332	3.400418	0.160386	0.102034	0.004369	0.564300284	1661	17	1662	35	1661	40	1661	40	-0.1	-0.1
JN2161-75	2485.422	83.72393	3.516443	0.138022	0.249437	0.007569	0.442983831	4.037367	0.133299	0.102456	0.003835	0.319201042	1527	16	1427	21	1668	35	1668	35	6.5	14.4
JN2161-76	109.7053	3.205006	4.672814	0.189563	0.331672	0.013069	0.484077602	3.05162	0.124598	0.102675	0.003918	0.485193159	1756	17	1827	32	1672	35	1672	35	-4.0	-9.3
JN2161-1	178.5669	6.836633	4.343702	0.109403	0.301863	0.013469	0.801373512	3.357528	0.144192	0.102918	0.003901	0.106128809	1679	20	1881	32	1677	37	1677	37	-0.1	-0.2

JN2161-55	318.9412	1.797114	4.321825	0.19831	0.303172	0.010126	0.386480832	3.326103	0.114943	0.103404	0.004398	0.359062275	1690	18	1695	26	1685	39	1685	39	1685	39	-0.3	-0.6
JN2161-49	82.7544	1.346032	3.891658	0.164477	0.280122	0.011531	0.268535123	3.617488	0.146379	0.103436	0.005905	0.576445045	1673	17	1575	29	1686	45	1686	45	1686	45	3.0	6.6
JN2161-35	918.381	16.08016	3.731085	0.218277	0.268402	0.02073	0.678481838	3.888427	0.309447	0.103798	0.006276	0.555596595	1567	27	1475	52	1692	56	1692	56	1692	56	5.9	12.8
JN2161-50	352.5757	2.668817	4.359558	0.13524	0.310078	0.010263	0.236995173	3.250905	0.112905	0.104014	0.004133	0.657167724	1714	13	1729	26	1696	37	1696	37	1696	37	-0.9	-1.9
JN2161-45	512.634	2.251627	4.931668	0.24858	0.339003	0.010341	0.622664287	2.946068	0.104597	0.104065	0.004118	0.049598994	1797	22	1884	29	1697	36	1697	36	1697	36	-4.8	-11.0
JN2161-38	250.8509	2.673761	4.772438	0.210832	0.331539	0.016769	0.491583597	3.071758	0.152695	0.104259	0.004965	0.557418296	1763	19	1817	39	1700	44	1700	44	1700	44	-3.1	-6.9
JN2161-73	168.469	2.131436	4.326552	0.144122	0.300302	0.008045	0.666383946	3.346895	0.087403	0.104485	0.002673	0.22091246	1694	13	1685	19	1704	24	1704	24	1704	24	0.5	1.1
JN2161-69	442.8744	4.224192	3.830069	0.141389	0.263252	0.007496	0.494920879	3.789714	0.125806	0.104515	0.003662	0.489753063	1593	14	1510	22	1705	32	1705	32	1705	32	5.2	11.4
JN2161-59	1462.741	14.56801	4.050876	0.180138	0.2773	0.011112	0.523530806	3.647515	0.143771	0.106457	0.004781	0.204855223	1639	22	1562	27	1739	41	1739	41	1739	41	4.7	10.2
JN2161-64	274.8668	1.902701	4.106792	0.146606	0.275064	0.008248	0.535308426	3.660042	0.113467	0.107356	0.003466	0.300436183	1643	15	1557	21	1754	30	1754	30	1754	30	5.2	11.2
JN2161-74	1890.468	1.112872	4.641524	0.148901	0.315219	0.012732	0.422044628	3.20821	0.123248	0.107467	0.004138	0.673936069	1752	13	1749	29	1756	35	1756	35	1756	35	0.2	0.4
JN2161-63	1388.918	7.21574	4.180374	0.214492	0.279793	0.016021	0.680667007	3.667093	0.211198	0.107988	0.004762	0.465807328	1647	22	1557	40	1765	40	1765	40	1765	40	5.5	11.8
JN2161-62	1891.251	3.761258	4.389896	0.187626	0.289493	0.012229	0.671865891	3.498752	0.146336	0.109006	0.00362	0.323022349	1692	18	1621	30	1782	30	1782	30	1782	30	4.2	9.0
JN2161-24	875.3529	9.558063	4.969552	0.468429	0.310618	0.022435	0.937794755	3.305662	0.173939	0.112536	0.004002	-0.14724799	1766	28	1704	39	1840	32	1840	32	1840	32	3.5	7.4
JN2161-72	468.1588	4.33983	10.16818	0.3301	0.444458	0.021893	0.507205698	2.261967	0.064477	0.165983	0.004987	0.37148735	2445	15	2360	28	2517	25	2517	25	2517	25	3.5	6.2
JN2161-57	1225.551	4.154561	10.32899	0.522161	0.436933	0.016791	0.606381034	2.311962	0.087132	0.170337	0.00723	0.139470337	2449	24	2317	37	2560	36	2560	36	2560	36	5.4	9.5

* Data not corrected for common-Pb.
²⁰⁶Pb/²³⁸U ages common lead corrected by inferring the initial Pb-composition from the Stacey and Kramers (1975) two stage isotope evolution model (Vermeesch, 2018). Analyses with greater than 10% uncertainty in ²⁰⁷Pb/²³⁵U age (1-sigma) or 5% uncertainty in ²⁰⁶Pb/²³⁸U age (1-sigma), 20% discordance, and/or 5% reverse discordance are excluded. Accepted ages calculated using ²⁰⁶Pb/²³⁸U ages for grains younger than 1100 Ma and ²⁰⁷Pb/²³⁵U ages for grains older than 1100 Ma.